

MICROSTRUCTURAL CHANGES INDUCED
IN CARBURIZED STEELS
BY ROLLING CONTACT FATIGUE

ARTHUR LAKES LIBRARY
COLORADO SCHOOL OF MINES
GOLDEN, CO 80401

by

Richard E. Miller

ProQuest Number: 10781213

All rights reserved

INFORMATION TO ALL USERS

The quality of this reproduction is dependent upon the quality of the copy submitted.

In the unlikely event that the author did not send a complete manuscript and there are missing pages, these will be noted. Also, if material had to be removed, a note will indicate the deletion.



ProQuest 10781213

Published by ProQuest LLC (2018). Copyright of the Dissertation is held by the Author.

All rights reserved.

This work is protected against unauthorized copying under Title 17, United States Code
Microform Edition © ProQuest LLC.



ProQuest LLC.
789 East Eisenhower Parkway
P.O. Box 1346
Ann Arbor, MI 48106 – 1346

A thesis submitted to the Faculty and the Board of Trustees of the Colorado School of Mines in partial fulfillment of the requirements for the degree of Master of Engineering (Metallurgical Engineer)

Golden, Colorado


Date 4-15-92

Signed: Richard E. Miller, Jr.
Richard E. Miller

Approved: 
Dr. George Krauss
Thesis Advisor

Dr. Don Williamson
Thesis Co-advisor

Golden, Colorado

Date 4-16-92


Dr. John Moore
Professor and Head
Metallurgy
Department

ABSTRACT

Specimens of AISI 8620 steel were carburized to a case depth of 2 mm and subjected to rolling contact fatigue (RCF) at contact stresses of 3380 MPa and 4146 MPa. The specimens tested at 3380 MPa were systematically rolled to decade intervals of cycles and the stressed volumes of the wear tracks examined by Mössbauer spectroscopy, light microscopy, residual stress measurements, and microhardness profiles. Depth profiles showed that the retained austenite content at the surface and in the region of highest τ_{45} shear stress decreases with increasing cycles of RCF. Hardness increases correlated with the transformation of retained austenite, and residual stress profiles became increasingly compressive as the retained austenite content decreased. The specimens tested at 4146 MPa developed white etching bands at 24 degrees and at 82 degrees to the contact surface after 1 billion cycles. A possible explanation of the controversy as to whether τ_{xz} or τ_{45} is the critical shear stress in rolling contact fatigue is also presented.

TABLE OF CONTENTS

ABSTRACT	iii
1.0 INTRODUCTION	1
1.1 History of this Project	1
1.2 History of Rolling Contact Fatigue Testing	2
2.0 LITERATURE REVIEW	8
2.1 Operating Parameters	8
2.2 Hertzian Stress Analysis	9
2.3 τ_{xz} , σ_1 , σ_2 , σ_3 , and τ_{45}	11
2.4 Retained Austenite	18
2.5 Residual Stress Changes	22
2.6 Hardness Changes	26
2.7 Dark Etching Regions	28
2.8 Nonmetallic Inclusions	35
2.9 White Etching Areas	36
2.9.1 Butterflies	39
2.9.2 30 Degree Bands	41
2.9.3 80 Degree Bands	43
2.9.4 Cracking	43
2.10 Classic Papers on Microstructural Changes	46
2.11 Experimental Matrices	47
3.0 EXPERIMENTAL DESIGN, MATERIAL, AND SPECIMENS ...	50

3.1	Timken Rolling Fatigue Machines	53
3.1.1	Toroid Rollers	58
3.1.2	General Maintenance	58
3.2	Experimental Procedures	60
3.2.1	Specimen Preparation, Machining ...	60
3.2.2	Carburizing and Reheat Treatment ...	61
3.2.3	Residual Stress Measurements	62
3.2.4	Profilometer Traces	64
3.2.5	Sectioning of Samples	66
3.2.6	Sample Identification	68
3.2.7	Mössbauer Spectroscopy	72
3.2.8	Electropolishing, Macroetching	77
3.2.9	Etchants for Microscopy	82
3.2.10	Light Microscopy	82
3.2.11	Microhardness Measurements	82
3.3	Analytical Procedures	84
3.3.1	Ruffian, Analysis Software	84
3.3.2	Ansys and MathCAD Analysis	86
4.0	EXPERIMENTAL RESULTS	89
4.1	As-received and Untested Microstructures ..	95
4.2	Basis for Evaluation of Results	97
4.3	Changes Produced During Stages I-II	100
4.4	Changes Produced During Stages III-IV	110
5.0	DISCUSSION	118
5.1	Discussion of Stages I-II	118

5.2	Discussion of Stages III-IV	121
5.3	Discussion of τ_{45} Versus τ_{xz}	123
5.3.1	τ_{45} Versus τ_{xz} , Fully Reversing Stress Cycle	123
5.3.2	τ_{45} Versus τ_{xz} , Depth to Crack Initiation	124
5.3.3	τ_{45} Versus τ_{xz} , Cracks Parallel to the Surface	126
6.0	CONCLUSIONS	128
7.0	SUMMARY	129
8.0	REFERENCES	130

APPENDIX

Fatigue Machine Start-up	137
Figure A-1: Fatigue Machines Controls	138
Table A-1: Raw Mössbauer Data	141
Table A-2: Microhardness Conversion Chart	143

ACKNOWLEDGMENTS

The author would like to thank the National Science Foundation and ASPPRC for the financial support under which this work was completed and his coworkers at Northwestern University and ASPPRC. He would like to note the donations of expertise and material from the Timken Company and Caterpillar incorporated. Timken donated the rolling contact fatigue machines and AISI 8620 steel. Caterpillar heat treated specimens and measured residual stresses with depth. Specifically thanks to C. Berndt, C. Moyer, D. Lawrentz, T. Mohr, and J. Murza. Also thanks to S. Donnelson of CSM for finding a room for the fatigue machines and to B. Brewer of CSM for metallographic advice.

The author would also like to thank his advisor, Dr. George Krauss for his management of this project and philosophical insights and Dr. Don Williamson for his Mössbauer work, without which this thesis would be much less significant. Dr. Williamson's capable assistant was Orhan Ozturk. Thanks to Dr. Chet VanTyne for explaining Zwirlein and Schlicht's paper and for his perspective on higher education. Thanks to Matt Johnson for welding part of the lubrication system. Lastly, he thanks Lynette L. Laffea for believing in the future.

1.0 INTRODUCTION

The goals of this work were to evaluate literature regarding rolling contact fatigue and to systematically study microstructural changes in carburized steels caused by rolling contact fatigue. Carburized cases are composed of martensite and some retained austenite. High loads, applied over time, cause changes in the depth profile of this composite microstructure. These changes in turn lead to wear, cracking, and spalling. Depending on the rolling conditions, cracks start below or at the surface. This thesis traces the microstructural changes in a representative volume of carburized case during rolling contact fatigue (RCF) and offers an explanation of the controversy concerning whether τ_{45} or τ_{xz} is the critical shear stress in RCF.

1.1 History of this Project

This work is a portion of the research program entitled "Life Prediction for Surface Modification of Tribological Materials," a cooperative National Science Foundation (NSF) tie project between the Center for Engineering Tribology (CET), Northwestern University, and

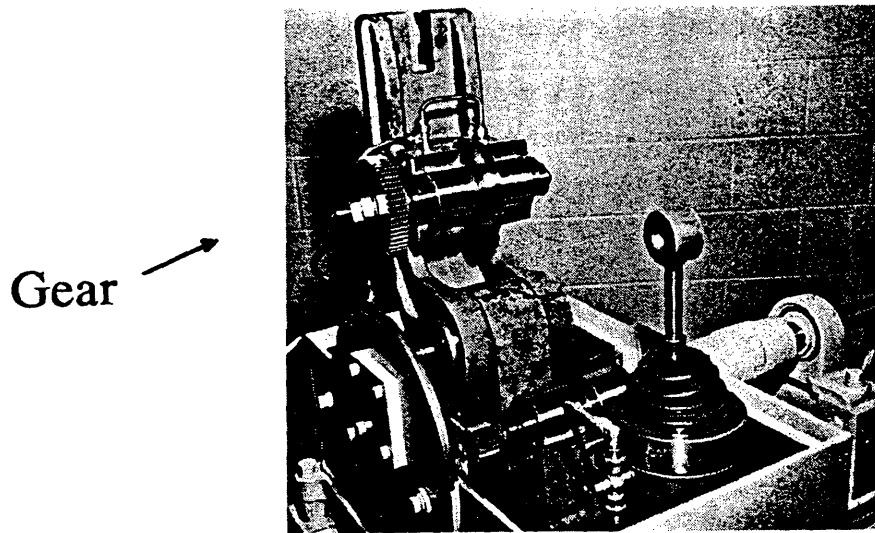
the Advanced Steel Processing and Products Research Center (ASPPRC), Colorado School of Mines. The objective of the ASPPRC portion of the program was to study changes induced in the microstructures of carburized steels due to rolling contact fatigue (RCF). Information about the evolution of microstructural fatigue damage provides Dr. H. Cheng and Dr. L. Keer at Northwestern University with input for fatigue life prediction work.

1.2 History of Rolling Contact Fatigue Testing

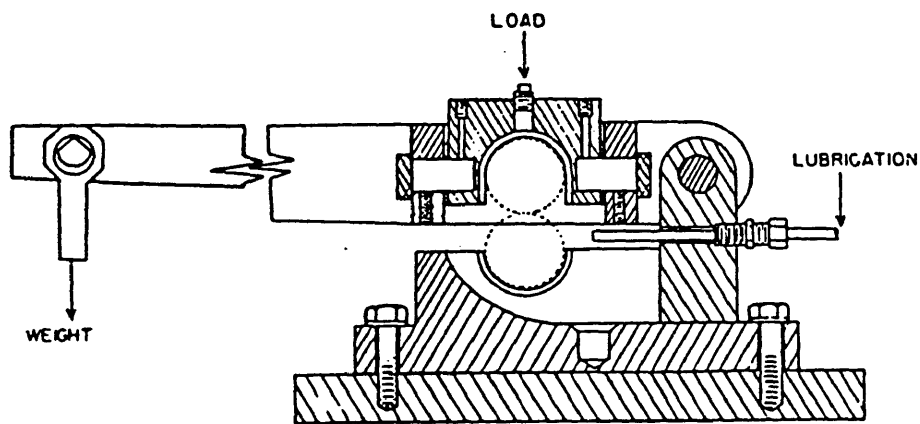
Since as early as the 1910s researchers have been using various testing machines to simulate and accelerate rolling contact fatigue (RCF) (1). Still, the 1946 Symposium on Testing of Bearings, sponsored by ASTM, only discussed full scale bearing tests (2) and not "bench tests". However, during the 1950s, several laboratories, General Electric (GE), Caterpillar (CAT), National Aeronautics and Space Administration (NASA), and Pratt and Whitney, constructed rolling contact fatigue testing machines for their own use. These machines had various specimen geometries and roller geometries such as cylinders, balls, disks, washers, cones, and toroids. The most popular specimen geometry was a cylinder, with the rollers being either balls or toroids (3).

Prior to 1960, there was very little quantitative data and no accepted RCF test with which to classify materials and microstructures (60). In 1960, the Gear Metallurgy Division of the Society of Automotive Engineers became interested in Caterpillar's Geared Roller Test Machine (GRTM) as a means of evaluating the surface durability of various gear steels. R.E. Denning and S.L. Rice were in charge of testing at Caterpillar and worked with SAE on the program. The GRTM became the first "standard" RCF testing machine. Units were sold to aircraft builders, steel and alloy producers, gear manufacturers, lubricant additive producers, machine tool manufacturers, and a business machine manufacturer (1).

The GRTM is capable of imposing sliding as well as rolling loads on a sample. Figure 1 shows a photograph and a schematic front view of the GRTM. The geared roller imposes sliding and removing the gear disables sliding. The GRTM imposes just 1 fatigue cycle per revolution and thus requires many revolutions of the specimen to initiate failure. Therefore, a second design called the "RC Rig", circa 1957, by General Electric, gained popularity (4). Figure 2 shows a schematic and a picture of the original RC Rig prototype. E.N. Bamberger is one of the people associated with its design (3). The GE RC Rig imposes two



a



b

Figure 1: Caterpillar Geared Roller Test Machine (GRTM)
a) isometric view b) front view of a
similar fatigue machine that shows the
method of load application (1,15).

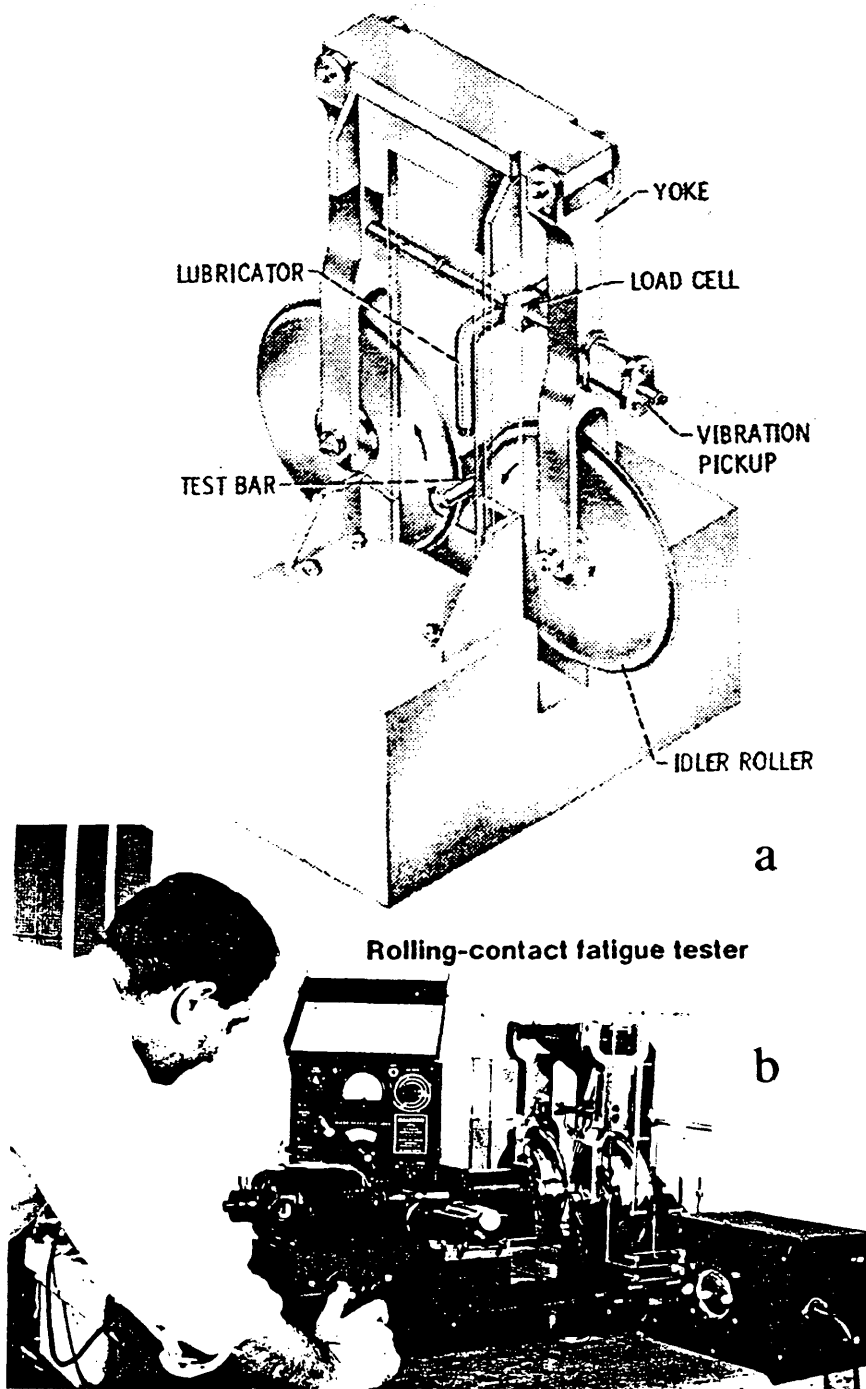
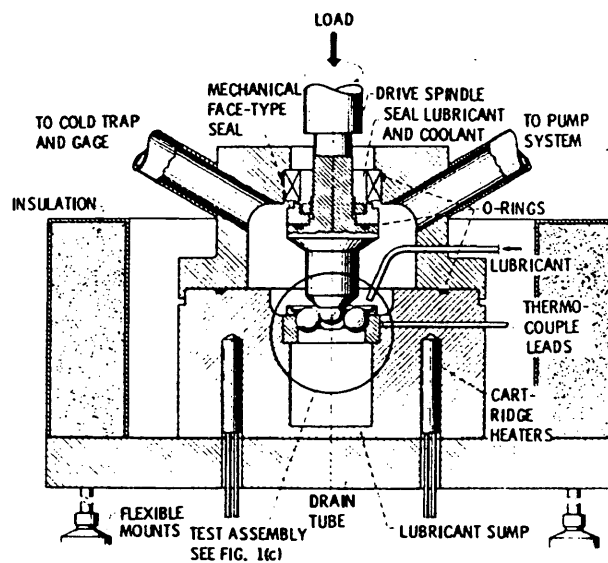


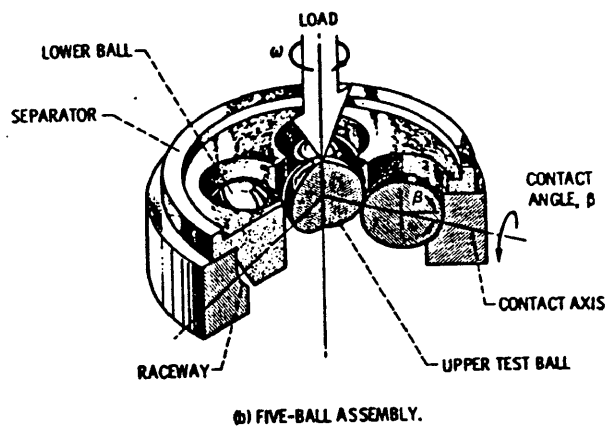
Figure 2: GE "RC Rig" a) schematic b) photo of original prototype (3).

fatigue cycles per revolution which decreases the testing time by one half. Timken built several contact fatigue testing machines similar to this GE RC Rig design in 1964 (5). Two of these Timken machines were donated to CSM and used in this work.

It has been speculated that shear stresses due to pure rolling will be the limiting factor in steel bearing development (1) and thus the GE "pure rolling" type machines, although they cannot test sliding, should be useful in the future. The most popular machines, currently, are 3 ball and 5 ball testers because they decrease the testing fatigue times even more (4,6). Figure 3 consists of two schematic views of the NASA 5-ball tester. Attempts to standardize testing other than the SAE-Caterpillar project have been sporadic. One of the latest attempts to standardize testing is by ASTM and culminated in an international symposium, 1981 (107), with papers by Bamberger, Glover, and Zaretsky.



a



b

Figure 3: NASA 5 Ball Rolling Contact Fatigue Tester
a) front view b) isometric view (4).

2.0 LITERATURE REVIEW

Rolling Contact Fatigue (RCF) is a complex system phenomenon. Performance is based on stress state, material properties, and system operating parameters. Each one of these system components is reviewed below. Emphasis is placed on the basic phenomena of dynamic changes in properties and microstructure caused by RCF.

2.1 Operating Parameters that Affect the Testing

According to Bohm et. al. (5), "The rolling contact fatigue of rolling elements is a property of a system..., it is influenced by a large number of factors that are, besides material properties, mainly... external influences such as temperature, lubricant, and load in connection with contact geometry, surface microtopography and surface residual stress, and elastohydrodynamic (EHD) film thickness." If "ideal conditions," are "established, namely, hydrodynamic rolling, no metal contact, no sliding, no tangential stresses at the surface; speed, temperature, and load... constant" then the chances that microstructural changes will be "modified by the lubricant and surface finish" are less. (Bohm et. al., "Nonmetallic Inclusions and Rolling Contact Fatigue," Bearing Steels: The Rating of Nonmetallic Inclusion, ASTM STP 575, ASTM, 1975, pp. 96-113.)

The quotation from Bohm describes the complexity of RCF systems. Table I lists various RCF variables and indicates how an increase or conversely a decrease in each variable

affects fatigue life (7).

Table I: Effects of Changes in RCF Parameters

Selected Variables	Increase in Variable	
Load	Decrease ↓ in Fatigue Life	
Crown Radius	Increase ↑ in Fatigue Life > Contact Area	
Speed Assuming Elastohydro- dynamic Lubrication	Increase ↑ in Fatigue Life	
Case Temperature	Case Temp. at ≤125°C Increase ↑ in Fatigue Life	Case Temp. at ≥150°C Decrease ↓ in Fatigue Life
Elastohydrodynamic Film Thickness	Increase ↑ in Fatigue Life	
Surface Roughness	Decrease ↓ in Fatigue Life	
Sliding Between RCF Components	Decrease ↓ in Fatigue Life	

2.2 Hertzian Stresses

In 1881, Heinrich Hertz derived an equation for the pressure distribution produced when two solid, elastic,

curved bodies are pressed together under a certain load (8,9). From the pressure distribution, he was able to estimate the principal stress distribution to a fair degree of accuracy. Later investigators derived equations for the stresses, and in 1930, Thomas and Hoersch (10) transformed the equations for the stresses on the axis of symmetry (z axis) into standard elliptical integrals (8). Thus the following stresses can be calculated (9):

$\sigma_1, \sigma_2, \sigma_3$ Principal stresses in the x, y, and z directions on the z axis at depth.

It can be shown that for any general state of stress at any point O in a body there exists three mutually perpendicular planes at point O on which shearing stresses vanish, the principal planes. The equations of Thomas and Hoersch (9) used in this study to calculate the principal stresses only apply when O is on the z axis.

τ_{45} Maximum 45 degree shear stress

$$\frac{(\sigma_1 - \sigma_3)}{2} \quad [1.1]$$

σ_e The Von Mises, distortion energy, equivalent stress

This is the equivalent uniaxial stress that would cause yielding in a uniaxial tension test of the same material. It has the same distribution as τ_{45} , i.e., depth to maximum, and another name for it is the flow stress, σ_o .

$$\sigma_e = \frac{1}{\sqrt{2}} [(\sigma_1 - \sigma_2)^2 + (\sigma_2 - \sigma_3)^2 + (\sigma_3 - \sigma_1)^2]^{\frac{1}{2}} \quad [1.2]$$

τ_{oct} The shear stress on the octahedral planes

$$\tau_{oct} = \frac{1}{3} [(\sigma_1 - \sigma_2)^2 + (\sigma_2 - \sigma_3)^2 + (\sigma_3 - \sigma_1)^2]^{\frac{1}{2}} \quad [1.3]$$

$\sigma_{xx}, \sigma_{yy}, \sigma_{zz}$ The normal stresses

The normal stresses are the stresses perpendicular to the yz, xz, and xy planes respectively.

τ_{xz} Orthogonal shear on the yz plane in the z direction, maximum is at $y=0$, sometimes written σ_{xz} .

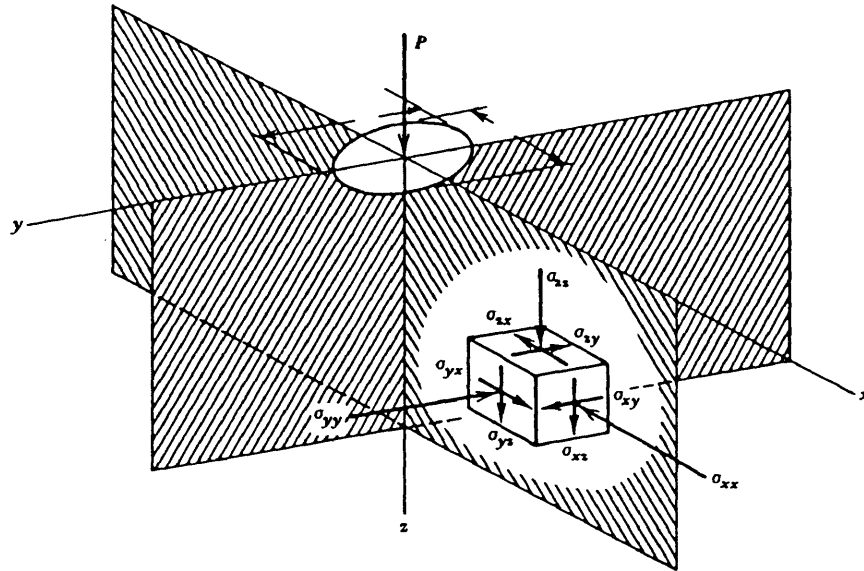
τ_{yz} Orthogonal shear on the y plane in the z direction, maximum is at $x=0$, sometimes written σ_{yz} .

2.3 $\tau_{xz}, \sigma_1, \sigma_2, \sigma_3$, and τ_{45}

τ_{xz} and τ_{45} are two ways of describing parts of a stress state. Either the stress tensor, including τ_{xz} , is given or the stress state is resolved into principal stresses and τ_{45} calculated. Figure 4 illustrates a representative stress cube and the stress tensor. τ_{xz} is the component of the stress tensor which acts on the yz planes of a representative stress cube in the z direction. When the stress state is resolved into principal stresses, then the 45 degree shear stress is defined as:

$$(\text{most positive principal stress} - \text{most negative principal stress}) / 2$$

It is called the maximum shear stress because its magnitude is always greater than any other calculated shear stress



$$\mathbf{T} = \begin{pmatrix} \sigma_{xx} & \sigma_{xy} & \sigma_{xz} \\ \sigma_{xy} & \sigma_{yy} & \sigma_{yz} \\ \sigma_{xz} & \sigma_{yz} & \sigma_{zz} \end{pmatrix}$$

Figure 4: Stress cube and stress tensor,
 σ_{xz} is the same as τ_{xz} (9).

(9,11,12). These two shear stresses, τ_{45} and τ_{xz} , should not be used at the same time to evaluate stress in the material. τ_{45} and τ_{xz} are two different ways of looking at the same stress state and not separate independent stresses in the material.

Figure 5 illustrates characteristics of τ_{45} and τ_{xz} . Figure 5a shows the 45 degree plane of a stress cube. Figure 5b schematically shows regions of highest τ_{xz} shear stress on both sides of the z axis at $y=0$. Figure 5b shows that regions of highest τ_{xz} are symmetric and fully reversing (change sign) with respect to the z axis (13). The τ_{xz} versus rolling distance graph for a point in the wear track is sinusoidal with a mean of zero. Typical profiles of τ_{45} and normal stresses along the z-axis are shown in Figure 6. The normal stresses and the principal stresses are the same at any point on the z-axis. The lower case "a" and "b" in Figure 6 are the semiaxis of the ellipse shown. The "a" dimension is the contact ellipse semiaxis in the rolling direction and the "b" dimension is the contact ellipse semiaxis in the transverse direction (half of the width of the wear track).

The depth of maximum τ_{xz} is usually at $0.50b$ and the depth of maximum τ_{45} is usually at $0.78b$ (9). Lack of lubrication, rough surfaces, residual stress changes, and

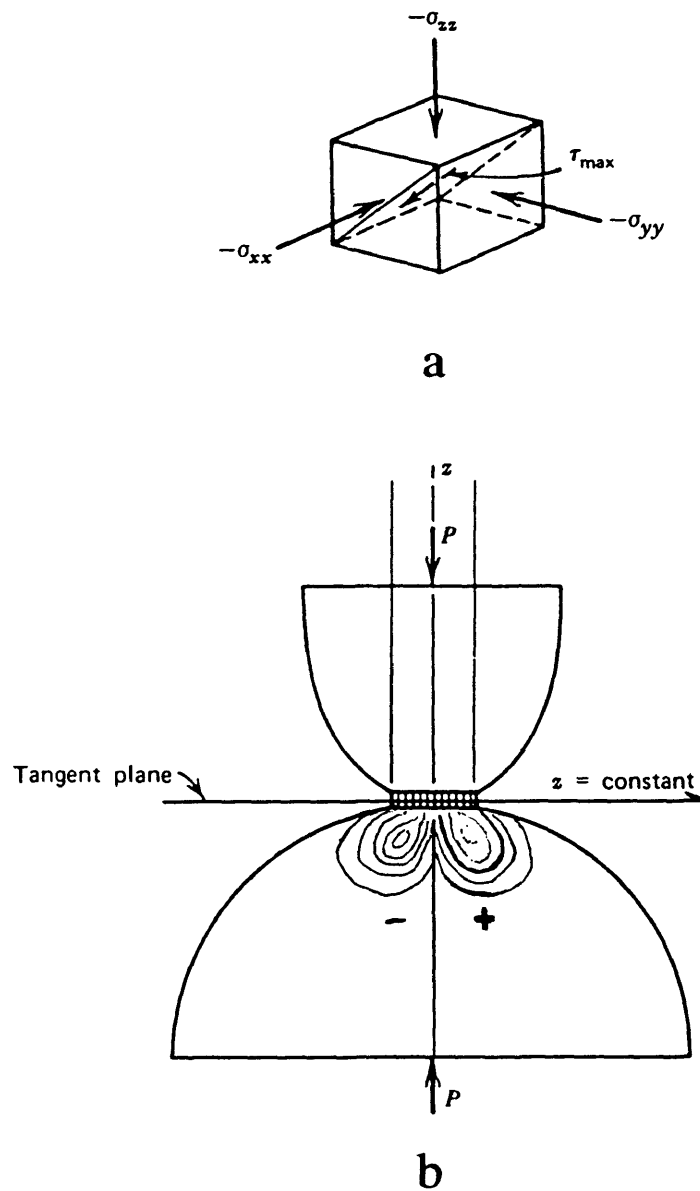


Figure 5: a) Plane of τ_{45} b) schematic contours of τ_{xz} stress showing that τ_{xz} is symmetric and fully reversing (changes sign) about the z axis (9).

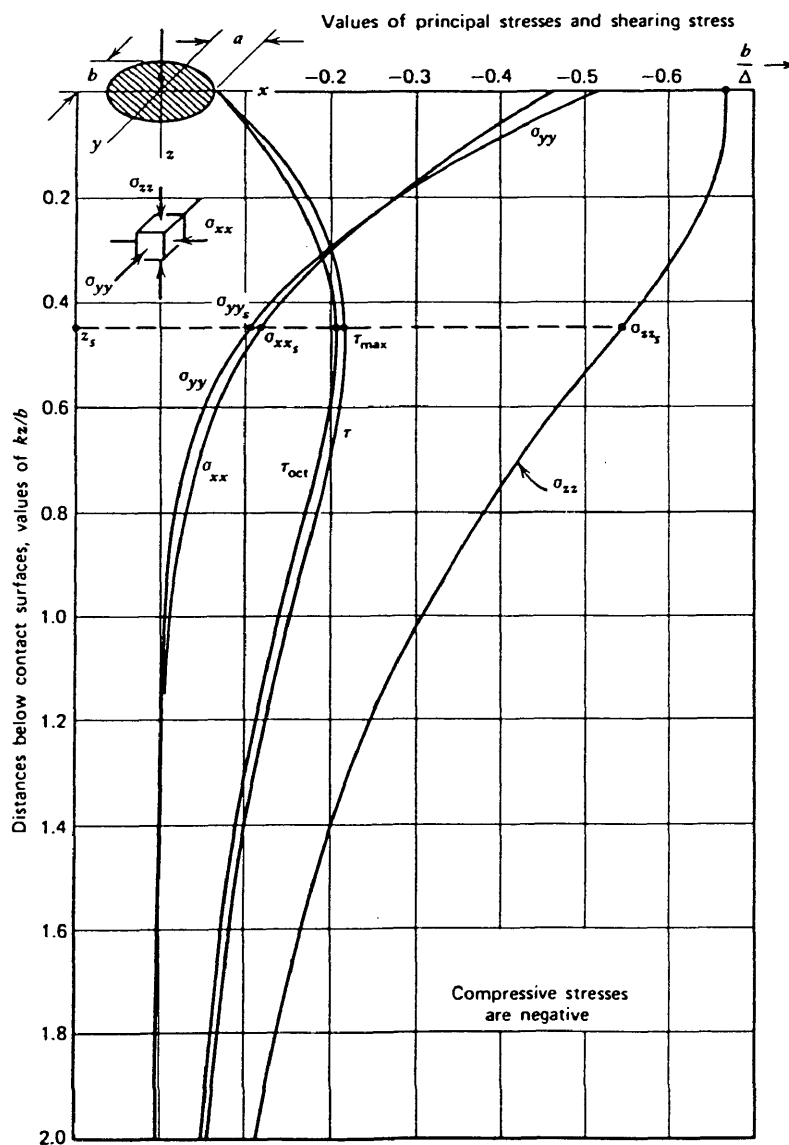
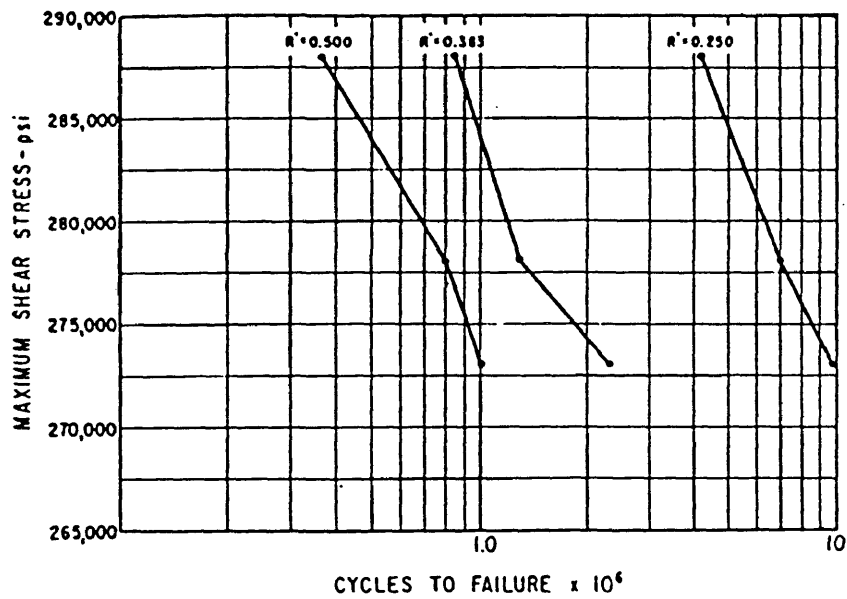


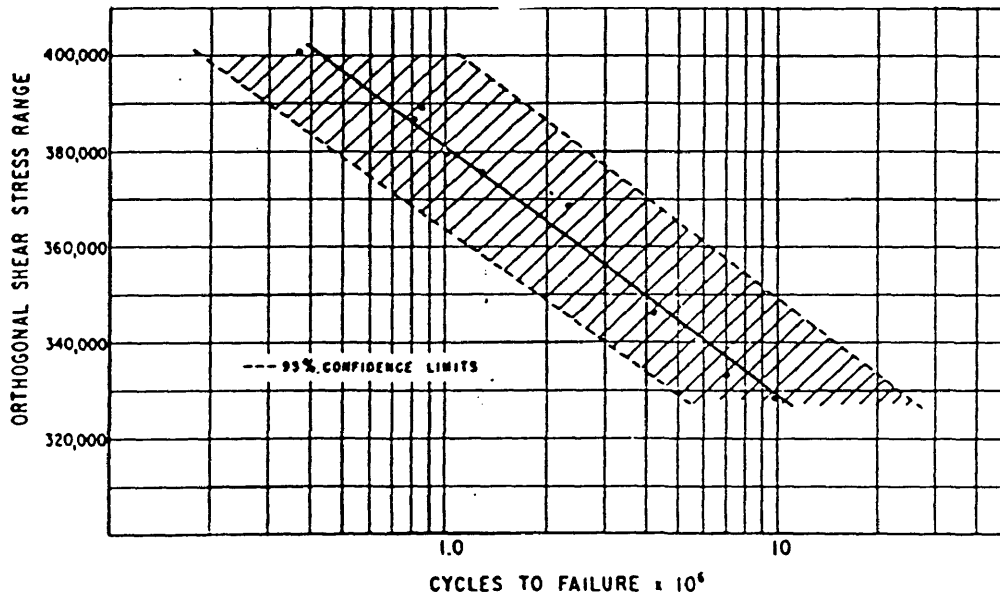
Figure 6: Profiles of τ_{45} , σ_{xx} , σ_{yy} , σ_{zz} , and τ_{oct} along the z axis. Normal stresses are equivalent to the principal stresses along the z axis (9).

many small hard inclusions move the location of peak τ_{45} and τ_{xz} closer to the surface (14).

From as early as 1962, there has been a controversy as to whether τ_{xz} or τ_{45} is responsible for microstructural changes during rolling contact fatigue (11,12,14). Therefore, both τ_{xz} and τ_{45} shear stresses are usually calculated. Greenert convinced many that τ_{xz} is responsible for RCF by plotting τ_{xz} and τ_{45} versus number of cycles to failure, Figure 7, for AISI 52100 test specimens (15). Greenert's plot of τ_{xz} versus cycles to failure, Figure 7b, is more linear than his plot of τ_{45} versus cycles to failure, Figure 7a. Thus he concluded that τ_{xz} is responsible for the microstructural changes because the correlation was better between τ_{xz} and cycles to failure. Many researchers also say that because cracks usually propagate in a direction parallel to the contact surface, τ_{xz} correlates better with rolling contact fatigue (RCF) than τ_{45} . However, it is important to note that theoretically a material should shear along the direction of τ_{45} , before shearing along the xz plane, because the magnitude of τ_{45} is greater. Reductions in retained austenite profiles, residual stress profiles (becoming more compressive), and hardness profiles correlate well with τ_{45}



a



b

Figure 7: Comparison of τ_{45} and τ_{xz} as a function of cycles to failure a) τ_{45} versus cycles to failure, R' is the crown radius of the rollers of the machine shown in Figure 1b b) τ_{xz} versus cycles to failure (15).

profiles such as the one in Figure 6 (15,16).

2.4 Retained Austenite

Retained austenite transforms to martensite during rolling contact fatigue. This transformation occurs by two different mechanisms depending on the conditions. There is a strain induced transformation and a stress induced transformation (17). Figure 8 consists of two graphs of profiles of retained austenite as a function of cycles which show decreased retained austenite as RCF cycles increase. Figure 8a is for carburized bearings (0.18%C, 1.50%Cr, 4.25%Ni, 1.0%W), case depth 2.5 mm, tested at 2800 MPa contact stress. Figure 8b is for SAE 52100 bearings tested at a contact stress of 3300 MPa.

Over the years, studies have contradicted each other as to the effect of retained austenite on RCF life, some showing increased fatigue life at the levels tested, Table II, and some showing decreased life with increases in initial retained austenite (14). Table II lists several researchers who found retained austenite to increase fatigue life. Murakami et. al. present a general explanation of the effect of retained austenite which takes both of these observations into account (18). Murakami et. al. state that there is an optimum amount of retained

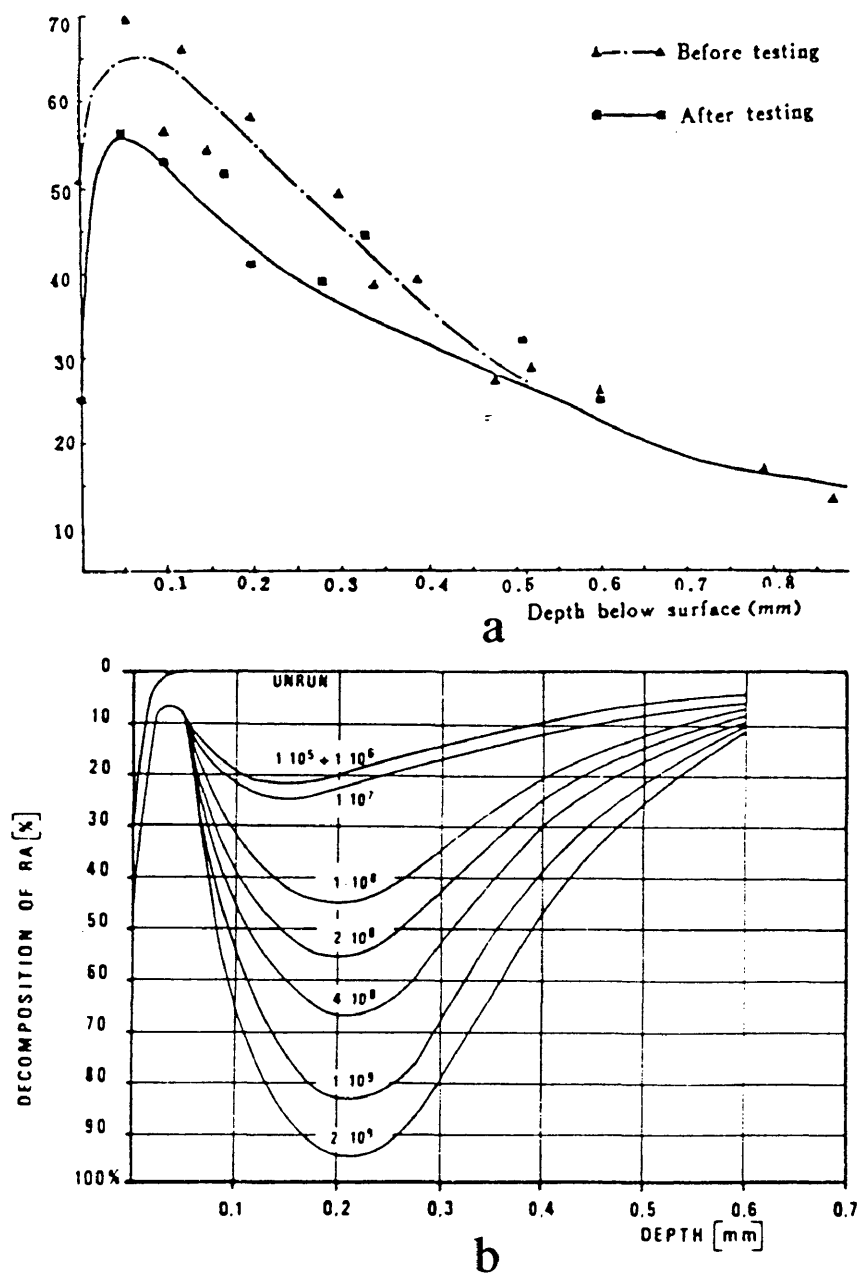


Figure 8: Reduction in retained austenite as a function of cycles a) reduction of surface retained austenite in a carburized steel (0.18%C, 1.50%Cr, 4.25%Ni, 1.0%W, case depth 2.5 mm) tested at a contact stress of 2800 MPa (20) b) reduction in retained austenite profiles in SAE 52100 bearings tested at a contact stress of 3300 MPa (21).

austenite for any application. Less than the optimum amount and more than the optimum amount result in decreased life. Figure 9 is from their work and shows L_{10} life as a function of volume percent retained austenite, with maximum L_{10} life at approximately 35 percent retained austenite for medium-carbon manganese containing bearings (1.2%-1.7%) tested in a Nippon Seiko ball bearing tester with a 600 kgf load.

Table II: Research Showing Beneficial Effect of Retained Austenite on Rolling Contact Fatigue

Researchers	Effect of Retained Austite	Steel Tested
Muro and Tsushima (19)	Retained austenite increases fatigue life	Various grades of carburized and bearing steels
Zhu et. al.	Good for low cycle fatigue	Carburized steel
Stickels and Janotik	Probably beneficial	52100 bearing steel
Stickels	Beneficial up to 20 % retained austenite	52100 bearing steel
Nahm	Beneficial	Carburized steel
Dong et. al.	Beneficial	Carburized steel

Beneficial effects of retained austenite are due to the austenite to martensite transformation taking up strain energy (19). Detrimental effects of retained austenite are due to dimensional instability caused by lattice expansion

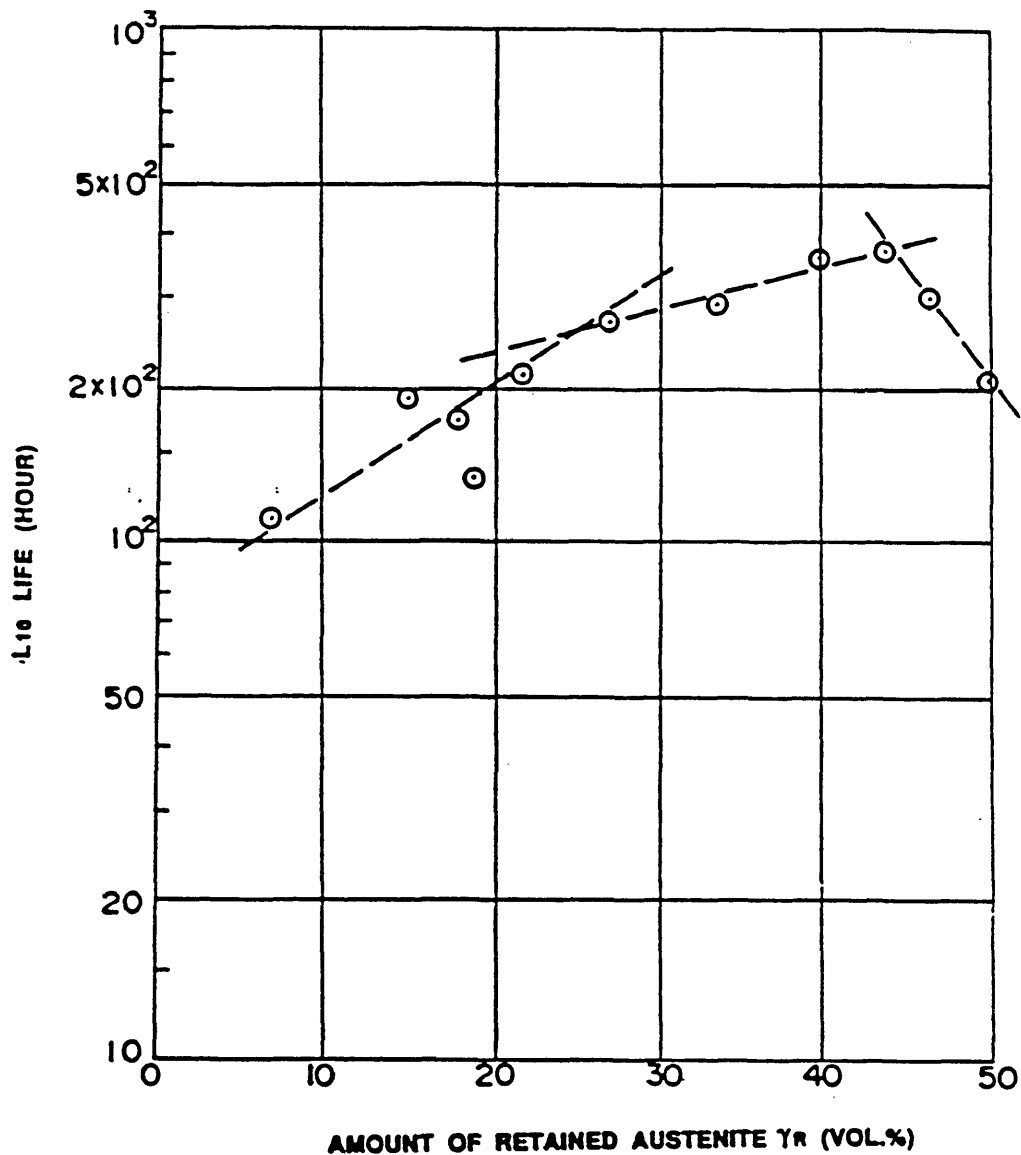


Figure 9: Ten percent failure, L_{10} life, as a function of initial volume percent retained austenite for medium-carbon manganese (1.2%Mn-1.7%Mn) bearings tested in a Nippon Seiko ball bearing tester with a 600 kgf load (18).

which results in surface waviness and premature spalling (14).

2.5 Residual Stress Changes

Several researchers have tracked residual stress changes as a function of the number of cycles, Figure 10 through Figure 14 (19,20,21,22,23). The magnitude of the residual stresses and when they occur vary from paper to paper, but the overall trend is as shown in Figure 10 and Figure 11. Figure 10 is a plot of surface residual stress versus cycles for carburized bearings (0.18%C, 1.50%Cr, 4.25%Ni, 1.0%W), case depth 2.5 mm, tested at a contact stress of 2800 MPa. The surface residual stresses stay approximately constant until about 10^5 cycles, then they become increasingly more compressive. Figure 11 is for SAE 52100 bearings tested at a contact stress of 3300 MPa and shows changes in residual stress profiles as a function of cycles. The residual stresses become increasingly more compressive in the region of maximum τ_{45} as cycles increase. Figure 12 shows surface residual stress as a function of cycles for carburized nickel-chromium steel (0.18%C, 0.27%Si, 0.51%Mn, 0.012%P, 0.020%S, 0.07%Cu, 2.21%Ni, 0.35%Cr) tested at a contact load of 220 kgf/mm². The curves in Figure 12 follow the trend of Figure 10 which

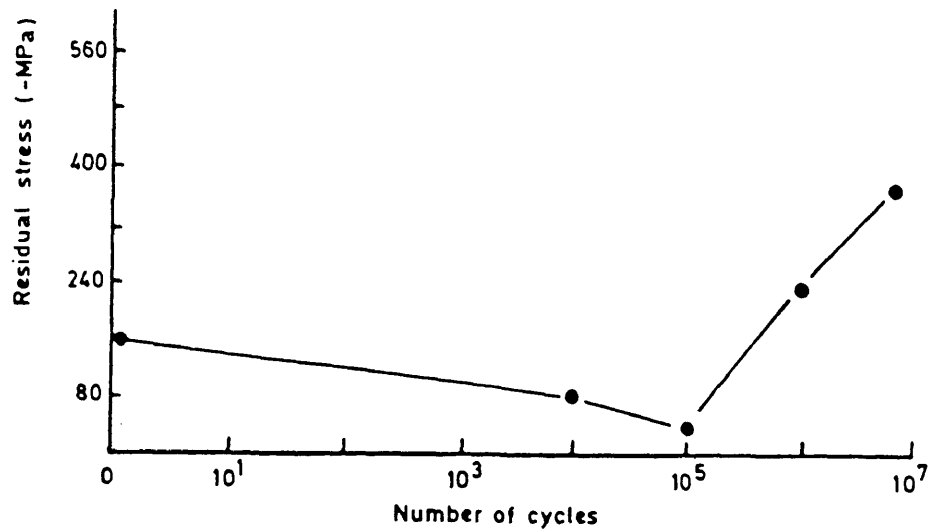


Figure 10: Surface residual stress versus cycles for carburized bearings (0.18%C, 1.50%Cr, 4.25%Ni, 1.0%W), case depth 2.5 mm, tested at a contact stress of 2800 MPa (20).

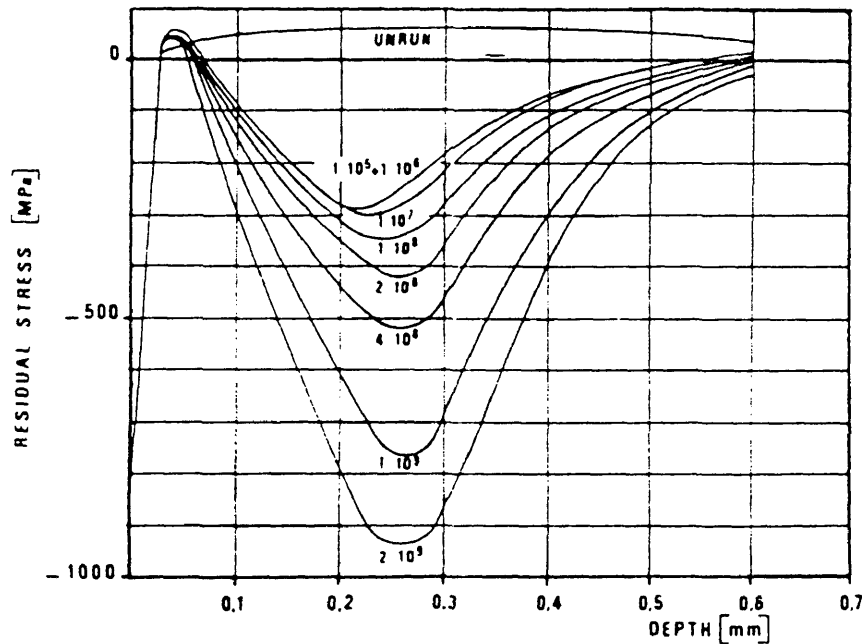


Figure 11: Residual stress profiles as a function of cycles for SAE 52100 bearings tested at a contact stress of 3300 MPa (21).

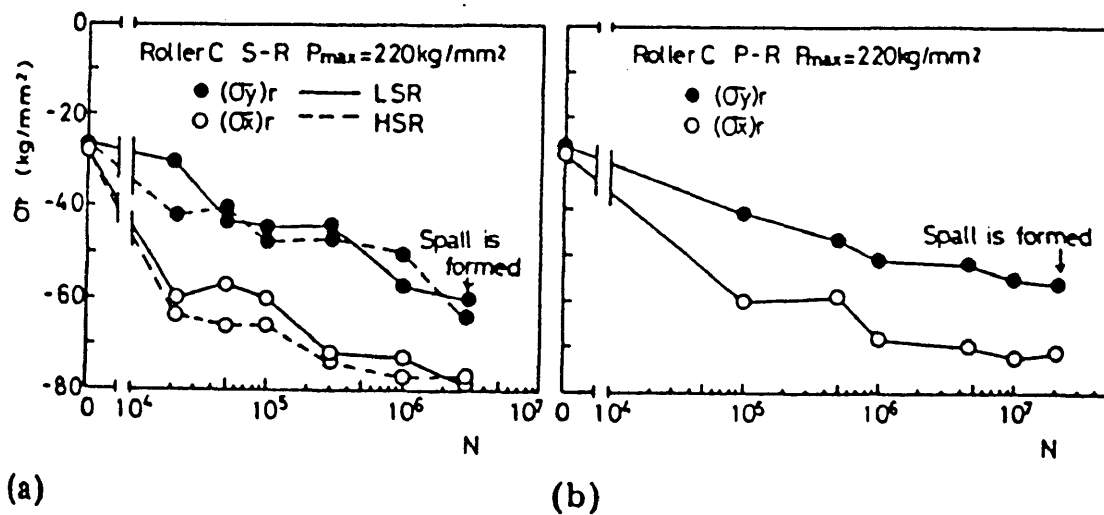


Figure 12: Surface residual stress as a function of cycles for carburized nickel-chromium steel (0.18%C, 0.27%Si, 0.51%Mn, 0.012%P, 0.020%S, 0.07%Cu, 2.21%Ni, 0.35%Cr) tested at a contact load of 220 kgf/mm² a) S-R stands for sliding, LSR (-25.7%) and HSR (+20.5%) b) P-R stands for pure rolling (22).

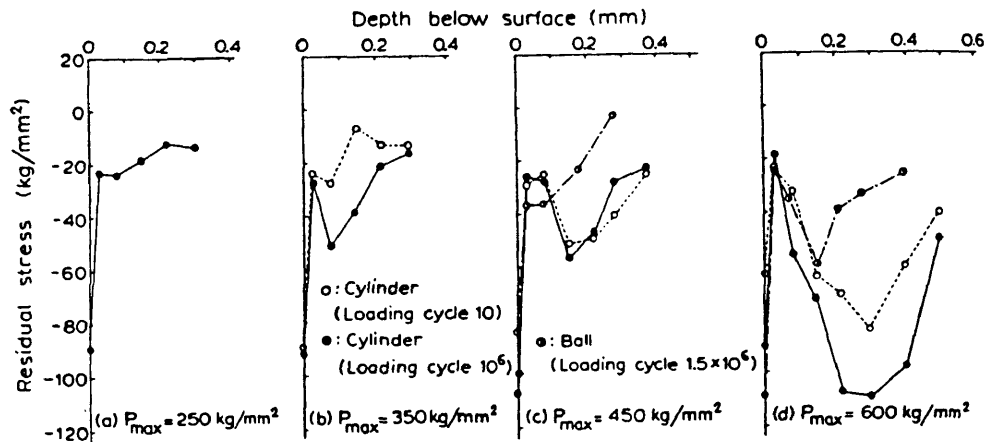


Figure 13: Changes in residual stress profiles during rolling contact fatigue for a carburized steel, case depth 1 mm, tested under various loading conditions, 250 kgf/mm² to 600 kgf/mm² (19).

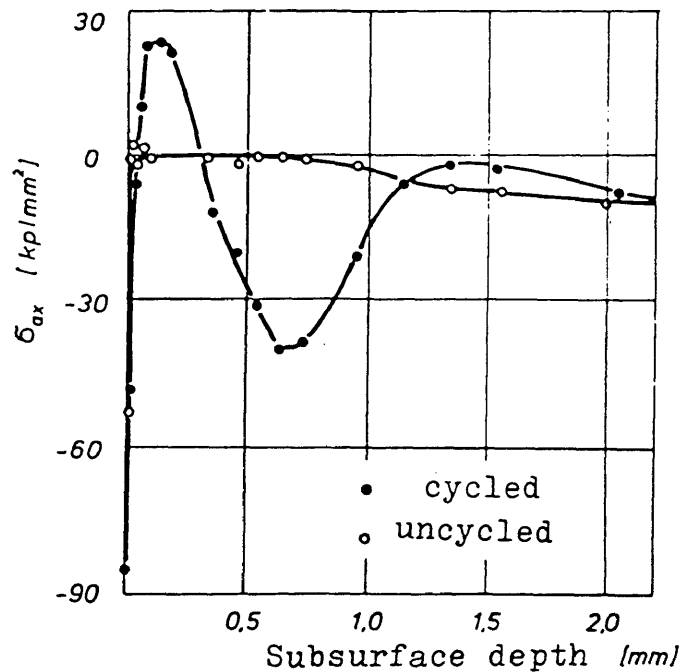


Figure 14: Changes in residual stress profiles during rolling contact fatigue for SAE 52100 steel tested at a contact stress of 2550 MPa (23).

is toward high surface compressive residual stress as cycles increase. Figure 12a is for sliding LSR (-25.7%) and HSR (+20.5%) and Figure 12b is for pure rolling. Figure 13 shows changes in residual stress profiles for a carburized steel, case depth 1 mm, tested under various loading conditions, 250 kgf/mm² to 600 kgf/mm². Figure 14 is for SAE 52100 tested at a contact stress of 2550 MPa.

Strain hardening and residual stress changes have been shown to occur in both carburized steel, Figure 13 (19) and through hardened bearing steel, Figure 14 (23). Depending on whether the steel is carburized or through-hardened, tensile residual stresses are produced or increased during RCF between the region of maximum shear stress, where residual stresses become more compressive, and the surface, Figure 14. Severe strain hardening of the steel matrix and thus large residual stress changes have been shown to occur even in ultra clean steels (24,25).

2.6 Hardness Changes

The hardness profile of a material subjected to RCF at first shows an increase, Figure 15, as residual stress, Figure 10, is becoming more compressive. Figure 15 is for a carburized nickel-chromium steel (0.18%C, 0.27%Si, 0.51%Mn, 0.012%P, 0.020%S, 0.07%Cu, 2.21%Ni, 0.35%Cr)

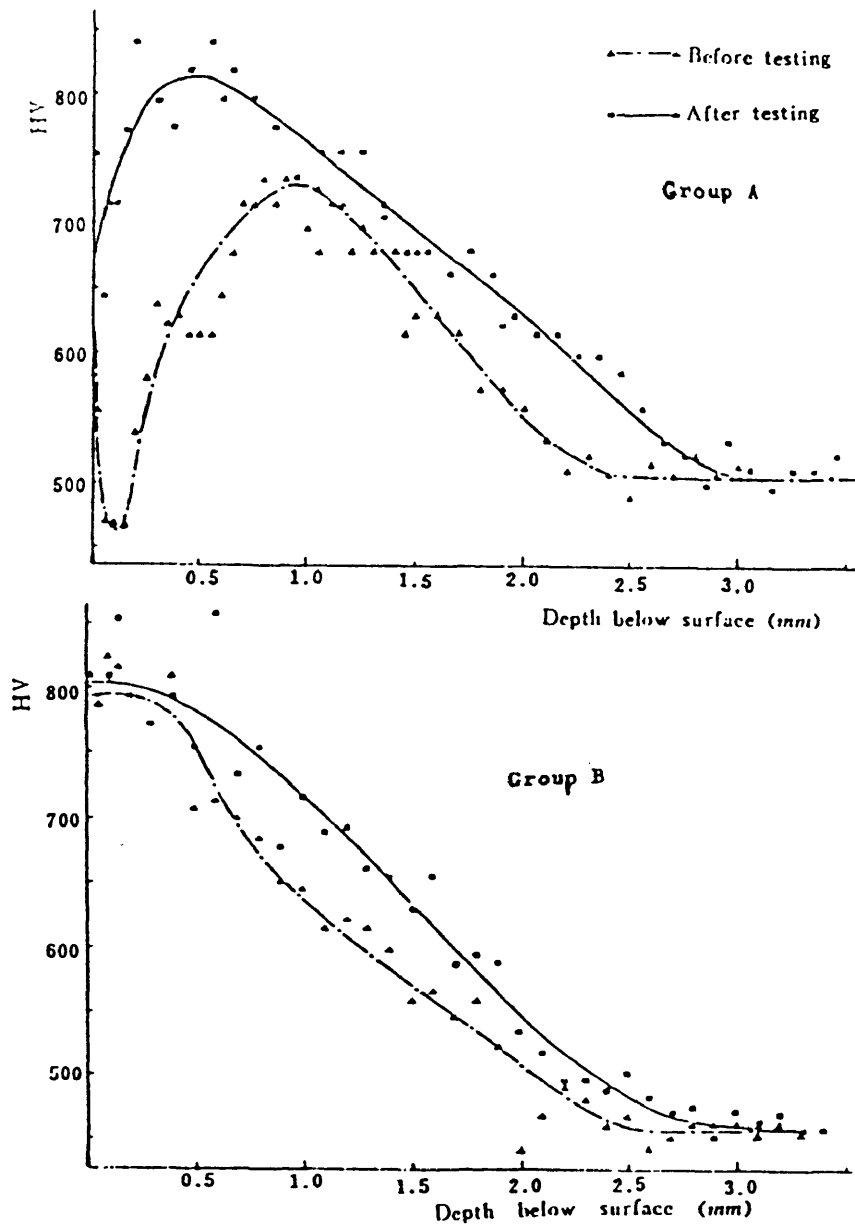


Figure 15: Changes in hardness profiles during rolling contact fatigue for two groups of a carburized nickel-chromium steel (0.18%C, 0.27%Si, 0.51%Mn, 0.012%P, 0.020%S, 0.07%Cu, 2.21%Ni, 0.35%Cr) tested at a contact load of 220 kgf/mm² a) group A contains 50% initial retained austenite b) group B contains 7% initial retained austenite (20).

tested at a contact load of 220 kgf/mm² (20). Group A, Figure 15a, had 50% retained austenite and group B, Figure 15b, had 7% retained austenite which resulted in a difference in the initial hardness profile. After testing, the hardness profiles were similar, except for lower surface hardness in group A.

After some number of cycles, hardness profiles decrease. Figure 16, from Swahn et. al. for SAE 52100 steel tested at a contact stress of 3720 MPa, shows the hardness profile at 10⁷ cycles falls below that of the untested profile. The hardness decreases may be in part due to a relaxation of residual stresses. However, this is not known because residual stress profiles past 10⁷ cycles were not found in the literature. Figure 16 shows that as the number of load cycles increases hardness drops most in the areas of structural change and the minimum in hardness is found closer to the surface (26).

2.7 Dark Etching Regions

The first macroscopic etching effect is a dark etching region (DER) formed beneath the contact surface, usually sometime after 10⁷ cycles, as shown schematically in Figure 17 (26). Figure 17 is a diagram produced by Swahn et. al. from work on SAE 52100 type 6309 ball bearings. The

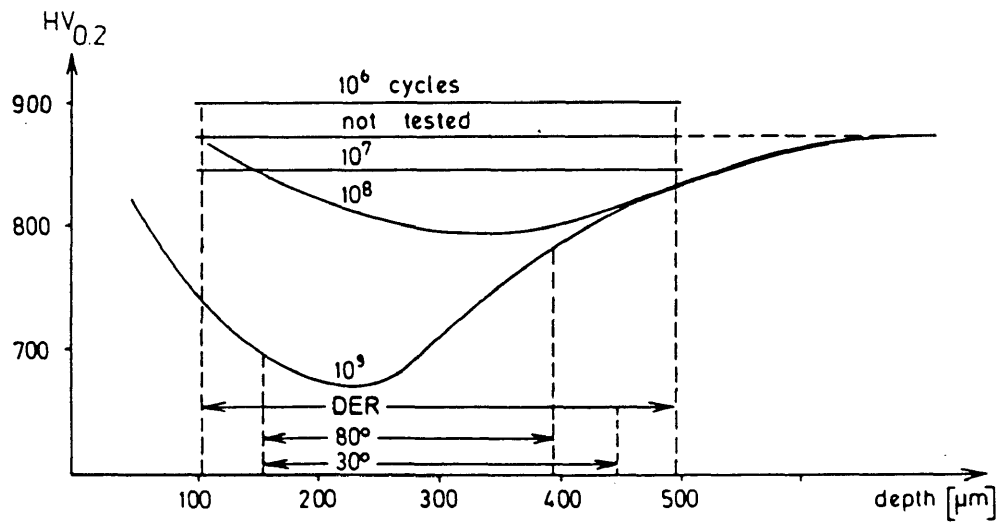


Figure 16: Changes in hardness profiles during rolling contact fatigue of SAE 52100 type 6309 ball bearings tested at a contact stress of 3720 MPa (26).

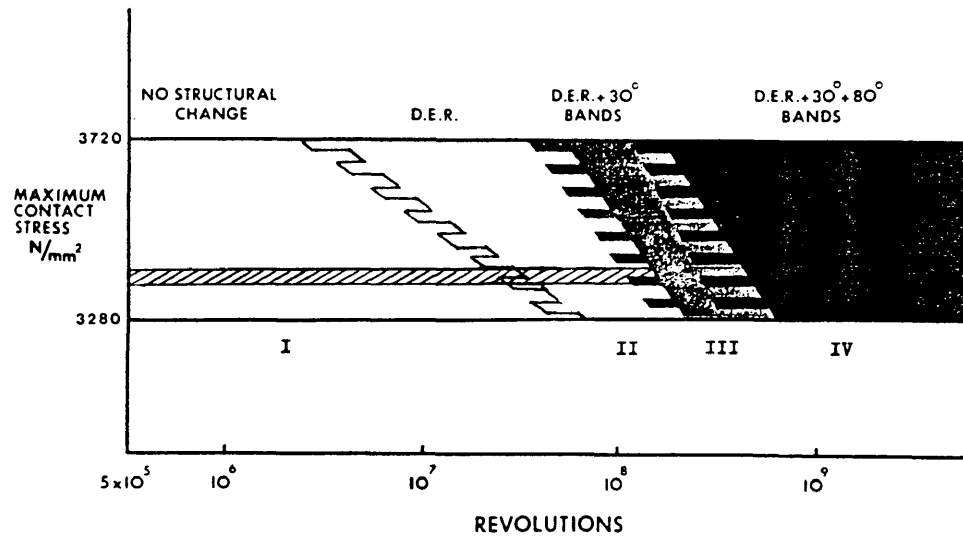


Figure 17: Diagram produced by Swahn et. al. from work on SAE 52100 type 6309 ball bearings. This diagram shows a relationship between contact stress, number of cycles, and microstructural changes (26).

diagram shows a relationship between contact stress, number of cycles, and microstructural change, and will be used later to provide a framework for the results presented in this thesis. The range of contact stress applied to some of the specimens tested in this work is shown as a horizontal band.

Dark etching regions (DER) occur in the region of maximum τ_{45} from just below the surface to a point deeper in the case, Figure 18 (21). At first, "patches" of transformed areas are seen, Figure 18a. The rest of the region transforms over time, Figure 18b and 18c. Figure 18 parts a,b, and c are on the xz plane through a SAE 52100 specimen tested at a contact stress of 3720 MPa. Figure 18d is on the yz plane of a SAE 52100 steel tested at a contact stress of 2550 MPa and shows the general shape of a DER. Dark etching regions are composed of martensite, ferrite (decomposed martensite), and retained austenite and differ slightly in shape depending upon the stress state imposed during RCF (11,19,21,22,26,27). The ferrite that forms is thermodynamically strongly supersaturated in carbon, though not in ordinary solution (26).

The initial region of highest σ_e correlates well with the DER, Figure 19a (28,29). Figure 19a shows the original distribution of σ_e , dashed line, and the distribution of σ_e

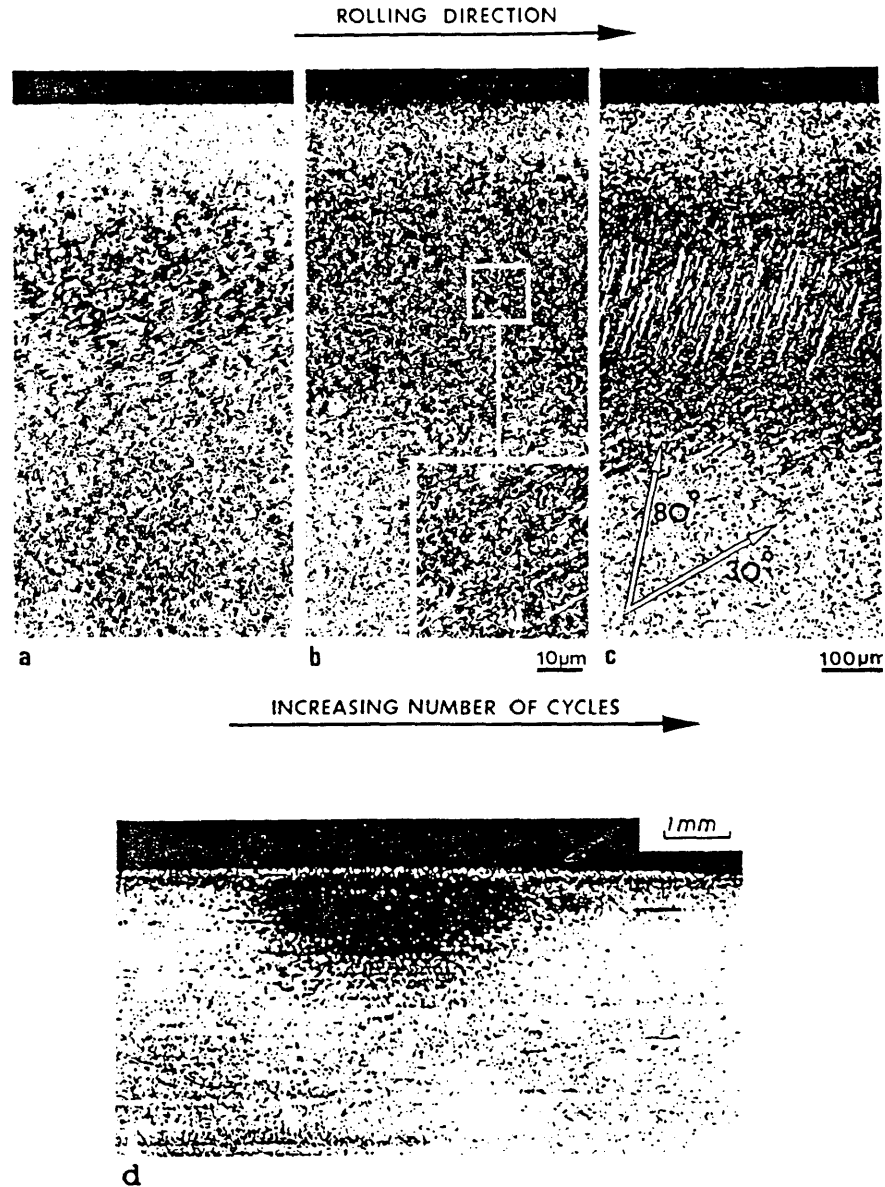


Figure 18: a-c) Progression of dark etching region and formation of 30 and 80 degree bands on the xz plane of a SAE 52100 steel tested at a contact stress of 3720 MPa (26) d) dark etching region on yz plane of SAE 52100 steel tested at a contact stress of 2550 MPa (23).

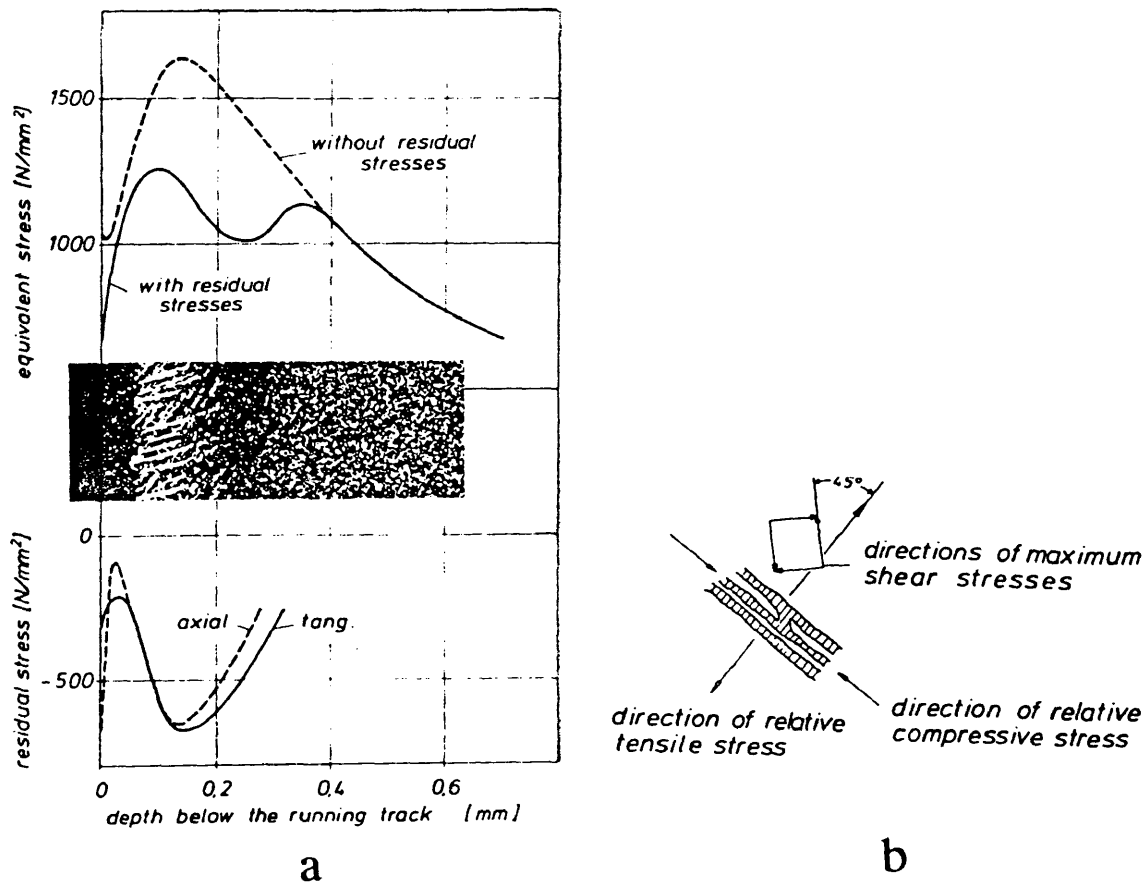


Figure 19: Explanation of the formation of 30 and 80 degree bands in terms of an effect on the distribution of σ_e and τ_{45} as a function of the imposed residual stresses during rolling contact fatigue a) distributions of σ_e before and after residual stresses and distribution of imposed residual stresses b) residual stress effect rotates the principal stresses 30 degrees such that a relative tensile stress acts perpendicular to the 30 degree direction and τ_{45} acts in the 80 degree direction (28).

after the residual stress distribution is entered into the calculation of σ_e (28). The relative amounts of martensite and DER ferrite depend upon the number of stress cycles (26). Because the DER forms in the region of highest σ_e (same as region of highest τ_{45}) and is a function of cycles, it has been concluded that the martensite to ferrite transformation is induced by the shear stresses (30).

One of the first researchers to observe dark etching regions was Jones (30). He called these areas mechanical "troostite". Troostite is an archaic term proposed by Jones to describe a previously unresolvable rapidly etching fine aggregate of carbide and ferrite. Now troostite is called either tempered martensite or fine pearlite. A synonym for troostite is sorbite, also an archaic term. The DER etches dark with a nital etch because of differences in the way that the martensite and DER ferrite etch leaving a rough surface.

Sometimes, dark etching bands are seen in the DER. Muro et. al. calls them dark needles and dark lines. When they are seen, it is usually at high stresses (19).

2.8 Nonmetallic Inclusions

There are several different types of nonmetallic inclusions:

- Sulfides
- Hard Alumina
- Silicates
- Globular Hard Oxides

It is known that hard inclusions adversely affect the rolling strength of steel. This phenomenon has been attributed to a notch effect associated with these inclusions (31,32). This notch effect has also been shown to locally increase the compressive residual stresses (14). Sulfides, which are soft, are considered to have a much smaller effect on RCF. They often deform plastically, whereas, oxide inclusions are brittle (33).

Some data suggest that the melting process may have a far stronger influence on rolling element fatigue life than the material chemistry (34). Vacuum degassing and several other techniques result in cleaner steels by reducing the size and number of oxide inclusions. Improvements in bearing steel fatigue life by a factor of 8 for 52100 steel and 2 for M50 steel (35) were observed with the progression from air melt to vacuum arc remelt (VAR) to vacuum induction melt-vacuum arc remelt (VIM-VAR) processing.

Control of grain flow during forming also enhances fatigue life. This may be due to the influence of fiber

orientation, namely the orientation and elongation of nonmetallic inclusions, upon the rolling contact fatigue life (35).

2.9 White Etching Areas

White etching areas are considered to form due to the dissolution of fine transition carbides in the tempered martensite of hardened bearing and carburized steels and the diffusion of carbon to areas of highest dislocation density (26,36). This process produces ferrite, which etches white, in contrast to tempered martensite which etches dark. High dislocation density areas are produced by RCF shear stresses over time and the increased hydrostatic stresses during RCF are thought to enhance diffusion (26). This mechanism is supported experimentally by the fact that the area around some hardness indentations etches white, Figure 20 (37). Figure 20 shows an etched hardness indentation in a Fe-1.2C steel.

There are several different types of white etching areas. First, there are butterflies, which form around alumina and oxide inclusions. Second, there are 30 degree bands which form in the DER of RCF samples and lastly, there are 80 degree bands which form on top of the 30 degree bands in the DER. White etching areas are 3

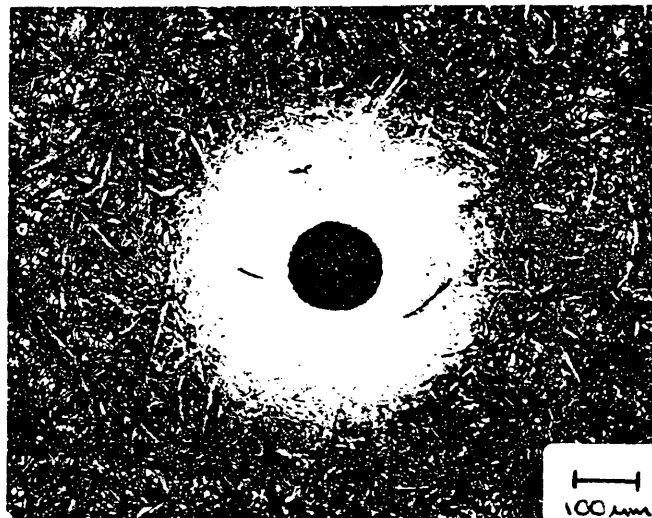


Figure 20: Etched hardness indentation showing white etching areas in a Fe-1.2C steel (37).

dimensional in nature. Thus it is important to look at the xz , yz , and xz planes to fully characterize their shape. The angle of orientation of white etching bands is the angle that the band makes with the contact surface in the xz plane, Figure 18c. A very seldom shown view is the xy plane, due to the difficulties involved in removing layers from the surface.

Orientations of white etching bands in the xz plane vary slightly depending on contact geometry, surface traction during RCF, imposed residual stresses, and depth within the DER (19,21,26,38). Differences of several degrees as reported by various investigators are shown in Table III (19,21,38).

White etching bands slant upwards towards the surface in the direction of rolling. Hahn et. al. offers an explanation why the bands form in the rolling direction and not in the opposite direction by showing that plastic flow is more prominent in the direction of rolling (38).

Table III: Reported Inclinations of White Etching Bands
Relative to the Rolling Contact Fatigue Surface

Reference	30 Degree Bands	80 Degree Bands
Voskamp (21)	20° to 32°	75° to 85°
Swahn, Becker, and Vingsbo (26)	30°	80°
Bush, Grube, and Robinson	30°	_____
Martin, Borgese, and Eberhardt (11)	22° to 24°, 30°	_____
Lund	_____	65° to 70°

2.9.1 Butterflies

Butterflies are sets of white etching bands which extend from alumina and oxide inclusions (31,39). The bands resemble the wings of a butterfly, Figure 21, and are usually oriented at 45 degrees to the contact surface, suggesting that they are due to a local increase in dislocation density produced by the τ_{45} shear stress and by the stress concentration of the inclusions. Figure 21 shows a typical butterfly around a hard inclusion particle at 45 degrees to the contact surface in SAE 52100 steel tested at a contact stress of 2550 MPa. The lowest angle of orientation reported for a butterfly was 25 degrees to the contact surface (39). Butterflies are often seen at high numbers of cycles and at high stress levels and have



Figure 21: A typical butterfly at 45 degrees to the contact surface around a hard inclusion particle in SAE 52100 steel tested at a contact stress of 2550 MPa (33).

an incubation stage similar to the bands discussed below (31,33,39). Once the butterfly forms, the "wings" of the butterfly grow as a function of cycles and cracking often originates at the edges of the wings (31,33).

2.9.2 30 Degree Bands

After the DER is well established, as shown by Swahn et. al., Figure 17, 30 degree bands of ferrite appear in the DER, Figure 18b. Transmission electron microscopy showed that inside these 30 degree bands, the dislocation density is very low (26). Along the sides of the bands are lenticular carbides (11,26). Lenticular carbides having a 30 degree orientation are also sometimes seen by themselves amongst the white etching bands. The 30 degree bands consist of ferrite in thermodynamic equilibrium with respect to carbon (26).

Zwirlein and Schlicht have given an explanation of the 30 degree bands in terms of a "crack opening" type of relative tensile stress, Figure 19b (28). Figure 19b illustrates the stresses acting to form a 30 degree band. According to their theory, induced residual stresses during RCF alter the orientation of the principal stresses such that this can occur. However, other researchers believe that the τ_{45} shear stress causes the 30 degree bands to form (11,21,26).

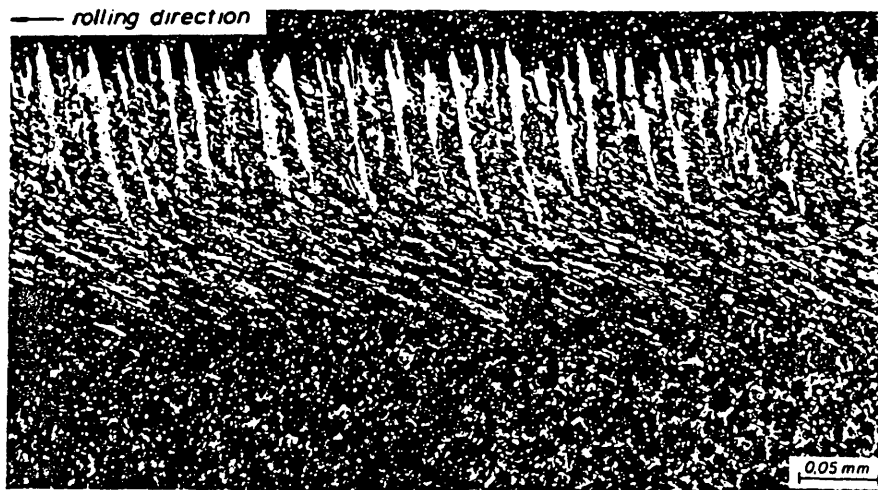


Figure 22: xz plane through the middle of the wear track of a SAE 52100 specimen cycled into Stage IV. The 80 degree bands usually occur in the upper portion of the 30 degree bands (28).

2.9.3 80 Degree Bands

After the formation of the 30 degree bands, 80 degree bands form on top of them in the DER, Figure 18c and Figure 22. Figure 22 shows a xz plane through the middle of the wear track of a SAE 52100 specimen cycled into Stage IV. The 80 degree bands are similar to the 30 degree bands except the ferrite has a very high dislocation density and the carbon content is lower than in the 30 degree bands (26). 80 degree bands are usually concentrated towards the top of the DER, whereas 30 degree bands often cover the width of the DER, Figure 22.

As a result of their 30 degree band explanation (28), Zwirlein and Schlicht have given an explanation for the 80 degree bands in terms of τ_{45} . According to Zwirlein and Schlicht, induced residual stresses alter the orientation of the principal stresses such that τ_{45} occurs at an angle of 80 degrees with respect to the contact surface, Figure 19b. Although other investigators disagree that τ_{45} causes the 80 degree bands, there is agreement that the 80 degree bands are produced by a shear mechanism (21,26,29).

2.9.4 Cracking and White Etching Areas

At the end of Stage IV in Figure 17, assuming that no cracks initiated at inclusions, cracking begins along the 30 and 80 degree bands (26), Figure 23 and Figure 24.

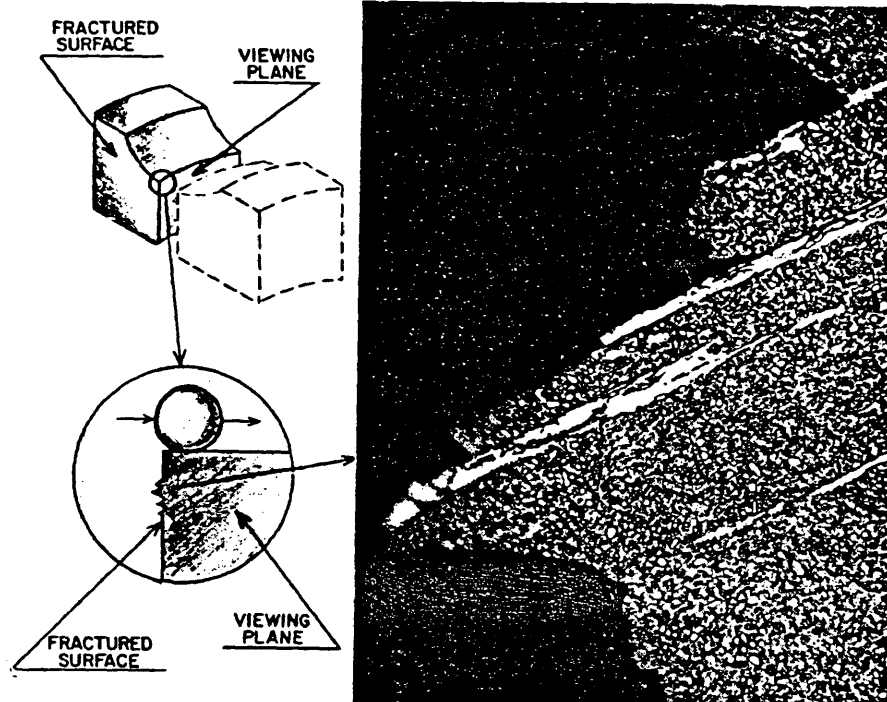


Figure 23: A crack along a 30 degree band (second from the top) in 52100 steel (11).



Figure 24: Cracks along 30 and 80 degree bands culminating in a "v" shaped spall in carburized steel (0.19%C, 0.24%Si, 0.85%Mn, 0.006%P, 0.010%S, 1.14%Cr, 0.046%Al, 0.020%N, 0.0009%O), case depth 1.3 mm, tested at a contact stress of 600 kgf/mm² (65).

Figure 23 is of a crack along a 30 degree band in 52100 steel and Figure 24 shows cracks along both directions in a carburized steel (0.19%C, 0.24%Si, 0.85%Mn, 0.006%P, 0.010%S, 1.14%Cr, 0.046%Al, 0.020%N, 0.0009%O), case depth 1.3 mm, tested at a contact stress of 600 kgf/mm².

Cracking is also known to originate from the edges of butterflies (31,33). When the cracks coalesce, then spalling occurs as shown by the "v" shaped spall in Figure 24. White etching areas, not related to those discussed previously, are also sometimes seen along cracks and seem to be a result of the cracks (40).

2.10 Classic Papers on Microstructural Change Due to RCF

Jones's 1946 paper was the earliest paper that the author found on the subject of microstructural changes due to RCF. Jones wrote of a dark etching region that developed in the material after a significant amount of rolling on 52100 samples at high stresses. He called this dark etching region mechanical troostite (30). M. Kuroda, 1960 (41), and Bush et. al., 1961 (42), reported similar results in 52100 steel. Johnson and Merwin (43) and Almen (44), 1963, proposed a RCF failure mechanism based on residual stress changes. Martin, Borgese, and Eberhardt of SKF, 1966, were the first to describe white etching areas

using transmission electron microscopy (11).

The most complete summaries of microstructural changes due to RCF are by Muro and Tsushima, 1970 (19), and Swahn, Becker, and Vingsbo, 1976 (26). The current work utilizes Swahn et. al.'s diagram of microstructural change versus cycles; termed here the S-B-V diagram, Figure 17. Rousseau et. al., 1982, cover the effects of nonmetallic inclusions (33). Voskamp, also 1982, outlined a qualitative model for the development of rolling contact fatigue (21). However, Zwirlein and Schlicht, 1982, give the best explanation of how 30 and 80 degree bands develop (28).

2.11 Experimental Matrices

The range of experimental matrices encountered in RCF literature is varied. Therefore, it is difficult to compare much of the research done (1). To illustrate this point, Table IV shows contact stress and rolling speed used in several different studies. White etching bands are observed in both carburized and through-hardened bearing steels (19,20,21,22,23). Various levels of retained austenite are obtained by varying the heat treatment.

Many researchers use Weibull analysis to determine the statistical significance of their findings (45). This involves taking RCF samples to failure and results in a

plot such as Figure 25. Figure 25 shows schematically the Weibull plots for two groups of specimens. Group B has better fatigue resistance. The dashed lines are confidence bands.

Table IV: Variation in RCF Stress and Rolling Speed

Researchers:	Machine Used	Contact Stress	Speed
Bamberger and Clark (3)	GE RC Rig	4826 MPa	12,500 rpm
Thom	Polymet RC Rig	4826 MPa	10,000 rpm
Glover	Federal-Mogul Ball-Rod RCF Tester	5420 MPa	3,600 rpm
Ito et. al.	Cylinder to Ball	5880 MPa	22,677 rpm
Lamothe et. al.	GRTM	3102 MPa	1,330 rpm
Miller (this work)	Timken RC Rig	4146 MPa, 3380 MPa	8,900 rpm

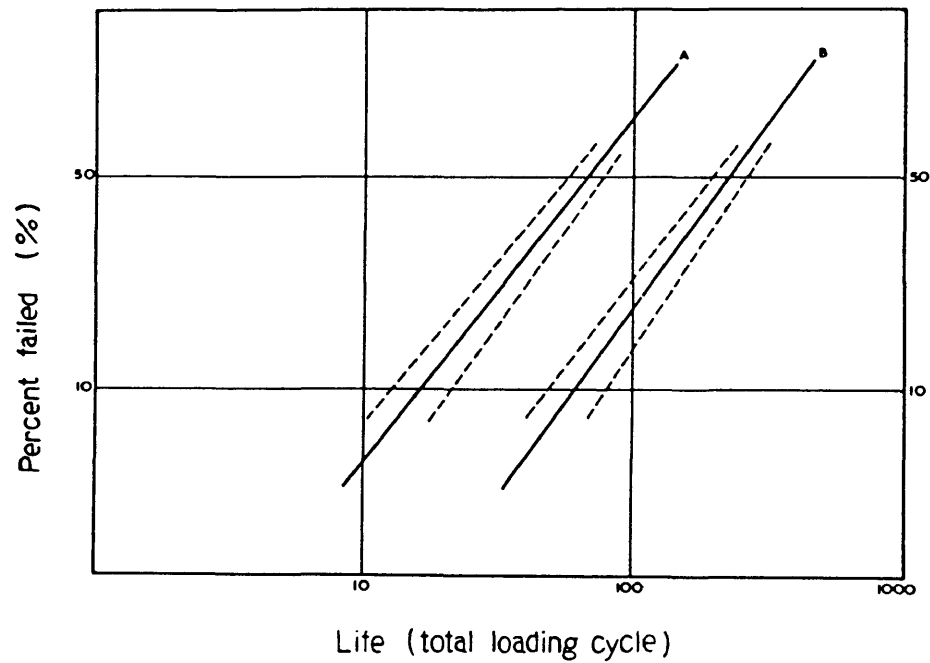


Figure 25: A schematic Weibull plot showing the fatigue resistance for two groups of specimens. Group B has better fatigue resistance, the dashed lines are confidence bands (66).

3.0 EXPERIMENTAL DESIGN, MATERIAL, AND SPECIMEN DESIGNATIONS

This investigation was designed to systematically evaluate changes introduced into carburized steel by RCF. Table V gives the composition of the steel specimens. Two heat treated conditions were tested.

Table V: Composition in Weight Percent of AISI 8620 Steel

C	Mn	P	S	Si	Cr
0.20	0.80	0.011	0.014	0.25	0.53
Ni	Mo	Cu	Al	Ti	
0.62	0.19	0.20	0.029	0.013	

One heat treatment consisted of direct quenching after carburizing (D) and the other consisted of reheating and quenching after carburizing (R), Table VI. Two groups of carburized specimens were tested. The first group was carburized and reheated by Timken. Thus these specimens are identified by the letters (TR). This group was tested at a contact stress of 4146 MPa with a 2.5 cm (1 in) crown radius on the rollers. The second group was carburized by Caterpillar and consisted of direct quenched (CD) and reheated specimens (CR). Therefore, these specimens are identified by the letters CD or CR. Reheating was expected to reduce retained austenite, an important factor regarding RCF performance as discussed earlier. The Caterpillar

specimens were tested at a contact stress of 3380 MPa with a 7.6 cm (3 in) crown radius on the rollers. Specimens were carburized to a case depth of 2 mm and tested at high contact stresses to various numbers of cycles, Table VI. Table VI lists the designations and the loading conditions for specimens tested in this study. Close to ideal conditions were applied by providing ample lubrication and holding the speed, temperature, and load (during each test) as constant as possible (7,23). The lubricant was not heated. The temperature of the oil was about 50 degrees C. Eleven of the initial 12 bars were used, 6 wear tracks more were done than are shown in Table VI.

Table VI: Experimental Matrix and Specimen Designations

Material	Specimen Designation		
	Cycles	Direct Quench	Reheat
Timken Specimens (TRXX) 4146 MPa Contact Stress 2.5 cm (1 in) Crown Radius	0		TR01
	2.8×10^8		TR32
	1.0×10^9		TR41
Caterpillar Specimens (CDXX)/(CRXX) 3380 Mpa Contact Stress 7.6 cm (3 in) Crown Radius	0	CD01	CR01
	10^1	CD11	CR11
	10^2	CD12	CR12
	10^3	CD13	CR13
	10^4	CD21	CR21
	10^5	CD22	CR22
	10^6	CD23	CR23
	10^7	CD31	CR31
	10^8	CD32	CR32
	0.5×10^9	CD33	CR33
	1.4×10^9		CR41

Table VI: Experimental Matrix and Specimen Designations
(Transposed)

Cycles ⇒	0	10	10^2	10^3	10^4	10^5
(TRXX)	TR01					
(CDXX)	CD01	CD11	CD12	CD13	CD21	CD22
(CRXX)	CR01	CR11	CR12	CR13	CR21	CR22

	10^6	10^7	10^8	$5 \cdot 10^8$	10^9	$5 \cdot 10^9$
			TR32 $2.8 \cdot 10^8$		TR41	
	CD23	CD31	CD32	CD33		
	CR23	CR31	CR32	CR33	CR41 $1.4 \cdot 10^9$	

Three wear tracks were produced on each 15.2 cm long bar. Thus CD11-CD13 are from the same bar, CD21-CD23 are from another bar and so on.

3.1 Timken Rolling Fatigue Machines

The two Timken Rolling Contact Fatigue Machines (TRFM) used in this experiment were donated by the Timken Company and installed at CSM. The machines operate at 8900 revolutions per minute (17800 fatigue cycles per minute). Loading is accomplished by a hydraulic cylinder which in turn is driven by shop air. Hydraulic fluid applies force to a tension bolt at the top of a "nut cracker" arrangement similar to Figure 2. Figure 26 illustrates the initial

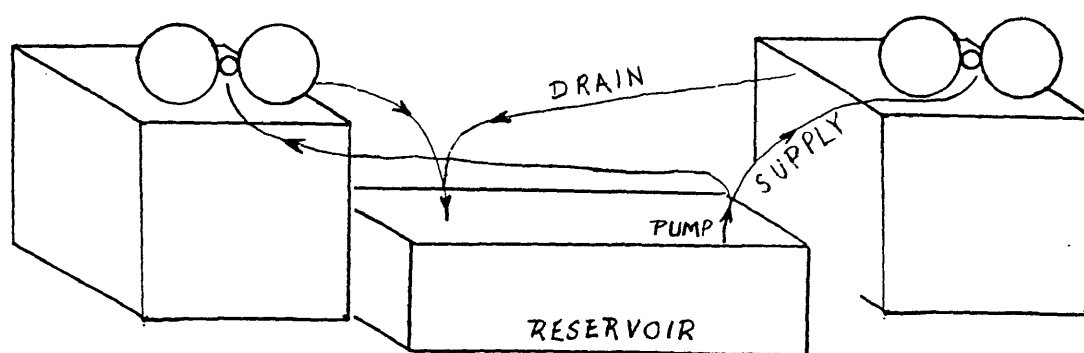


Figure 26: Illustration of the initial lubrication system for the Timken Rolling Fatigue Machines installed at the Colorado School of Mines in which the lubricant was originally pumped from a reservoir tank directly into the contact regions. This lubrication system was inconsistent and difficult to regulate.

lubrication system. Lubrication was originally provided by a ground level pump, which pumped from a reservoir tank directly into the contact regions. This lubrication system had a tendency to clog was difficult to regulate.

Therefore, Figure 27, an overhead gravity feed system was designed and manufactured. This system automatically compensates for changes in the lubricant flow. Should the nozzles in the contact region become clogged, there is a buildup of oil in the overhead reservoirs. Once the pressure increases, the clog is dislodged and normal flow returns over time. New load cells were built by John Shepic of Denver, Colorado and a VeederRoot electronic cycle counter was installed. The new load cells showed that there were fluctuations in loading during start-up and during testing. Figure 28 shows a typical load versus time graph. The subject of loading during machine start-up is discussed in the Appendix.

Some sliding occurs in all rolling contact. A small amount of positive sliding occurs on specimens tested in the TRFM machine. The difference between positive and negative sliding is that in positive sliding the specimen drives the roller and the surface velocity of the specimen is greater than that of the roller and in negative sliding the roller drives the specimen and the surface velocity of

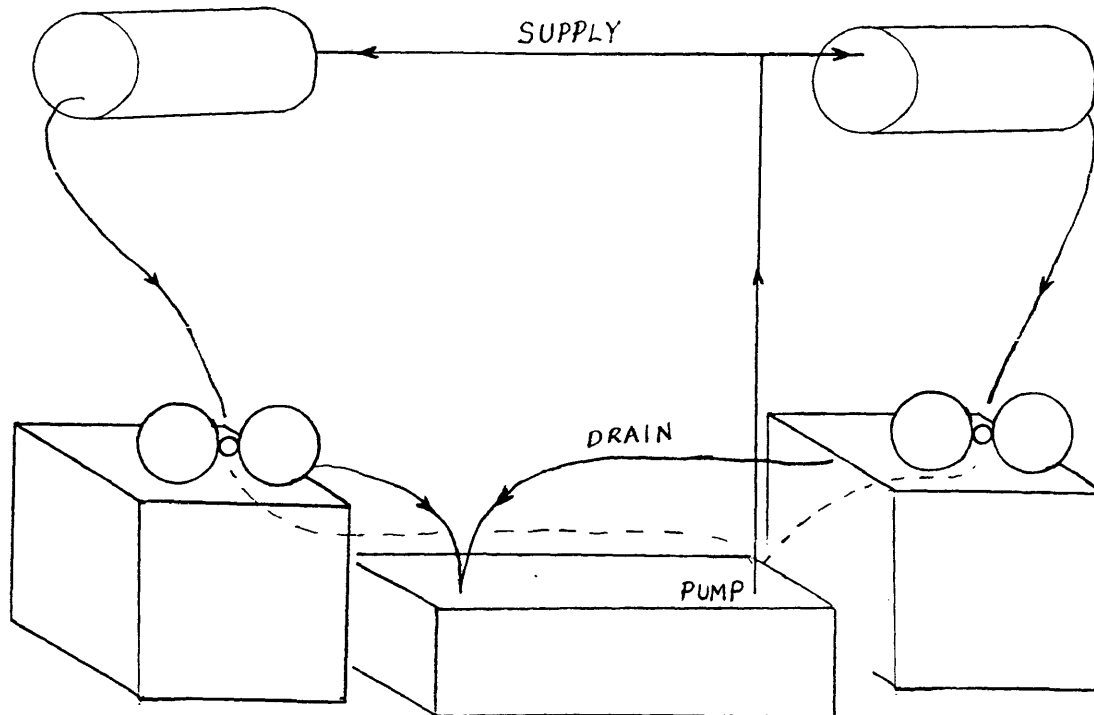


Figure 27: Illustration of gravity-feed replacement lubrication system for the Timken Rolling Fatigue Machines installed at the Colorado School of Mines in which the system automatically compensates for changes in the flow. Should the nozzles in the contact region become clogged, there is a buildup of lubricant in the overhead reservoirs. Once the pressure increases, the clog is dislodged and normal flow returns over time.

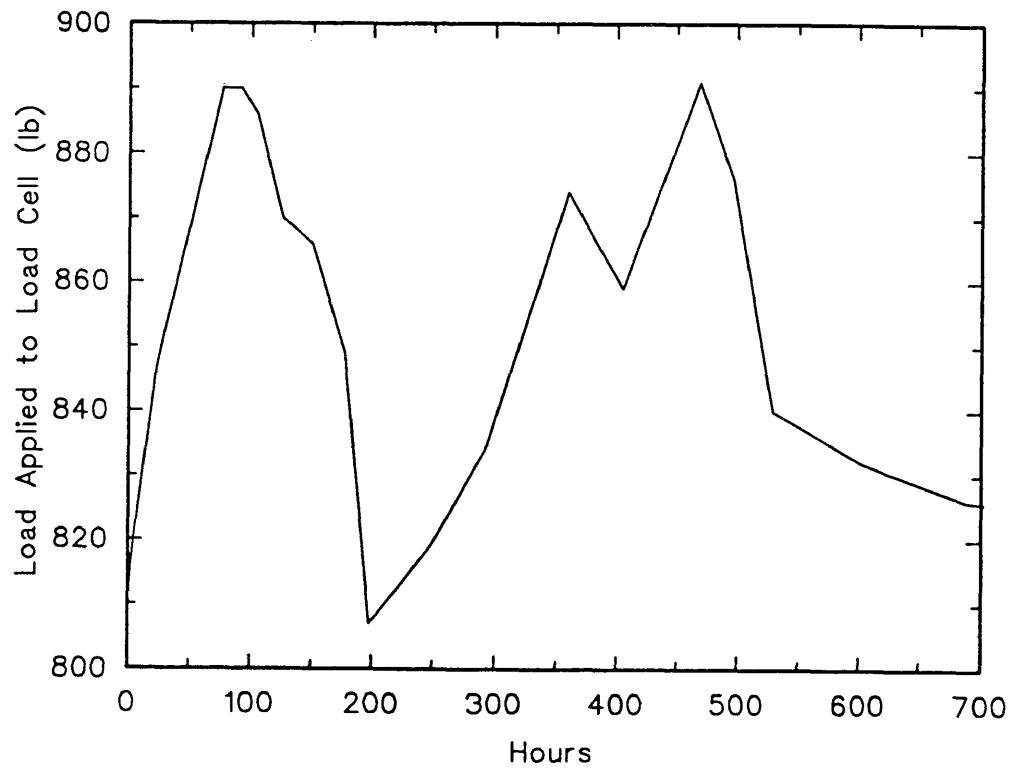


Figure 28: A typical load versus time graph during start-up for the Timken Rolling Fatigue Machines installed at the Colorado School of Mines. Note an initial spike in the loading followed by fluctuations due to adjustments before the loading settles near 850 lb.

the specimen is less than that of the roller. An example of negative sliding is the sliding that occurs at the roots of gear teeth and tends to open surface initiated cracks (7,46).

3.1.1 Toroid Rollers

The rollers of these machines have several characteristics worth noting. First is wear. After some number of cycles they should be reground to maintain the crown radius and surface finish (5,47). The crown radius is the radius of curvature of the toroid roller as shown in Figure 29. Figure 29 shows a specimen and the toroid rollers of a TRFM. As the crown radius increases, the contact stress decreases due to the increased contact area. The diameter of the rollers is approximately 21.9 cm (8.63 in) depending on the number of times the roller has been ground.

3.1.2 General Maintenance

A manual published by Polymet for a RC Rig machine that they manufacture offers maintenance suggestions (47). Additionally, Dave Lawrentz of Timken wrote a manual specifically for the TRFM (5). The following is a table of regular maintenance based on experience at CSM, Table VII.

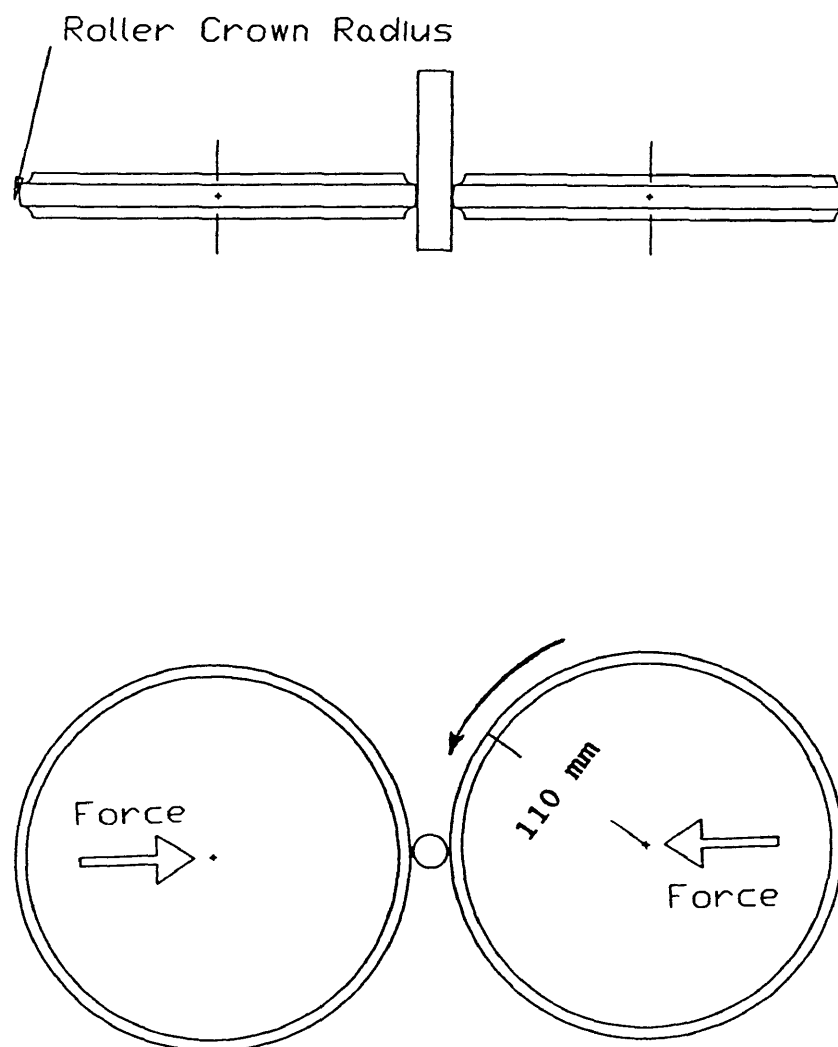


Figure 29: A drawing of a specimen and the toroid rollers of the Timken Rolling Fatigue Machine. Direction of rolling is indicated by the curved arrow.

Table VII: General Maintenance of TRFM Fatigue Machines

Action	Frequency
Grind Surface of Rollers	As needed per ref (5)
Lubricate Generator and Motors	Every 3 months of continuous service
Replace Bearings in Main Pillow Block	Every 5 billion cycles
Grease Bearings in Rollers	Once every 10 billion cycles
Change Oil	When oil turns dark and thick. Consult Timken Concerning Replacement Oil
Clean Brushes on Generator	Remove covers and check brushes for carbon. Clean out the carbon dust. Accumulation of carbon dust can lead to spalling of the main spindle (5).

3.2 Experimental Procedures

The following experimental procedures outline the specimen preparation and metallographic techniques utilized to characterize the stressed volume of the wear tracks of both the Timken and Caterpillar specimens. To obtain profiles of various parameters, measurements were made on some samples with depth as well as at the surface.

3.2.1 Specimen Preparation, Machining

The first set of samples, the TRXX specimens, were prepared by Timken. The second set, CDXX and CDRXX, was machined at CSM and finished at Caterpillar. Steel was

received at CSM in the form of bars of 2.87 cm (1.13 in.) in diameter and 1.8 m (6 ft) long. The bars were cut into 30.4 cm (12 in) long bars and machined to 1.94 cm (0.765 in) in diameter at CSM before being sent to Caterpillar. At Caterpillar, the specimens were cut in half, producing 12 specimens. Centers were put in the new ends and the specimens carburized. After carburizing, specimens were centerless ground to a root mean surface height, R_q , of 0.322 μm , and a root mean square profile slope, DELQ, of 0.066 radians, Table VIII. Table VIII shows the surface roughness parameters for both the Caterpillar specimens and the fatigue machine rollers.

Table VIII: Surface Roughness Measurements

	R_q (μm)	DELQ (rad)
Caterpillar Specimens	0.322	0.066
Fatigue Machine Rollers	0.200	0.035

3.2.2 Carburizing and Reheat Treatment

The specifics of the carburizing and reheat treatment used on the Timken specimens are not known, except that the final surface hardness was approximately 60 R_c and the case depth is 2 mm (R_c 50).

The Caterpillar specimens were carburized in integral furnaces, i.e. the steel was not exposed to air between the various processes. The CDXX specimens were gas carburized

at 927 °C (1700 °F), oil quenched, and tempered at 150 °C (302 °F) for one hour. The CRXX specimens were gas carburized at 927 °C, cooled in a nitrogen atmosphere, reheated for 1.6 hours at 843 °C (1550 °F), oil quenched, and tempered at 150 °C for one hour. Case depths for all specimens are 2 mm (R_c 50). Carbon profiles of unrun CDXX and CRXX specimens are shown in Figures 30 and 31 respectively. Six CDXX bars were carburized and six CRXX bars were carburized, a total of twelve.

3.2.3 Residual Stress Measurements

According to Bragg's law,

$$\lambda = 2d \sin(\theta)$$

the d spacing of atomic planes can be measured by X-ray diffraction. From the change in d spacing, the change in residual stress and lattice parameters are calculated with Young's modulus and Poisson's ratio respectively.

Residual stress measurements were taken on the Caterpillar specimens by Bob Bemis of Caterpillar. X-ray diffraction was performed in the axial and circumferential directions on untested areas and on the stressed volumes of the wear tracks. Measurements at depth were obtained by first electropolishing material from the surface. Residual stress profiles were done on CD01, CD33, CR01, and CR33. Table IX gives the parameters used for measuring the change

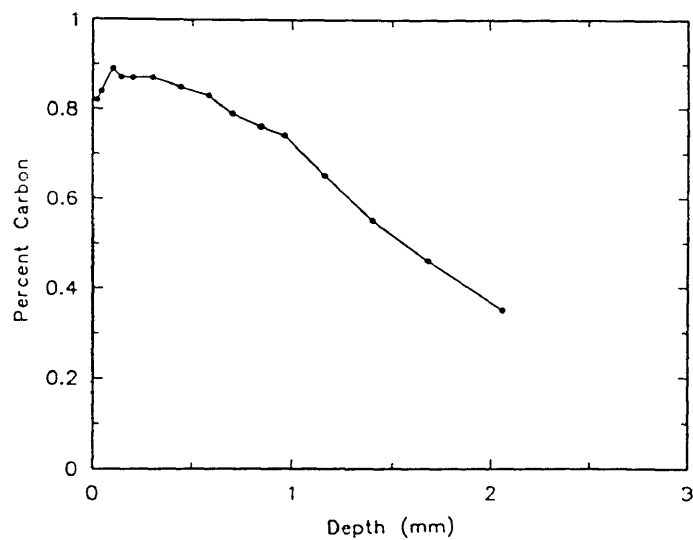


Figure 30: Carbon profile of CD01, untested direct quench specimen, courtesy of Caterpillar Inc.

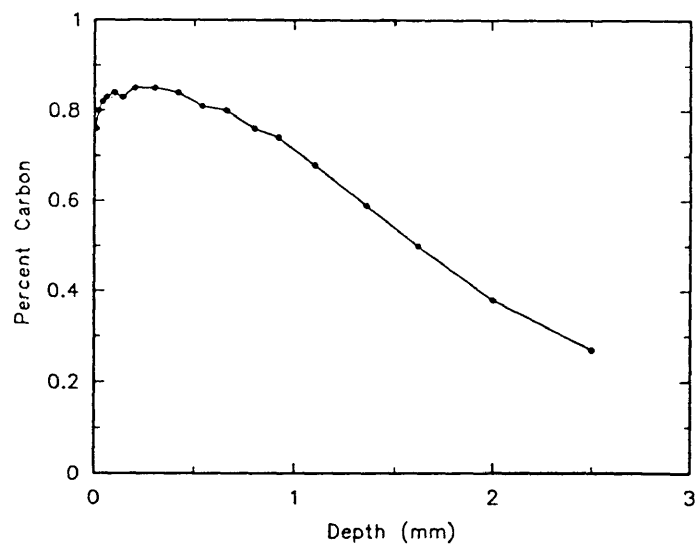


Figure 31: Carbon profile of CR01, untested reheated specimen, courtesy of Caterpillar Inc.

in residual stresses in the Caterpillar specimens. Since the residual stresses seemed rather high, two bars on which residual stresses were measured at Caterpillar were sent to Timken and residual stress measured there for a comparison. The numbers were very similar.

Table IX: Residual Stress Measurement Parameters

Parameter	
X-ray Wavelength	2.28962 angstroms (chrome target)
X-ray Power	54 W (tube filament 45.0 kV, 1.20 mA)
X-ray Beam Collimator Geometry	0.1 inch diameter pinhole
Calibration Reference Specimen	60-62 ksi (shot-peened steel plate)
Young's Modulus for Steel	33,660 ksi
Poisson's Ratio	0.25
Analysis Method	Two exposures
Psi Inclination Angles	0° (first peak) 45° (second peak)
X-ray Exposure Time	60 to 120 sec/peak

3.2.4 Profilometer Traces

Plastic deformation can reduce the contact stress as much as 10 percent by increasing the contact area. Wear also increases the contact area. Therefore, the calculated Hertzian stresses may only be approximate, Figure 32 (15,48,49). Figure 32 schematically illustrates the change

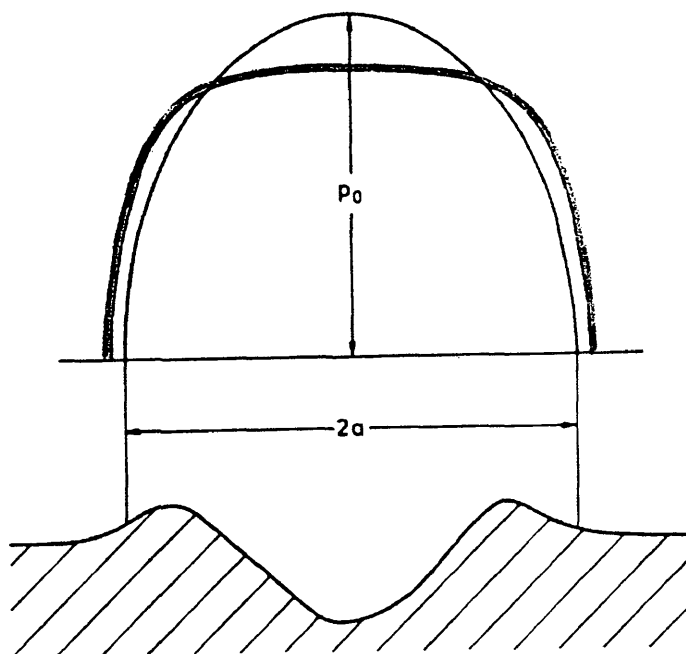


Figure 32: Changes in the Hertzian pressure distribution as a result of plastic deformation. The thin line is the original distribution and the thick line is the resulting distribution due to plastic deformation (49).

in pressure distribution when plastic deformation of the surface occurs. The solid line is the initial distribution as calculated by Hertzian equations and the dashed line is the resulting distribution. Hence, it is important to take profilometer traces of the wear tracks to determine the degree of plastic deformation. Profilometer traces of the Caterpillar specimens were done at Caterpillar with a Taylor-Hobson profilometer. The lower frequency limit for the machine was $0.0020 \mu\text{m}^{-1}$ and the upper frequency limit was $0.4000 \mu\text{m}^{-1}$.

3.2.5 Sectioning of Samples

After the residual stress and profilometer measurements were completed and the bars returned to CSM, they were sectioned into the pieces illustrated in Figure 33. The first cuts around a wear track resulted in a cylindrical section, 25 mm (1 in) long, with the wear track in the middle. This piece was cut in half along the longitudinal axis. One of the halves was given to Dr. Williamson of the Physics Department at CSM for Mössbauer spectroscopy. The other half was cut in half along the longitudinal axis, leaving a section labelled an A section (axial section) and a section which was the mirror image of A. This "mirror image" of A was cut in half transverse to the longitudinal axis through the wear track resulting in

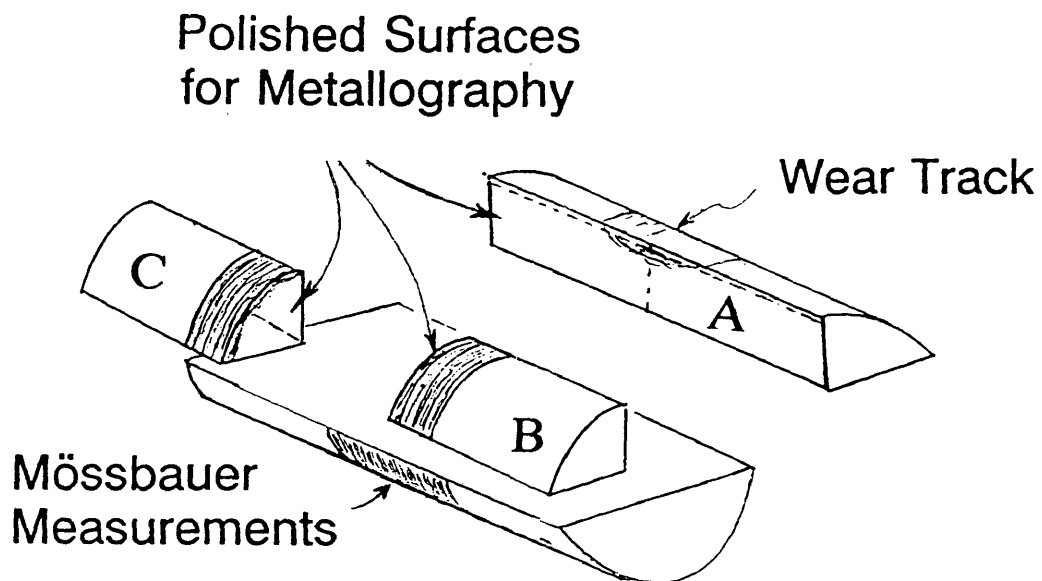


Figure 33: Sectioning of Caterpillar rolling contact fatigue samples. The "A" section stands for axial section and "C" for circumferential. The bottom piece was separated from the others for Mössbauer spectroscopy.

the B and C sections shown. It was cut slightly off center so that the "C" section (circumferential section) could be polished to the center of the wear track. To determine when the specimen was polished was to the center, a notch was cut to a measured distance in one side of the sample so that the mounting material would fill it in. When the notch was polished away, then the polishing was stopped. The last two section designations are B for the opposite side of the wear track from the C section and D for cylindrical sections.

At first, sectioning was done with a Buehler Isomet 11-1180 low speed diamond saw. The cuts were high quality. However, some of the sections took several days to cut. The gears in the saw are made of plastic and frequently wore out. Therefore, one of the specimen holders for the Buehler Isomet was modified to fit in the vice of a Buehler Model 10-1000 Abrasive Cutoff Saws. As long as adequate coolant was provided, the abrasive cutter cut through the material in a couple of minutes without burning the steel.

3.2.6 Sample Identification

After sectioning, sections for Mossbauer spectroscopy were identified by cutting notches in the ends. Figure 34a is an illustration of a sample labelled number 72. The A, B, and C sections were mounted for metallography and

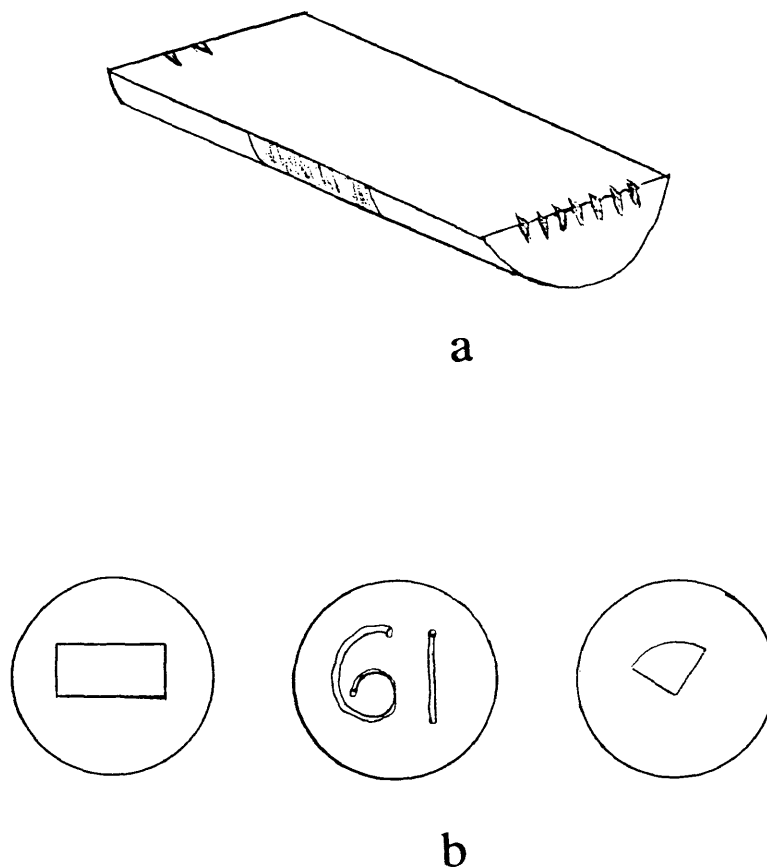


Figure 34: Illustration of labelling method for sections of Caterpillar specimens a) the number 72, 7 marks on one end and 2 on the other denotes a section for Mössbauer spectroscopy from bar number 7 wear track number 2 b) A and C sections mounted in hot-mount material, back of one of the sections showing wire numerals embedded in the mounting material to label these sections.

identified by wire numbers in the backs of the mounts. Figure 34b is an illustration of A and C section mounts and the back of a mount with the number 61 formed out of short pieces of wire. The identification scheme for the Mossbauer specimens is as shown in Table X. In general, the first number identifies the original bar that the section is from and the second number identifies the wear track on that bar. A number 72 means bar number 7 wear track number 2. A, B, and C sections were identified using the same scheme. A and C sections were mounted in red, hot-mount material and the B sections were mounted in black.

Table X: Identification Scheme for RCF Specimens

Number of Notches on One End	Number of Notches on the Other End	Designation	Number of RCF Cycles
6	0	CD01	0
7	0	CD01	0
6	3	CD11	10
6	2	CD12	100
6	1	CD13	1,000
7	1	CD21	10,000
7	3	CD22	100,000
8	2	CD23	1,000,000
7	2	CD31	10,000,000
8	1	CD32	100,000,000
8	3	CD33	500,000,000
1	1	CR01	0
4	2	CR01	0
3	0	CR11	10
4	0	CR12	100
0	0	CR13	1,000

continued

Table X (continued)

Number of Notches on One End	Number of Notches on the Other End	Designation	Number of RCF Cycles
4	1	CR21	10,000
4	3	CR22	100,000
5	2	CR23	1,000,000
2	2	CR31	10,000,000
5	1	CR32	100,000,000
5	3	CR33	500,000,000
9	1	CR41	1,400,000,000
8	0	etched CD01 0.51 mm (0.020 in)	0
8	4	etched CD33 0.51 mm	1,400,000,000
5	0	etched CR01 0.51 mm (0.020 in)	0
5	4	etched CR33 0.51 mm	1,400,000,000

3.2.7 Mössbauer Spectroscopy

Conventional Mössbauer spectroscopy involves resonant absorption of gamma rays by ^{57}Fe nuclei in suitably thin specimens, typically foils about 25-50 μm thick. This method is well documented for characterization of the many

phases present in all types of steel, particularly for retained austenite and various carbides (50,51,52). Here, two types of nonconventional backscatter Mössbauer spectroscopy were tested to analyze the microstructures of as-received AISI 8620 and RCF-worn carburized 8620 specimens: the conversion electron Mössbauer spectroscopy (CEMS) method probes to a depth of about $0.1\text{ }\mu\text{m}$ below the surface, and the conversion x-ray Mössbauer spectroscopy (CXMS) method to about $10\text{ }\mu\text{m}$ (53).

Typical CEMS and CXMS data are shown in Figures 35 and 36 together with the computer deconvolution of the spectra into various Fe sites in the steel constituents. Relative emission versus velocity is plotted for uncarburized, TR01, and TR32 specimens. The middle peak of the spectra is retained austenite. Each site yields a particular subspectrum as indicated by the stick diagrams shown at the bottom of the figure. The subspectra are also indicated by the dashed curves in each spectrum. The solid curve passing through the data points of each spectrum is the sum of all the subspectra used to fit that spectrum. The lineshape of each resonance "line" is well known to be Lorentzian. At the top of Figure 35 an uncarburized specimen shows a superposition of two six line magnetic components, $M(0)$ and $M(1)$, typical of Fe atoms in ferrite

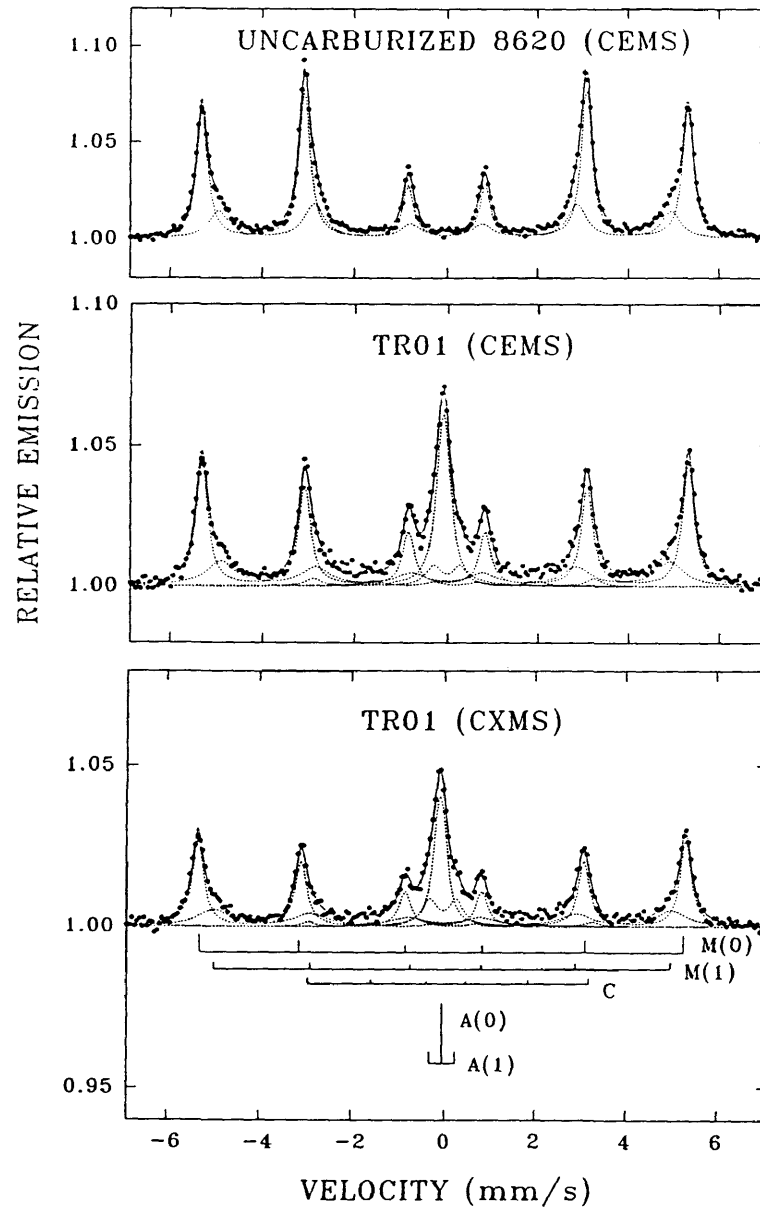


Figure 35: Mössbauer spectra for an uncarburized sample and an untested Timken reheat sample, TR01. The middle peak of the spectra is retained austenite. Thus the uncarburized section has zero retained austenite as measured by Mössbauer spectroscopy. CEMS and CXMS are two different methods of Mössbauer spectroscopy.

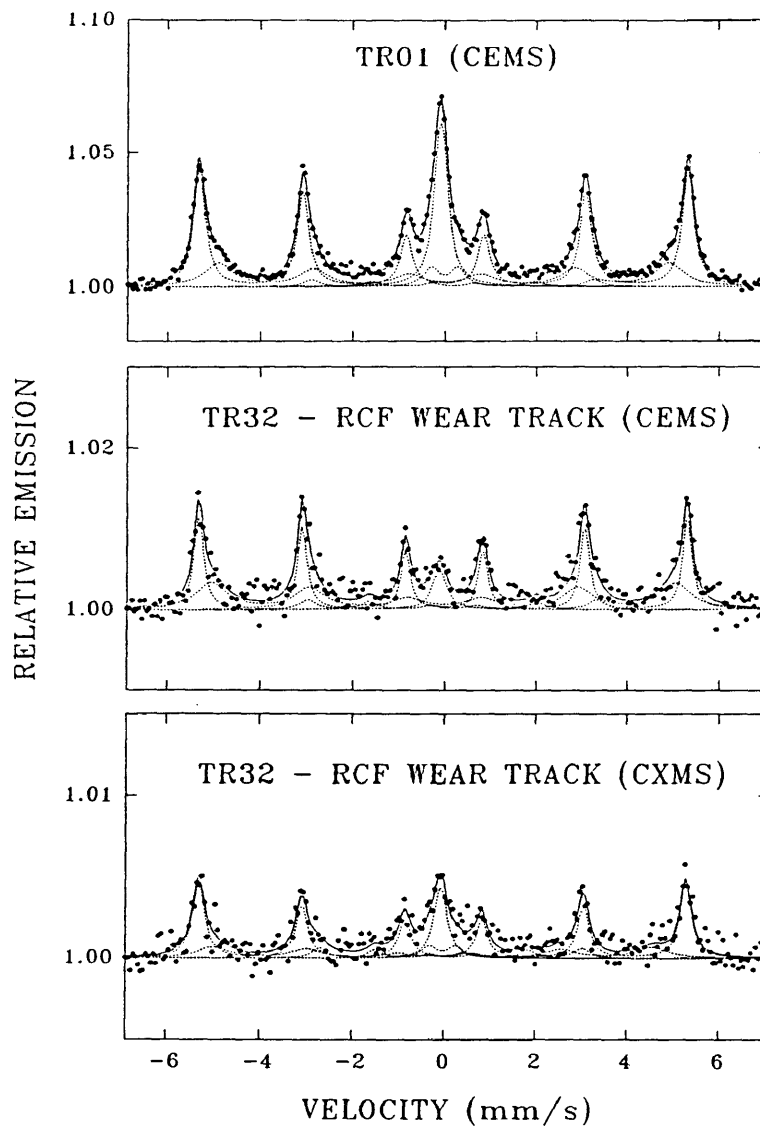


Figure 36: Mössbauer spectra for TR01 versus TR32. The middle peak of the spectra is retained austenite. Thus TR32 has less retained austenite after 2.8×10^8 cycles than the untested specimen, TR01. CEMS and CXMS are two different methods of Mössbauer spectroscopy.

or martensite with 0 and 1 nearest neighbor alloy atoms (e.g. Mn, Si, Cr), respectively. The lower two spectra of Figure 35 are from TR01 and they have substantial fractions of nonmagnetic retained austenite as indicated by A(0) and A(1) components which are due to Fe atoms in austenite with 0 and 1 nearest neighbor carbon atoms (in the interstitial octahedral sites), respectively. In addition a weak third phase labelled "phase C" was needed to obtain a good fit to these spectra and its parameters are typical of a cementite-like carbide. Neither austenite or cementite were found in the uncarburized 8620. Figure 36 compares the spectrum from the unworn TR01 specimen to those from TR32 (280 million cycles). To acquire CEMS data from the wear track, a simple masking of a 2.7 mm wide area (the visible width of the TR32 wear track) around the circumference of the cylindrical specimen with masking tape was sufficient to block the conversion electrons emerging from the unworn steel surface. To acquire CXMS data from the wear track, adhesive lead (Pb) tape was needed to prevent conversion x-rays from escaping from the unworn area into the detector. The Pb tape was found to be unsuitable for CEMS because a large background of photoelectrons are generated when the gamma rays and x-rays from the Mossbauer source strike the Pb. The statistical

qualities of the spectra from the wear track are clearly not as good due to the small area but they are still adequate to observe substantial changes in austenite and carbide phases. The integrated intensities of the resonance lines are directly related to the fraction of Fe atoms in various phases.

CEMS and CXMS were also performed on TR41 and on the Caterpillar specimens, and at various depths as well. CEMS (0.1 μm) was used on unetched surfaces and CXMS (10 μm) on etched surfaces. Figure 37 illustrates a statistical quality indicator with which the raw data was analyzed. A "good" rating implies less scatter in the spectrum.

3.2.8 Electropolishing, Macroetching

Electropolishing was used to remove up to 508 μm (0.020 in) from the surfaces of TR01, TR32, TR41, CD01, CD33, CR01, and CR33 for Mössbauer spectroscopy. Figure 38 shows the electropolishing experimental setup. The electrolyte used is a combination of hydrochloric acid (HCl), distilled water, and ethyl alcohol in sufficient proportions to produce a solution with a 40 V potential when 5 amps of current are passed through the system (54,55,56). Additions of hydrochloric acid increase conductivity and ease of removal of the anodic layer while additions of distilled water and/or ethanol decrease the

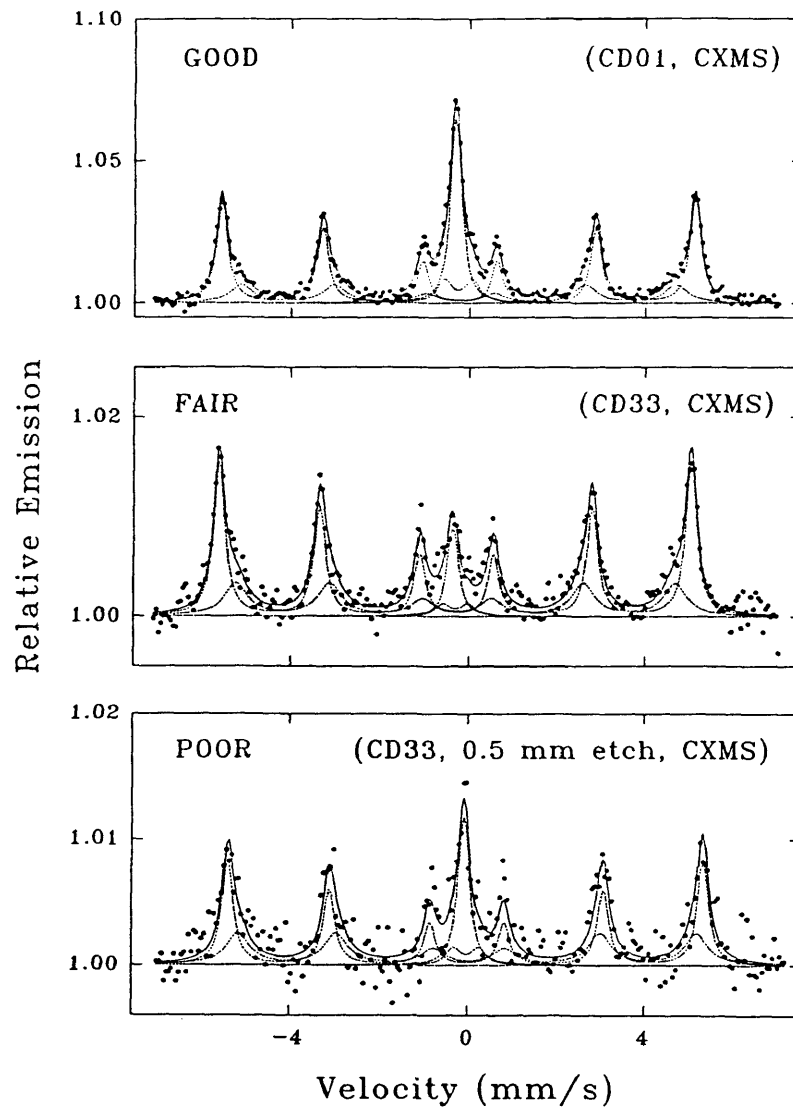


Figure 37: A statistical quality indicator used with the Mössbauer results. A "good" rating implies less scatter in the spectrum.

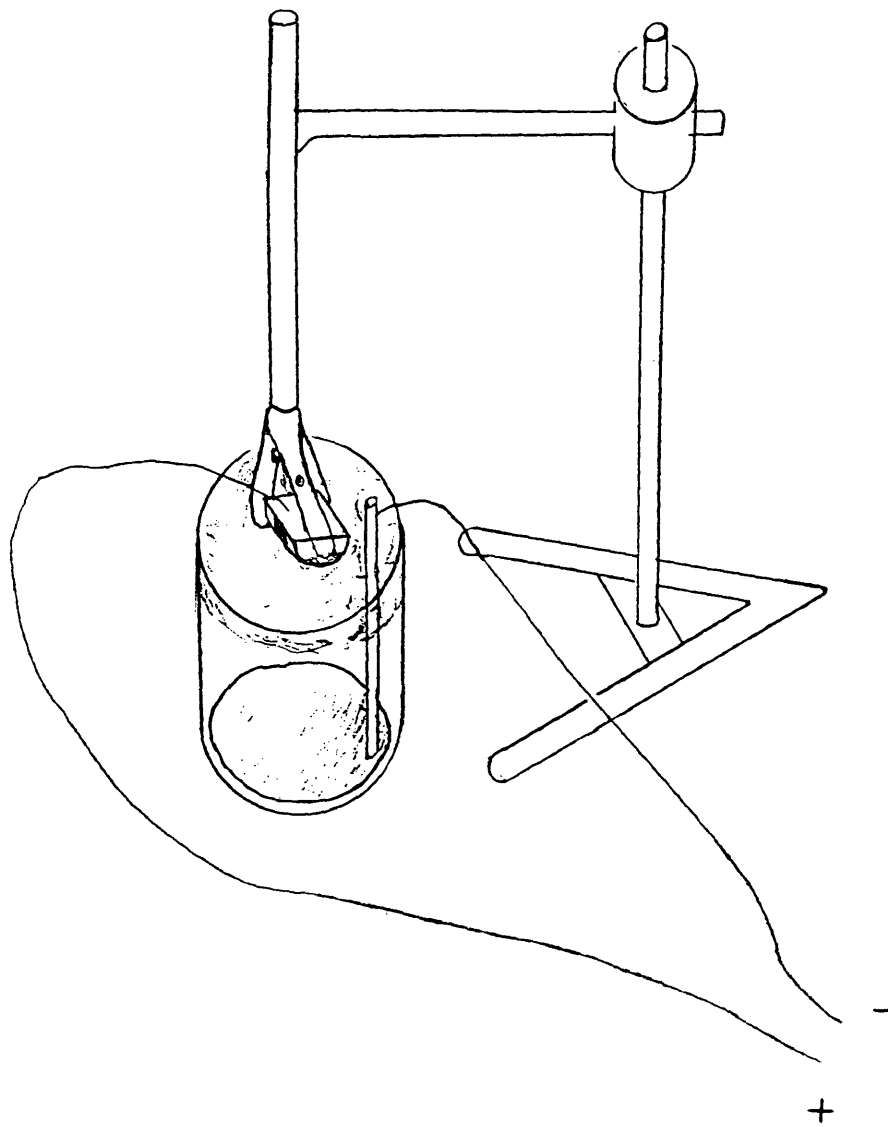


Figure 38: Electropolishing experimental setup: specimen holder, specimen, electrolyte, cathode and electrical leads.

conductivity. The etch is relatively uniform. Figure 39 shows two profilometer traces, one of the wear track of TR41 before electropolishing and one after removing 130 μm from the surface. The electropolishing preferentially attacks austenite, therefore Mössbauer spectroscopy at depth was done with CXMS which probes deeper into the material. The etching is done in 10 second intervals. After 10 seconds, the specimen is removed and the anodic layer wiped off. Each 10 second pass removes approximately 3 μm (0.0001 in) of material. Voltage can vary depending on how the surface finish looks, but usually at least 5 amps of current is required. The material electropolishes differently as a function of depth, probably due to the carbon profile. Electropolishing with this electrolyte should be done in a ventilated hood as it produces chlorine gas.

Other electrolytes and macroetches were tried. A 50/50 mixture of phosphoric and sulfuric acids produces a smooth finish, but the anodic layer is hard to remove. Apple's grain boundary, chemical etch (57) did not work for this application. K. Erven (58) reported that it produced a good surface finish at short times and shallow depths and a poor surface finish for deeper etching. Various additions to the original hydrochloric electrolyte (56)

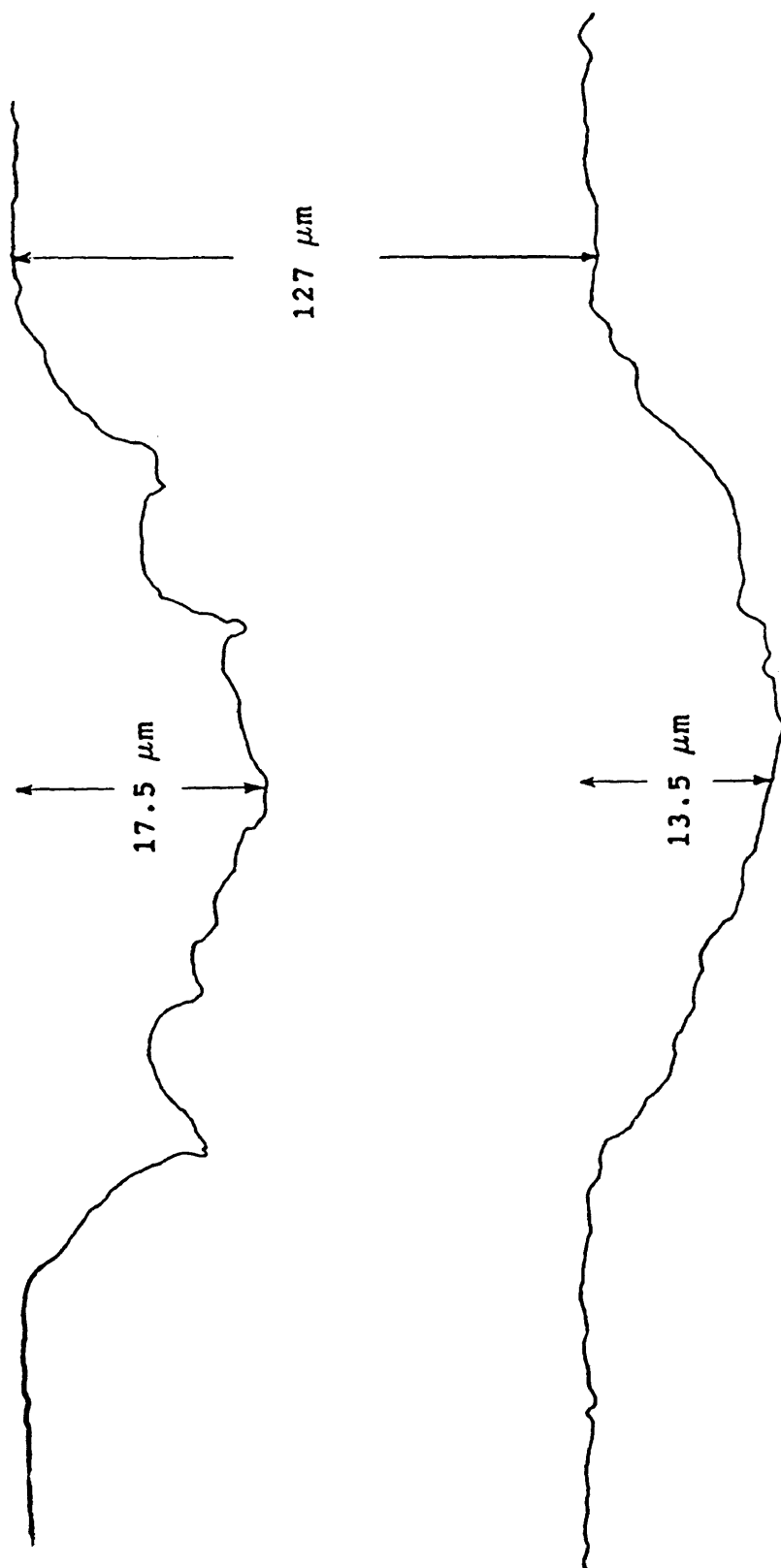


Figure 39: Two profilometer traces of Timken specimen number TR41. One of the wear track of TR41 before electropolishing and one after removing 130 μm from the surface. These profilometer traces were done by D. Williamson.

were tried. However, it was determined that the small improvements in surface finish were not worth the necessary precautions (54,55,56). The additions reacted with each other producing potentially hazardous products.

3.2.9 Etchants for Microscopy

Metallographic surfaces were etched in 2% nital (98% CH_3OH , 2% HNO_3) for 15 seconds, rinsed, and then etched in sodium metabisulfite ($\text{Na}_2\text{S}_2\text{O}_5$) for 20 seconds to increase the contrast between martensite and retained austenite.

3.2.10 Light Microscopy and Image Analysis

A Leco Neophot 21 Metallograph and Leco 2001 Image Analyzer were utilized to study the macroetching effects produced by RCF. Light microscopy was done at 50X and 1000X at various locations. Image analysis profiles were produced by setting the field of view to 200 μm (400X) and analyzing the metallographic sections from the RCF surface towards the core 200 μm at a time.

3.2.11 Microhardness Measurements

A Leco M-400A Microhardness Tester was used to measure microhardness profiles and traverses. Profiles were taken from the RCF surface towards the core. Traverses were done on A sections of the Caterpillar specimens at 0.24 mm from the RCF surface, see schematic traverse in Figure 33.

Hardness indentations were made 0.1 mm apart with a diamond

pyramid indenter, weighted with a 300 g load. The timer was set at 15 seconds. A typical profile or traverse required 60 hardness indentations. Raw data from the hardness tester is a set of measurements of the vertical and horizontal length of each indentation. These two measurements are averaged and the result is converted by use of a chart, see Appendix, to the Vickers hardness scale. The profiles and traverses were first plotted in terms of Vickers hardness versus distance. This showed a significant amount of scatter in the data. So next, the data was plotted in terms of the average of the vertical and horizontal measurements of the indentation and then the scale changed to read R_c . These curves are smoother and better reflect the actual hardness transition in the material. Table XI lists the profiles and traverses made. The first four digits of the code tell which wear track it is. The fifth digit tells the type of section it is and the last digit tells whether it is a profile or traverse. For example, CD33AP is a profile on an A section of wear track CD33. Two separate measurements were made for CD01 and CR01 and averaged to produce a more accurate initial profile.

Table XI: Profiles and Traverses Made on RCF Sections

Designation	Section (A,B,C,D)	Profile (P) and/or Traverse (T)
TR01	D	P
TR32	C	P
TR41	C	P
CD01	Two A sections and two C sections	AP,AT,CP
CD32	A,C	AP,AT,CP
CD33	A,C	AP,AT,CP
CR01	Two A sections and two C sections	AP,AT,CP
CR32	A,C	AP,AT,CP
CR33	A,C	AP,AT,CP
CR41	A,C	AP,AT,CP

3.3 Analytical Procedures

The following analytical procedures were utilized to calculate and analyze the stress states in the material. Various stresses were calculated for both the Caterpillar and Timken Specimens. Regions of highest τ_{xz} were calculated for the Timken specimens and compared with the white etching bands observed in TR41.

3.3.1 Ruffian - Timken Stress Analysis Software

Ruffian is a program provided by Timken that calculates the magnitude and depth of maximum orthogonal

shear stress, as well as contact area and several other parameters. It takes into account lubrication and surface roughness. This program was used to verify the MathCAD numbers. Table XII lists the input parameters for Ruffian calculations of stresses for the Caterpillar specimens.

Table XII: Input Parameters for Ruffian Program

Parameter	
Root mean square surface height of body 1, RQ1	0.32211 μm
Root mean square surface height of body 2, RQ2	0.20000 μm
Root mean square profile slope of body 1, DELQ1	0.06632 radians
Root mean square profile slope of body 2, DELQ2	0.03490 radians
Lower frequency limit	0.00200 μm^{-1}
Upper frequency limit	0.40000 μm^{-1}
Tensile yield strength	386.1061 MPa
Radius of curvature of body 1 - rolling direction	9.525 mm
Radius of curvature of body 1 - transverse direction	50000 mm
Radius of curvature of body 2 - rolling direction	109.500 mm
Radius of curvature of body 3 - transverse direction	76.200 mm (3 in) 25.400 mm (1 in)
Contact Load (variable)	N
Lubricant dynamic viscosity	3.00 centipoise
Lubricant pressure viscosity index	0.014500 mm^2/N
Rolling velocity	8.8774 m/sec

3.3.2 MathCAD and Ansys, Hertzian Stress Calculations

MathCAD acts as a piece of paper on which mathematical equations are typed and the answer is automatically calculated. Hertzian stress equations were typed into several pages of a MathCAD file. This program calculates the principal stresses, τ_{45} , σ_e , τ_{oct} , τ_{yz} , and τ_{xz} . Lubrication conditions and surface roughness are not taken into account.

τ_{xz} stress for the Timken specimens at 0.1 mm intervals in a 1.2 mm by 1.2 mm by 1.2 mm box about the contact zone was calculated with this program and transferred to a spreadsheet, Lotus 123. The 7500 data points that resulted were arranged into sections through the material (45). The Lotus files were imported into a graphics program, Coplot. In Coplot, contour plots of the shear stresses were calculated using mostly default settings. These plots were overlayed onto light micrographs of the DER of TR41 (45) and are discussed later.

Ansys is a finite element package. Taking advantage of symmetry, a pie shaped mesh on the xz plane was encoded in Ansys and the stresses calculated. Figure 40 shows the imposed stresses on the negative x side of the xz plane in the Caterpillar specimens during RCF. The values in this

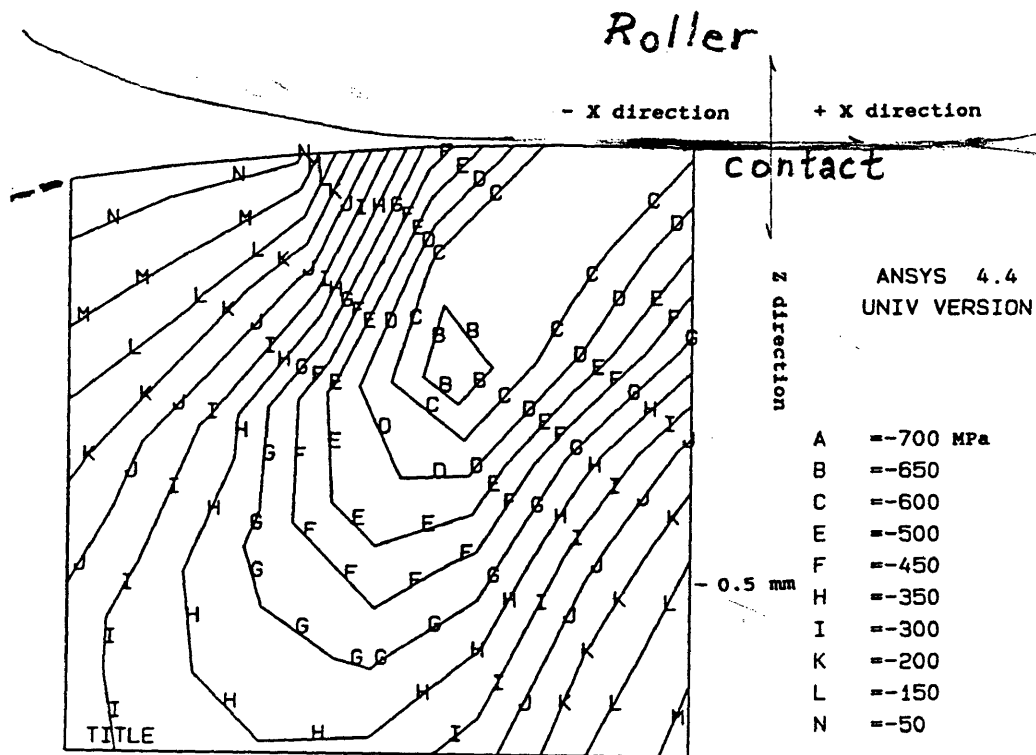


Figure 40: Imposed τ_{xz} shear stresses on the negative x side of the xz plane in the Caterpillar specimens during rolling contact fatigue.

figure are negative as shown. Calculations of τ_{xz} on the negative side of the x axis result in negative values and calculations on the positive side of the x-axis result in positive values. After the Ansys input files are setup, Ansys is quicker than the MathCAD approach.

4.0 EXPERIMENTAL RESULTS

Figure 41 and Figure 42 are schematic overviews of this work. Figure 41 shows a representative stress cube at different stages in RCF. Figure 42 shows A and C sections of Timken and Caterpillar specimens tested to various number of cycles. Caterpillar specimens at decade intervals from 0 to 10^6 cycles are left out of these figures for sake of space. AISI 8620 was carburized, heat treated, and then rolled in Timken Rolling Fatigue Machines. The rate of microstructural change was greater in the Timken specimens than in the Caterpillar specimens. A Timken specimen tested to 10^9 cycles showed white etching bands.

Swahn et. al. have presented a schematic framework for the development of changes due to RCF. This framework was presented earlier as Figure 17 and is reproduced here as Figure 43 with some modifications to incorporate the results shown in Figures 41 and 42. The diagram of Swahn et. al. has been modified by introducing Roman Numerals for the various stages, by denoting the transition region between Stages I and II as the beginning of the transformation of austenite to martensite, by adding a

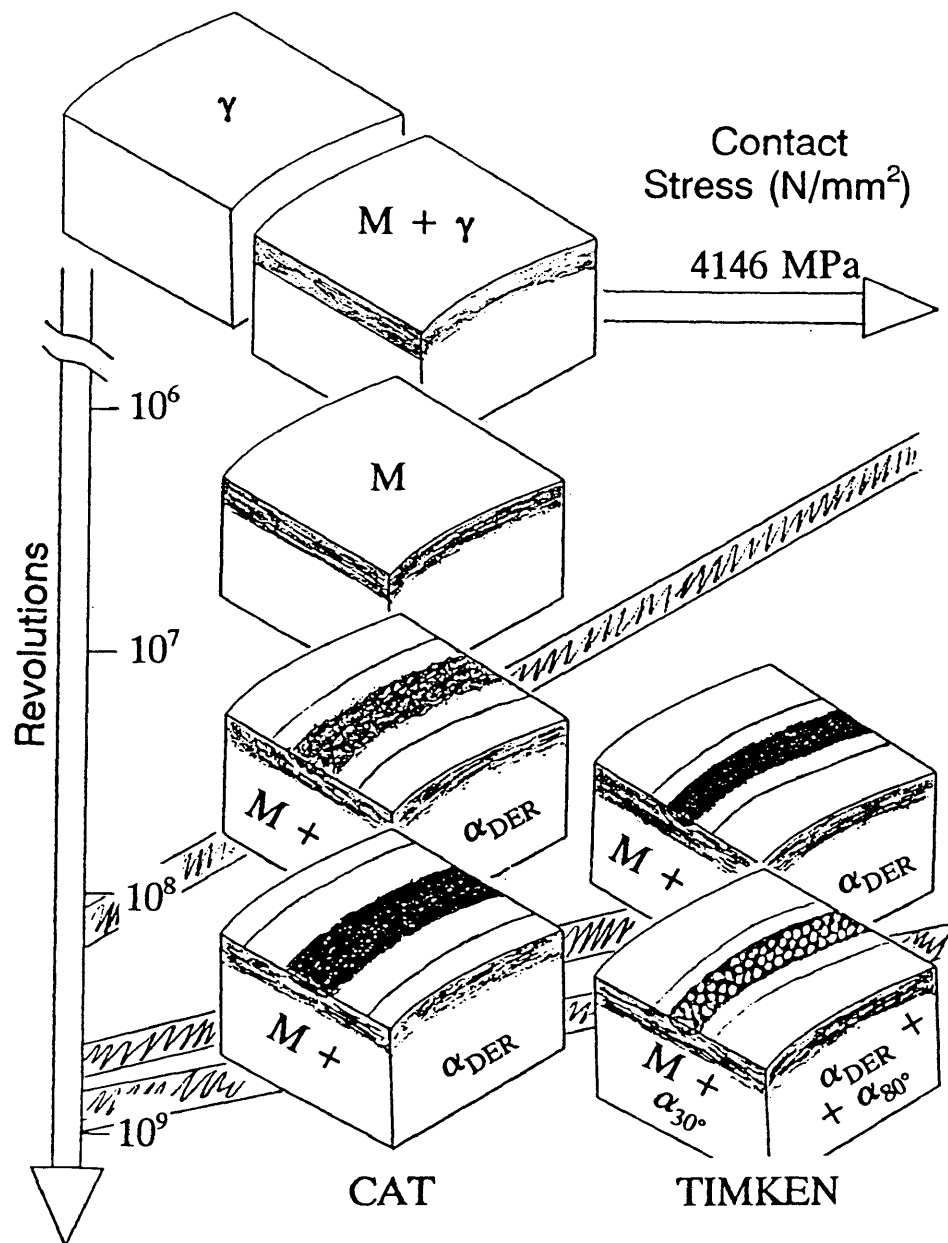


Figure 41: Overview of this work using a schematic representative stress cube to track microstructural change during rolling contact fatigue.

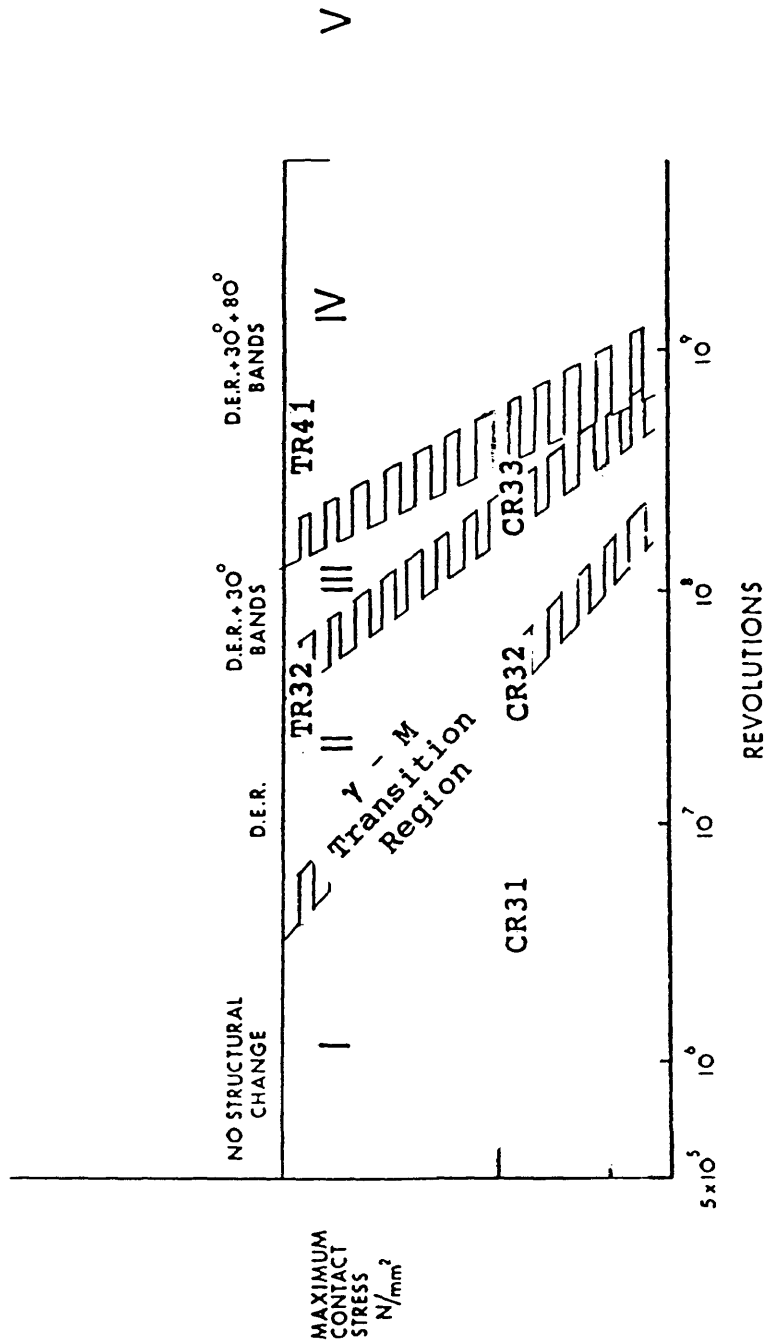


Figure 43: Modified Swahn et. al. diagram which illustrates the experimental conditions of this investigation.

fifth stage, and by changing the horizontal axis to match this work.

Various stages of structural change produced by RCF are shown as a function of cyclical contact stress at number of revolutions. The sequence of stages is as follows:

- I No Structural Changes
- * Transition Region Between Stages I and II
- II Dark Etching Region (DER)
- III Formation of 30 degree white etching bands
- IV Formation of 80 degree bands crossing the 30 degree bands in the DER
- V Cracking, leading to pitting and spalling

The two stress levels and the various specimens examined are shown schematically in Figure 43. The reason for the differences in behavior of the two groups of specimens was that the width of the wear track was increased for the Caterpillar specimens in order to facilitate Mössbauer spectroscopy, X-ray diffraction, and metallographic measurements. The increased width of the wear track served to reduce the contact stress and significantly reduced the rate at which structural changes developed. The results obtained from testing the two groups of specimens are presented in the following sections. Figure 44 is a similar diagram by Zwirlein and

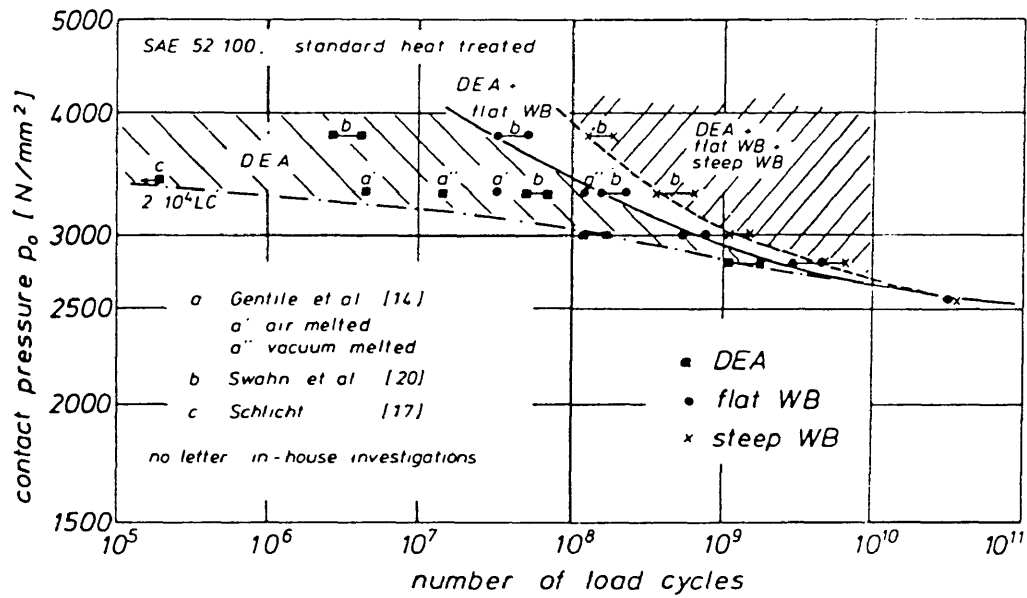


Figure 44: Diagram by Zwirlein and Schlicht after Swahn et. al. showing that the width of Stage III diminishes towards zero as the contact stress decreases (28).

Schlicht showing that the width of Stage III diminishes towards zero as the contact stress decreases. The following assumptions are made with respect to Figures 43 and 44:

1. The stresses in the material are sufficiently high, causing structural changes to occur, as revealed by etching effects.
2. The areas of highest shear stress concentration can initially be estimated with Hertzian equations for elastic contact of homogeneous, isotropic materials.
3. Plastic flow occurs only or predominantly in the areas of highest shear stress concentration and cracking initiates subsurface.
4. Inclusion particles, especially in clean steels such as the one studied here, are not responsible for failure.
5. Case temperatures above ambient are typical of rolling contact fatigue.

4.1 As-received and Untested Microstructures

Figure 45 consists of four micrographs. Figure 45a is of the as-received, uncarburized microstructure. Figure 45b shows part of the case of TR01. Figure 45c shows part of the case of CD01, a carburized and direct quenched Caterpillar specimen. Figure 45d shows part of the case of CR01, a carburized and reheated specimen. The CD01, CR01, and TR01 samples are very similar. However Figure 45b shows more spheroidized carbides suggesting that TR01 was

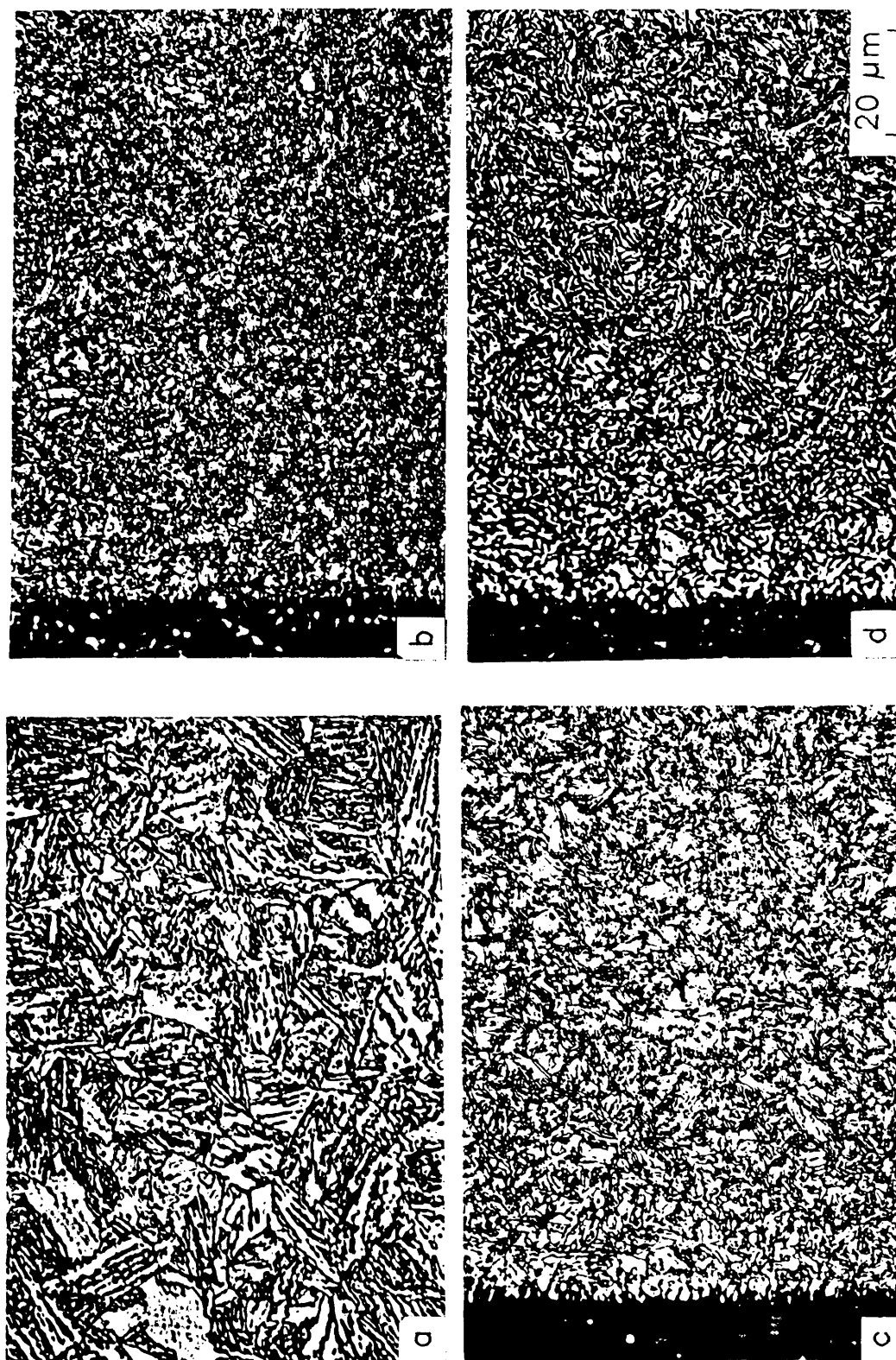


Figure 45: Four micrographs of the as-received and as-carburized material, a) as-received AISI 8620, b) TR01 Timken as-carburized c) CD01 d) CR01, all 2% nital etch for 15 seconds, light microscopy, 800X.

reheated at a lower temperature than the CR01 specimens (1). Most of the results from Caterpillar specimens are data for the reheat specimens. The results from the CDXX and CRXX specimens were very similar and therefore more metallography was done on the CRXX specimens than on the CDXX specimens so that the results from the two reheat conditions TRXX and CRXX could be compared.

4.2 Basis for Evaluation of Results

There are three planes from which to observe the microstructural changes due to RCF, Table XIII. The planes as listed in Table XIII are: the xy plane, the xz plane, and the yz plane. In order to match the planes on which results were observed with changes in the steel, a "representative volume of carburized case" is defined and the results are related to it, Figure 46. Figure 46 is a schematic of the representative volume described by Table XIII.

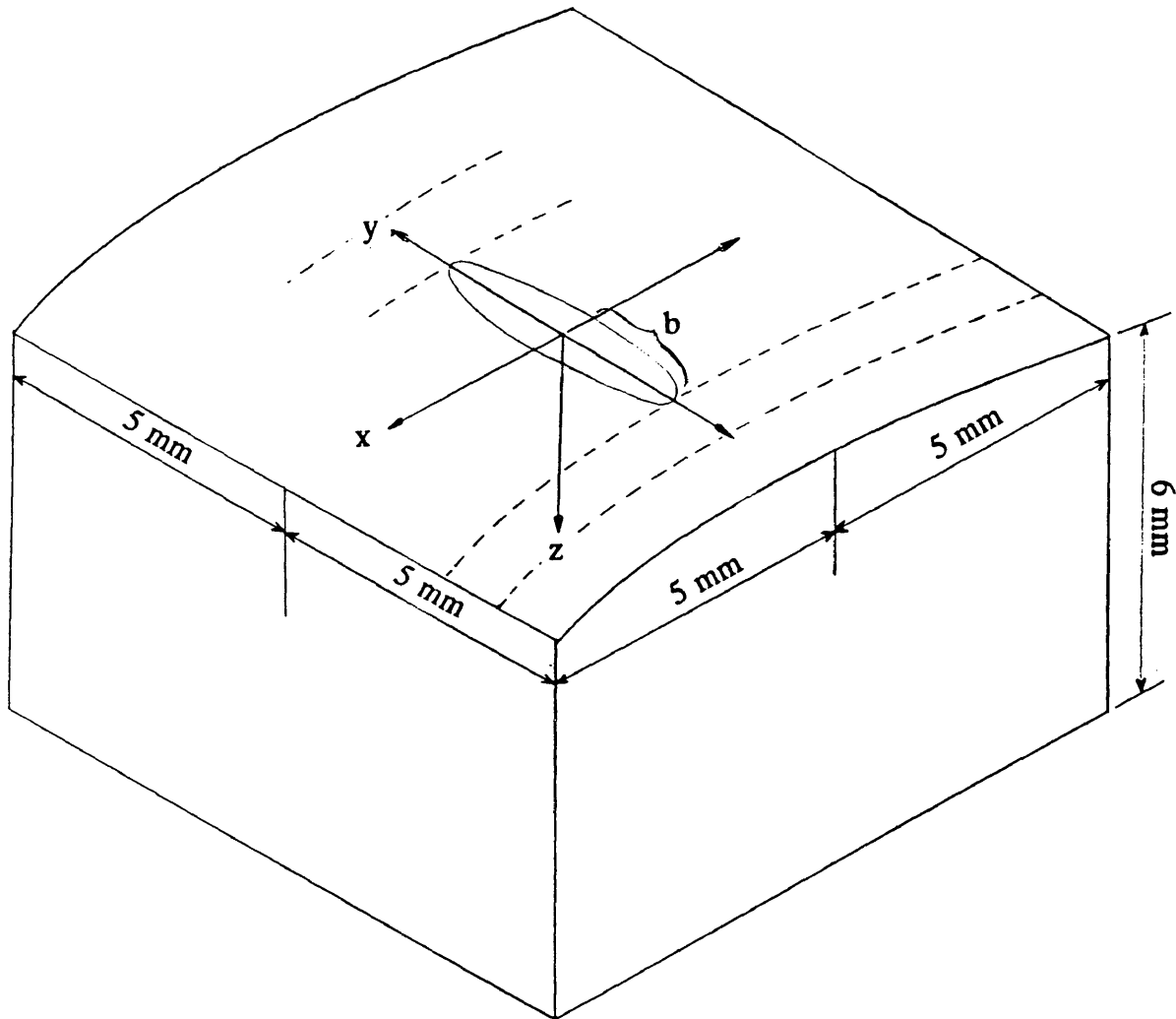


Figure 46: Schematic of the representative volume used in this work to place microstructural changes on various planes as a function of cycles.

Table XIII: Faces and Dimensions of Representative Volume

Description	Faces	Dimensions
Tangent Section	xy	$x \pm 5 \text{ mm}$ $y \pm 5 \text{ mm}$
Circumferential (Parallel) Section	xz	$x \pm 5 \text{ mm}$ $z \pm 6 \text{ mm}$
Transverse (Axial) Section	yz	$y \pm 5 \text{ mm}$ $z \pm 5 \text{ mm}$

Referring to Figure 46, the contact area between the rollers of the fatigue machine and the specimen is an ellipse due to the contact geometry and is assumed to be flat (19). Wear causes the contact width to expand as shown by the dashed lines. Per convention, a right-handed coordinate system is shown. The rolling direction is in the positive x direction, the y direction is transverse to the rolling direction, and the positive z direction is normal to the specimen surface. The direction of rotation for a point on the surface of the rolling elements is in the negative x direction.

The microstructural changes of Figures 43 and 44 were sorted into four data categories as tabulated in Table XIV. These categories are: changes in depth profiles, overall macroscopic changes, change in the dark etching region, and changes at the surface. Profiles are the most important category; this category samples all of the others. The

four categories are all a function of cycles, but should not to be confused with the five stages of the S-B-V diagram. Within each stage of the S-B-V diagram, microstructural changes occur with depth, on a macroscopic scale, in the DER, and at the surface.

Table XIV: Data Categories

Category	Description
Pro	Changes in Depth Profiles
Mac	Overall Macroscopic Changes
DER	Changes in the Dark Etching Region
Sur	Changes at the Surface

4.3 Changes Produced During Stages I and II

In Stage I, no detectable microstructural changes are observed. However, at the end of Stage I there is a transition region from Stage I to Stage II in which profiles of retained austenite decrease. Figure 47 consists of retained austenite profiles with depth as measured from Mössbauer spectroscopy and light microscopy for CRXX. Note that the amount of retained austenite at the surface stays relatively constant until about 10^6 cycles and then begins to transform. Figures 48 and 49 confirm a reduced retained austenite in the region of 0.1 to 0.3 mm below the surface after 10^6 cycles. Figure 50

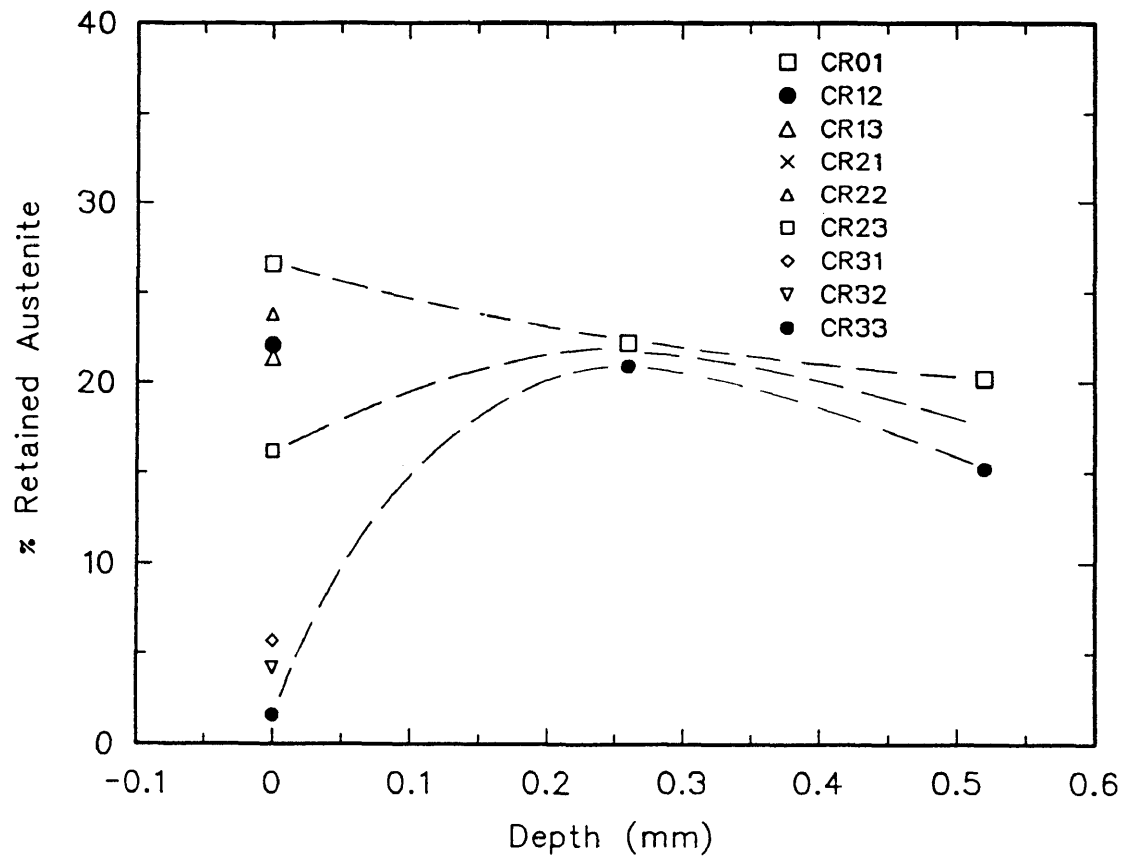
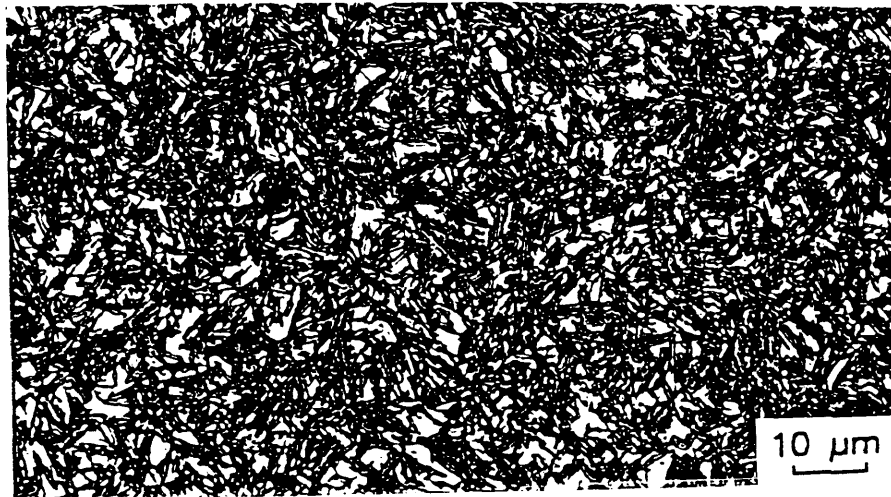
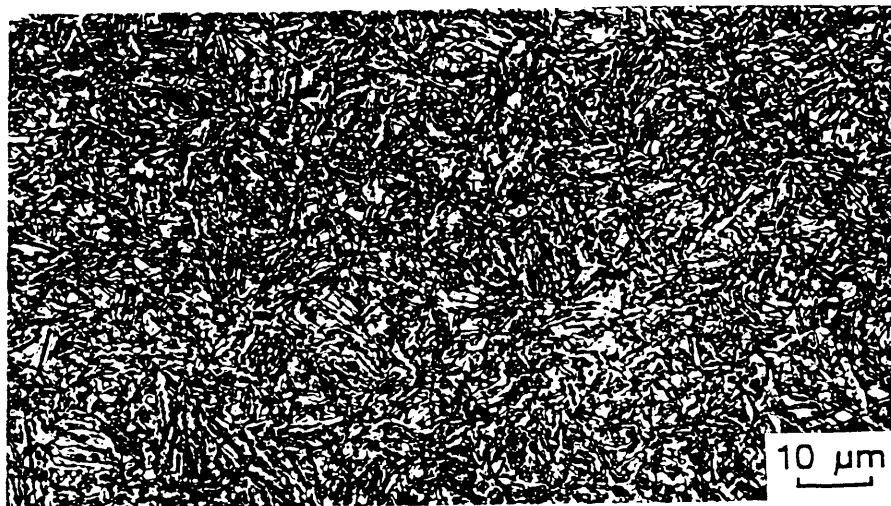


Figure 47: Plots of retained austenite profiles as observed by Mössbauer spectroscopy and light microscopy for CRXX Caterpillar specimens.

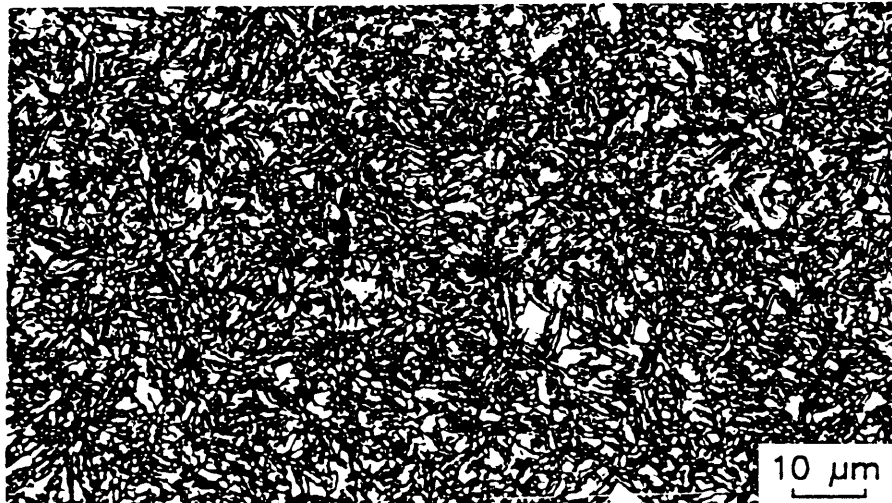


a



b

Figure 48: Light micrographs showing the area 0.1-0.3 mm below the surface of a) CD01, 11.7% retained austenite, and b) from the same area beneath the wear track of CD23, 4.8% retained austenite, 1000X, 2% nital etch for 15 seconds, followed by an etch of 10% sodium metabisulfite by weight in water for 20 seconds.



a



b

Figure 49: Light micrographs showing the area 0.1-0.3 mm below the surface of a) CR01, 8.5% retained austenite, and b) from the same area beneath the wear track of CR23, 1.1% retained austenite, 1000X, 2% nital etch for 15 seconds, followed by an etch of 10% sodium metabisulfite by weight in water for 20 seconds.

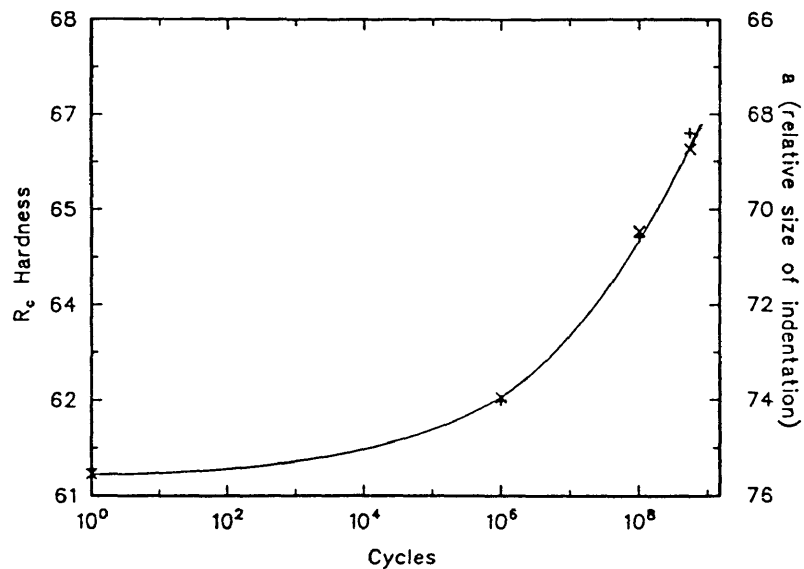


Figure 50: R_c hardness versus cycles at 0.24 mm below the surface, data from CRXX hardness profiles. The parameter "a" is an average of the horizontal and vertical measurements of the microhardness indentations.

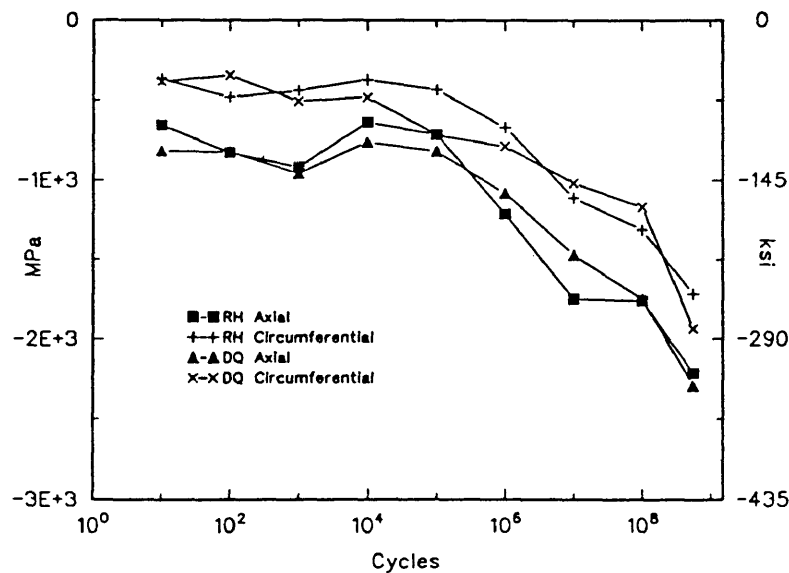


Figure 51: Plot of surface compressive residual stress in the axial and circumferential directions in both the CDXX and CRXX specimens as a function of cycles.

shows an increase in hardness in this same area as a function of cycles. The elbow in the surface residual stress curve is at approximately 10^6 cycles as well, as shown in Figure 51.

During Stage II, a dark etching region forms due to the decomposition of martensite to ferrite. The ferrite formed etches dark and this etching effect occurs on a macroscopic scale visible to the naked eye although it is limited to the DER. Macroscopic observations shows the DER that formed in both the CDXX and CRXX Caterpillar specimens between 10^7 and 10^8 cycles. Retained austenite continues to decrease, Figure 47. Residual stress profiles become even more compressive. Figure 52 is for the Caterpillar specimens and shows residual stress profiles in the axial and circumferential directions for CD01, CD23, CR01, and CR23. Hardness profiles and traverses of these same specimens show increased hardness as shown in Figures 53 through 55. Increases in hardness profiles for CDXX and CRXX specimens are very similar, Figure 53. Figure 53b and Figure 54 are from different planes of CR33, the circumferential and axial. However, they show similar trends. Profilometer traces, Figure 56, at the surface show limited wear up until 10^8 cycles in the Caterpillar specimens. Between 10^8 and 5×10^8 cycles extensive wear

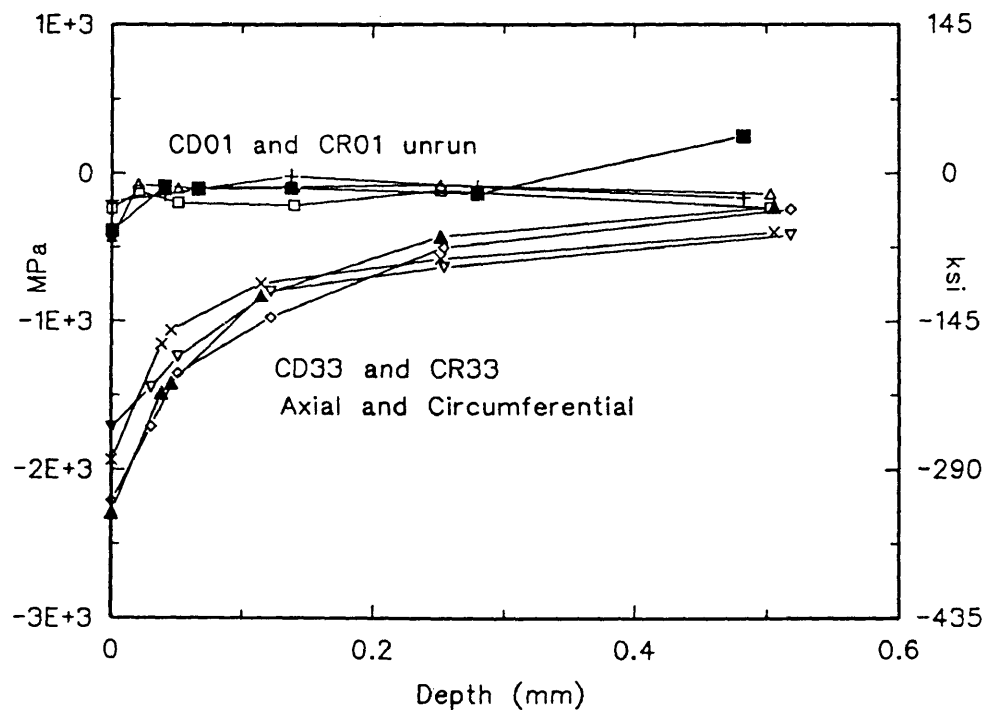


Figure 52: Plot of residual compressive axial and circumferential stress depth profiles for Caterpillar specimens CD01, CD33, CR01 and CR33.

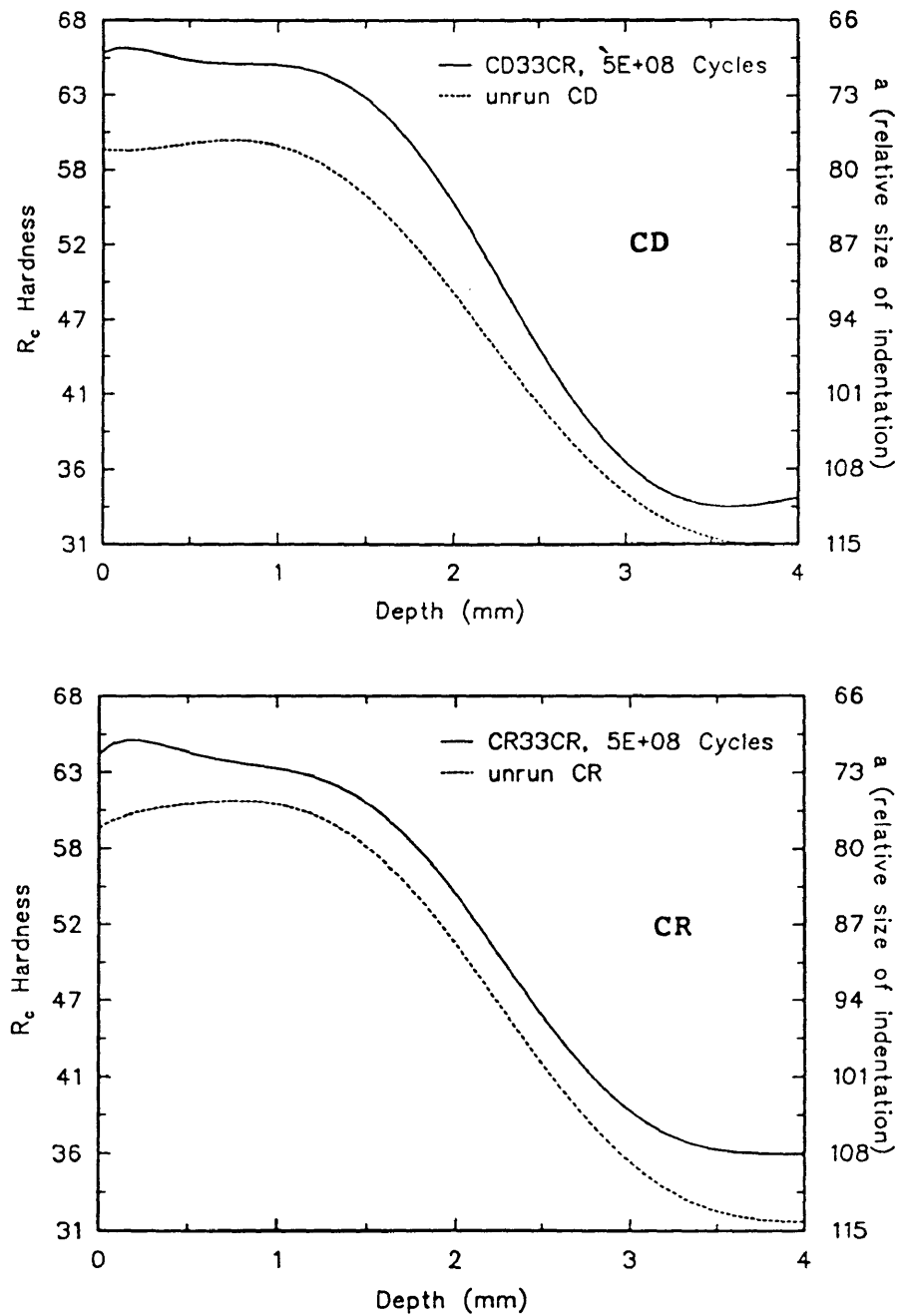


Figure 53: Hardness profiles from C section of Caterpillar specimens CD01, CD33, CR01, and CR33. A Vickers type, diamond shaped hardness indenter at 300 g load applied for 15 seconds.

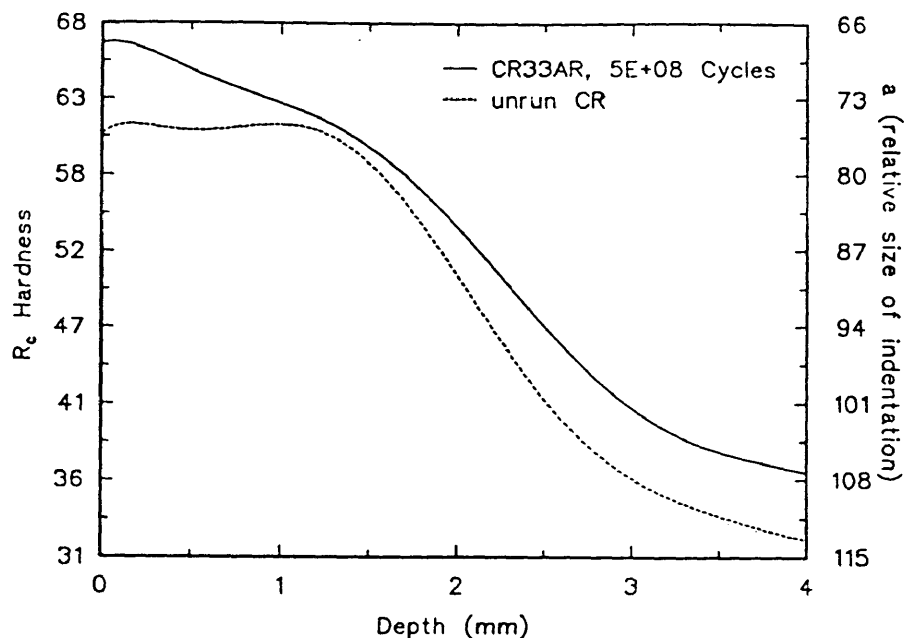


Figure 54: Hardness profiles for A section of Caterpillar specimens CR01 and CR33. A Vickers type, diamond shaped hardness indenter at 300 g load applied for 15 seconds.

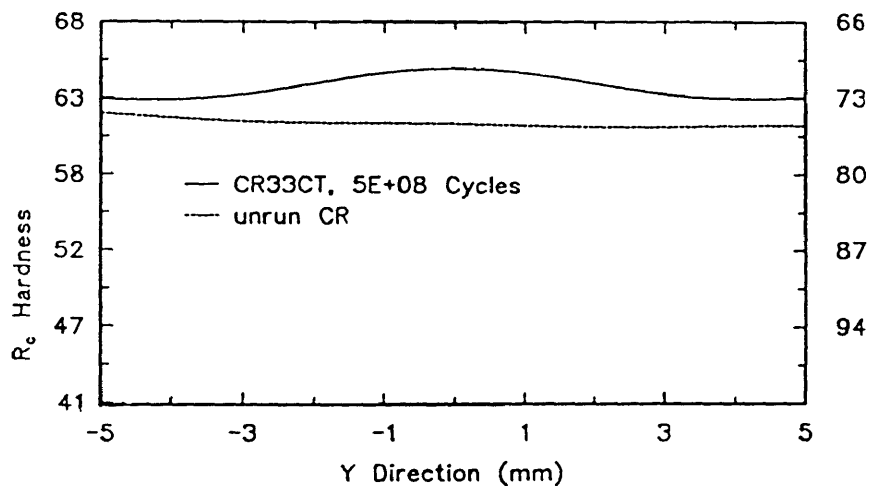


Figure 55: Increase of hardness in traverses parallel to the surface at a depth of 0.24 mm on A section of CR01 and CR33. A Vickers type, diamond shaped hardness indenter at 300 g load applied for 15 seconds.

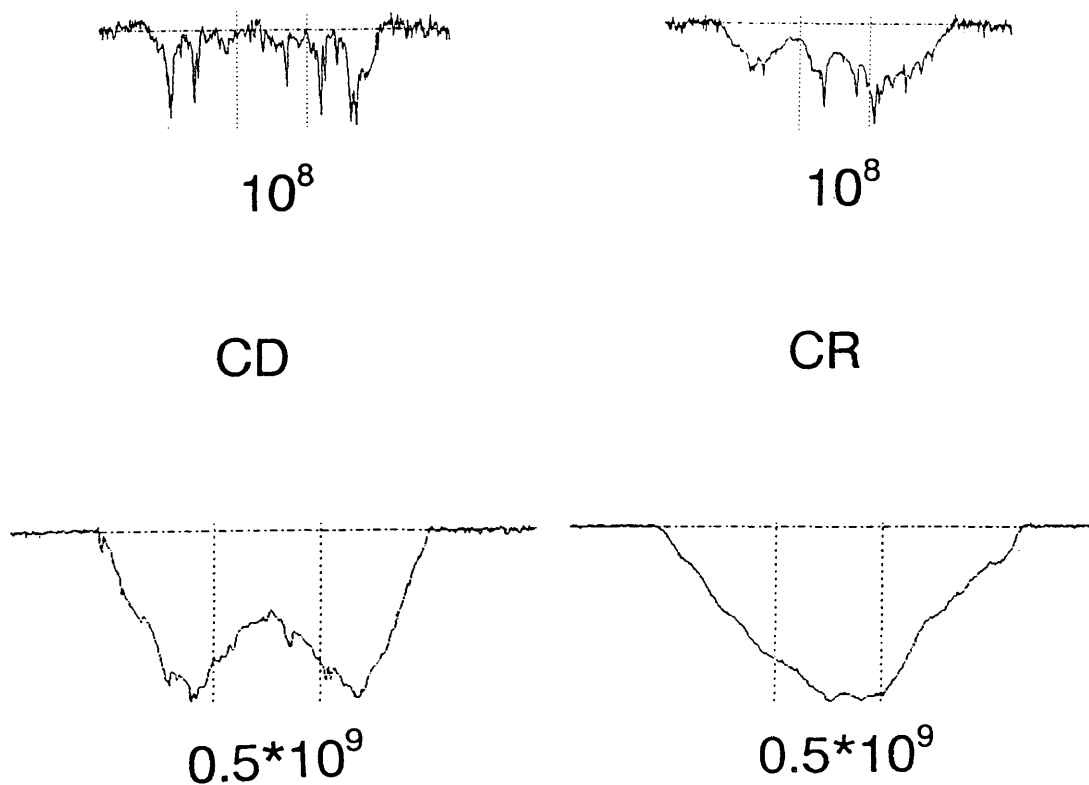


Figure 56: Profilometer traces of CD32, CD33, CR32, and CR33. The width of the wear track increases from approximately 4 mm to 6 mm and the depth from 4 μm to 30 μm for CDXX and 6 μm to 65 μm for CRXX, courtesy of Caterpillar Inc.

occurs in both the CDXX and CRXX specimens. The width of the wear track increases from approximately 4 mm to 6 mm and the depth from 4 μm to 30 μm for CDXX and 6 μm to 65 μm for CRXX between 10^8 and $5 \cdot 10^8$ cycles as shown in the profilometer traces.

The overall (Mac) etching of CR01 and CR33 shows a marked difference. Figures 57 and 58 show micrographs at 50X and image analysis profiles of CR01 and CR33.

4.4 Changes Produced During Stages III and IV

During Stages III and IV, the 30 degree and 80 degree bands develop in the DER. No white etching bands were observed in the Caterpillar specimens cycled to $5 \cdot 10^8$ cycles, but were observed in a Timken specimen cycled to 10^9 cycles. The angles of white etching bands in TR41 are 24 degrees and 82 degrees. White etching bands are not visible to the naked eye. Figure 59 shows these white etching bands and presents regions of highest τ_{xz} stresses on the xz and yz planes of TR41. A rough correlation is evident between the regions of highest τ_{xz} stress and the white etching bands. Figure 59a is on the yz plane and Figure 59b is on the xz plane. Figure 59 is from the MathCAD analysis discussed earlier. Compare this figure with Figure 40. Note that the highest regions of τ_{xz} in

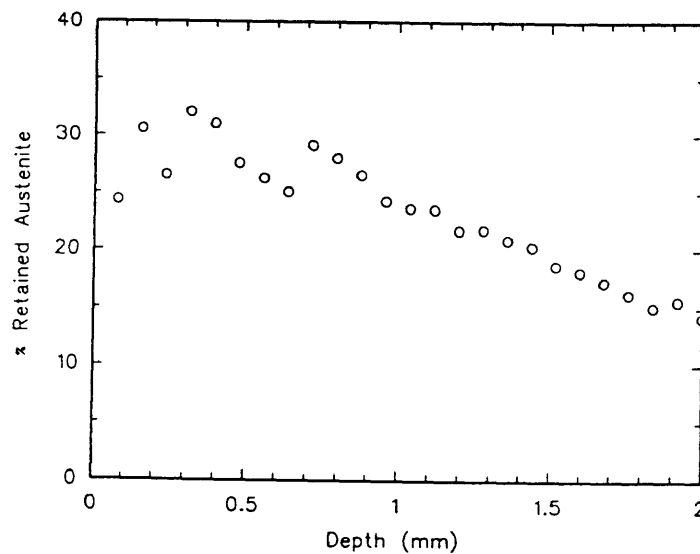
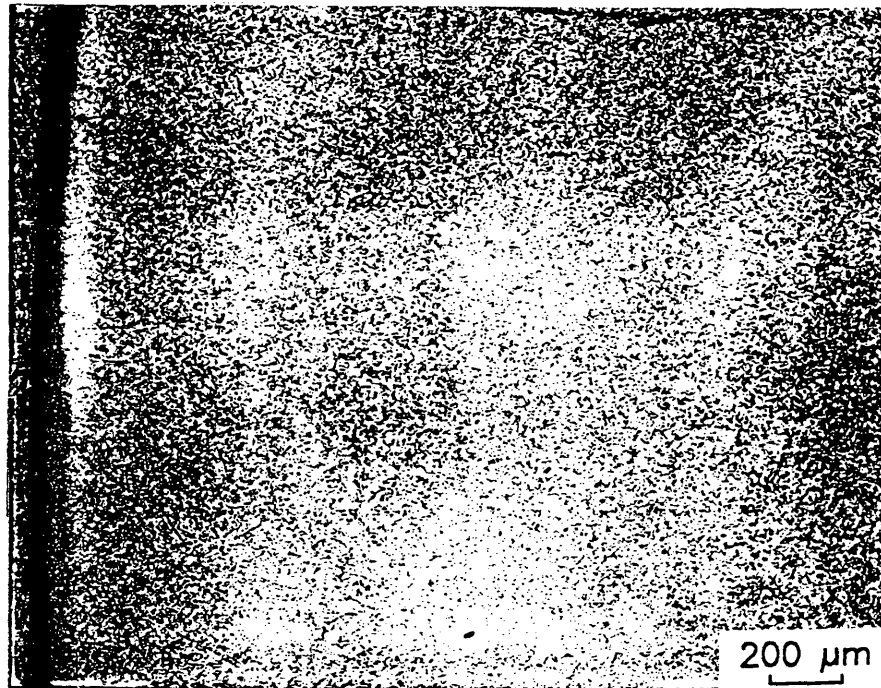


Figure 57: Micrograph at 50X and image analysis profile of CR01 on xz plane. Initial settings on image analyzer at surface were set so that surface measurements approximated the retained austenite values from Mössbauer spectroscopy, 2% nital etch for 15 seconds, followed by an etch of 10% sodium metabisulfite by weight in water.

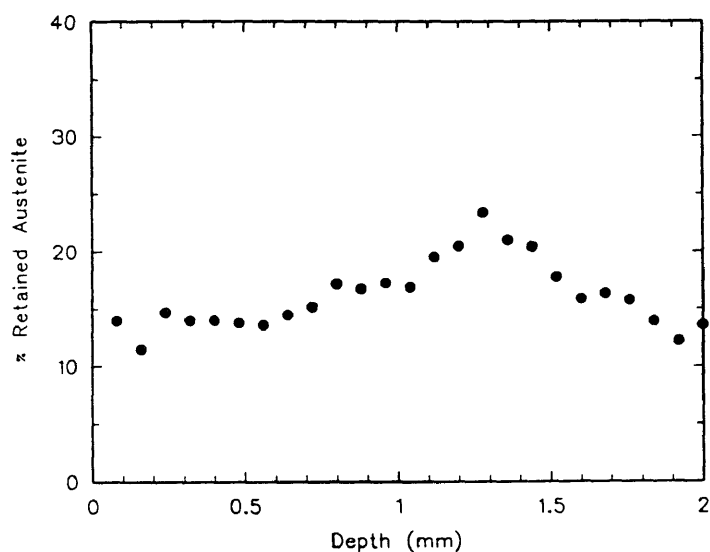
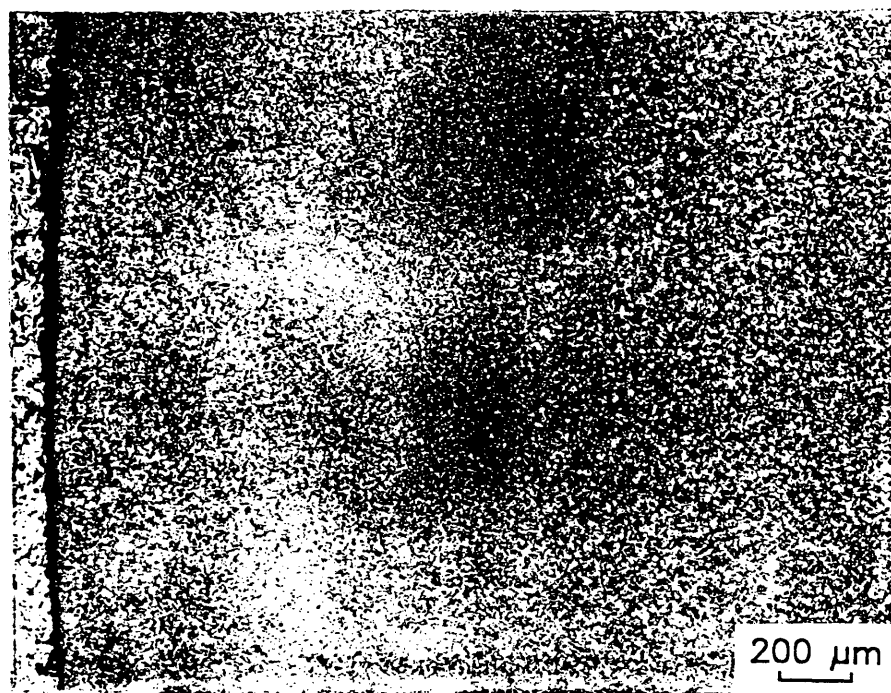


Figure 58: Micrograph at 50X and image analysis profile of CR33 on xz plane. Settings on image analyzer at surface were set so that surface measurements approximated the retained austenite values from Mössbauer spectroscopy, 2% nital etch for 15 seconds, followed by an etch of 10% sodium metabisulfite by weight in water.

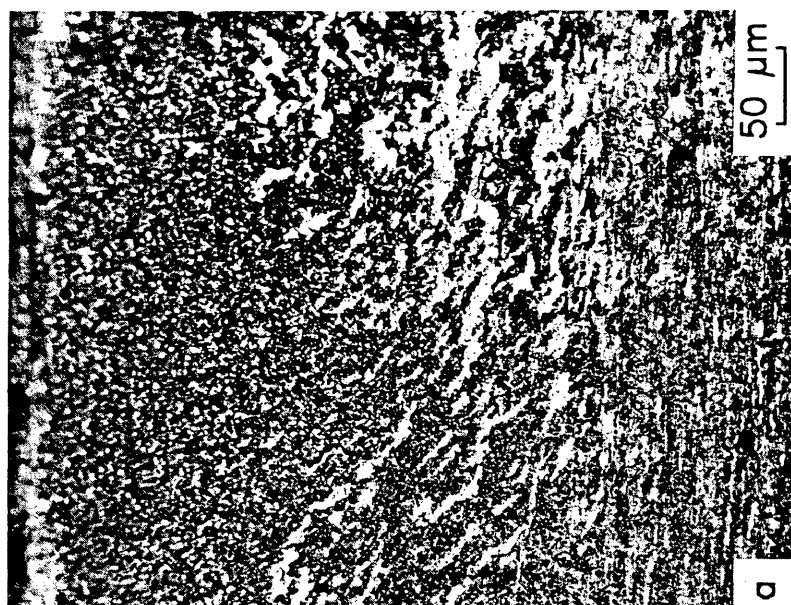
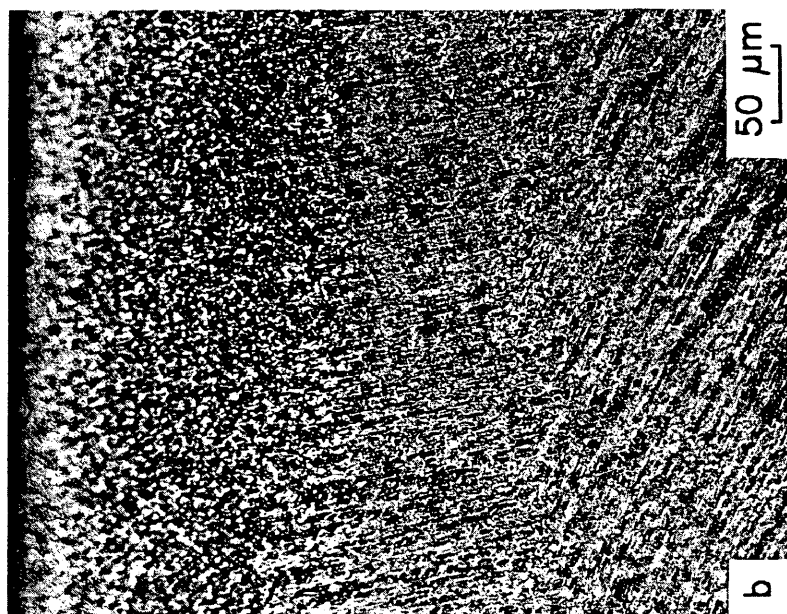


Figure 59b point towards the direction of rolling, which is consistent with the observed direction of the bands. This correlation of τ_{xz} regions with white etching bands is for negative τ_{xz} values at $x=-0.5$ mm. However, the material is also stressed by the same magnitude of positive τ_{xz} stress at $x=0.5$ mm, as the roller rolls over the surface, Figure 5.

As measured by Mössbauer spectroscopy, the carbide content is higher at the surface of TR41 than it is at the surface of TR01; shown by a plot of carbide content at the surface versus cycles, Figure 60. Retained austenite profiles of TR01, TR32, and TR41, Figure 61, show decreases as expected. Hardness profiles of TR41 are decreased to below the untested levels due to the microstructural changes as shown in Figure 62.

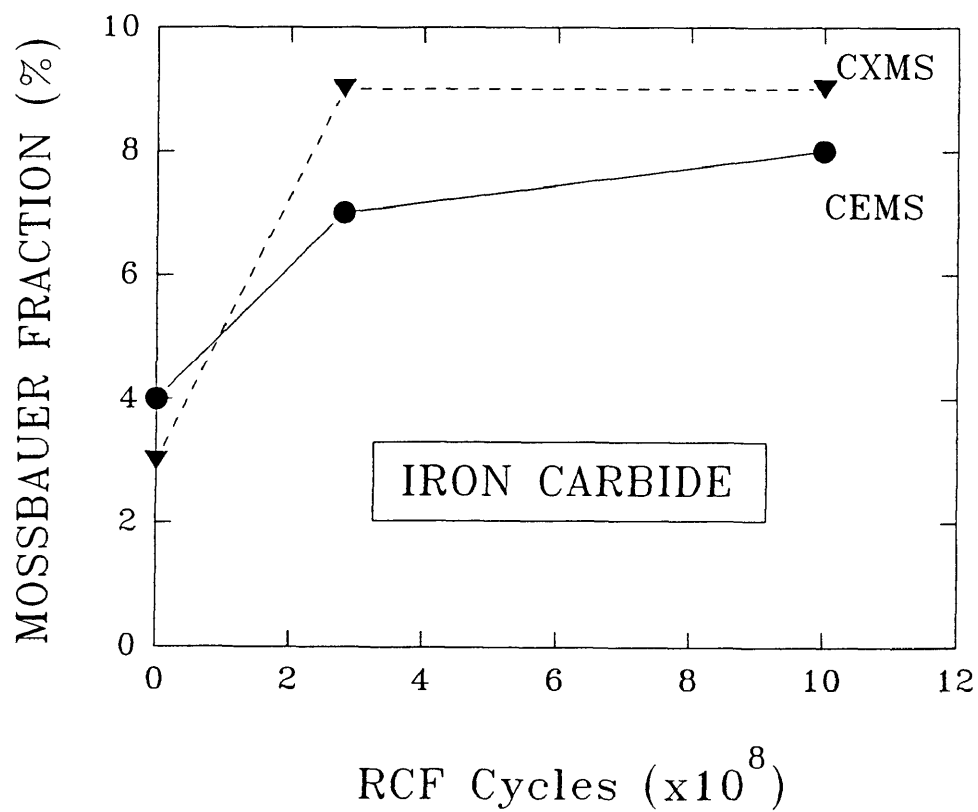


Figure 60: Carbide volume percent versus cycles for CEMS and CXMS Mössbauer spectroscopy measurements of the surface of Timken specimens, TR01, TR32, and TR41.

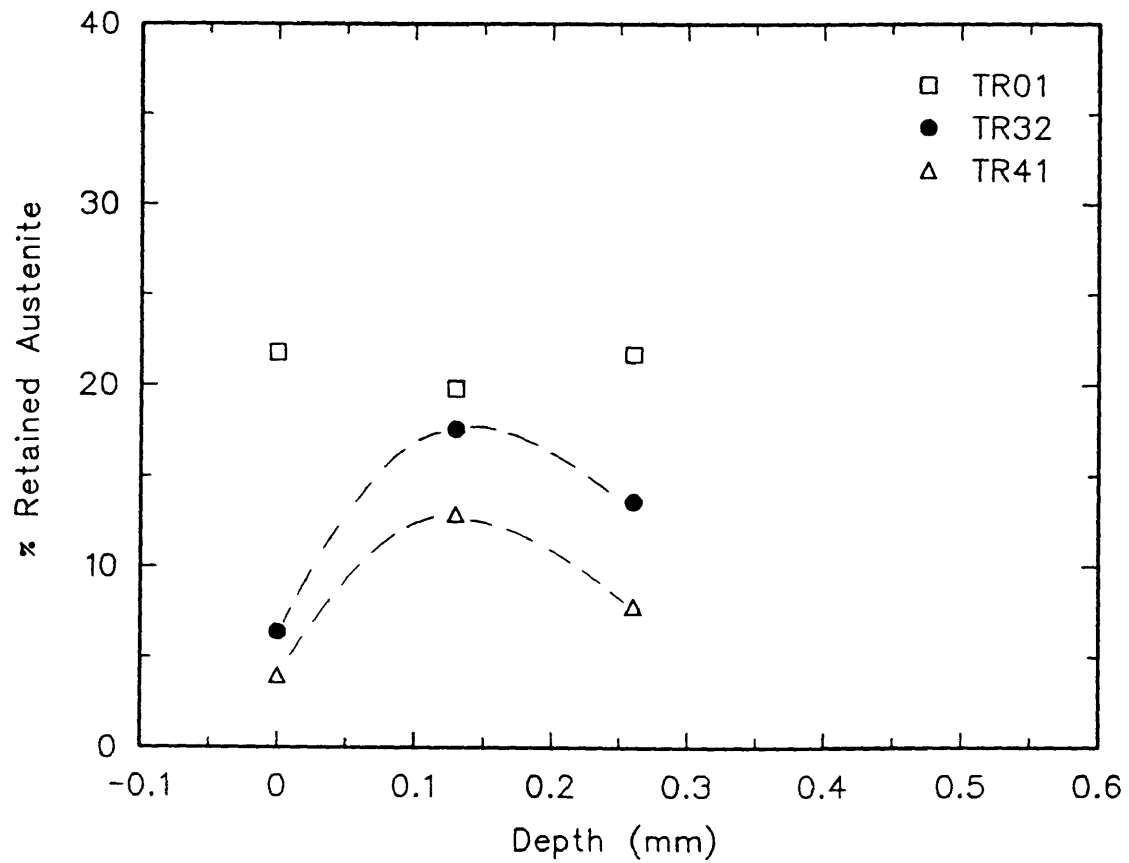


Figure 61: Plots of retained austenite profiles as measured with Mössbauer spectroscopy for Timken specimens.

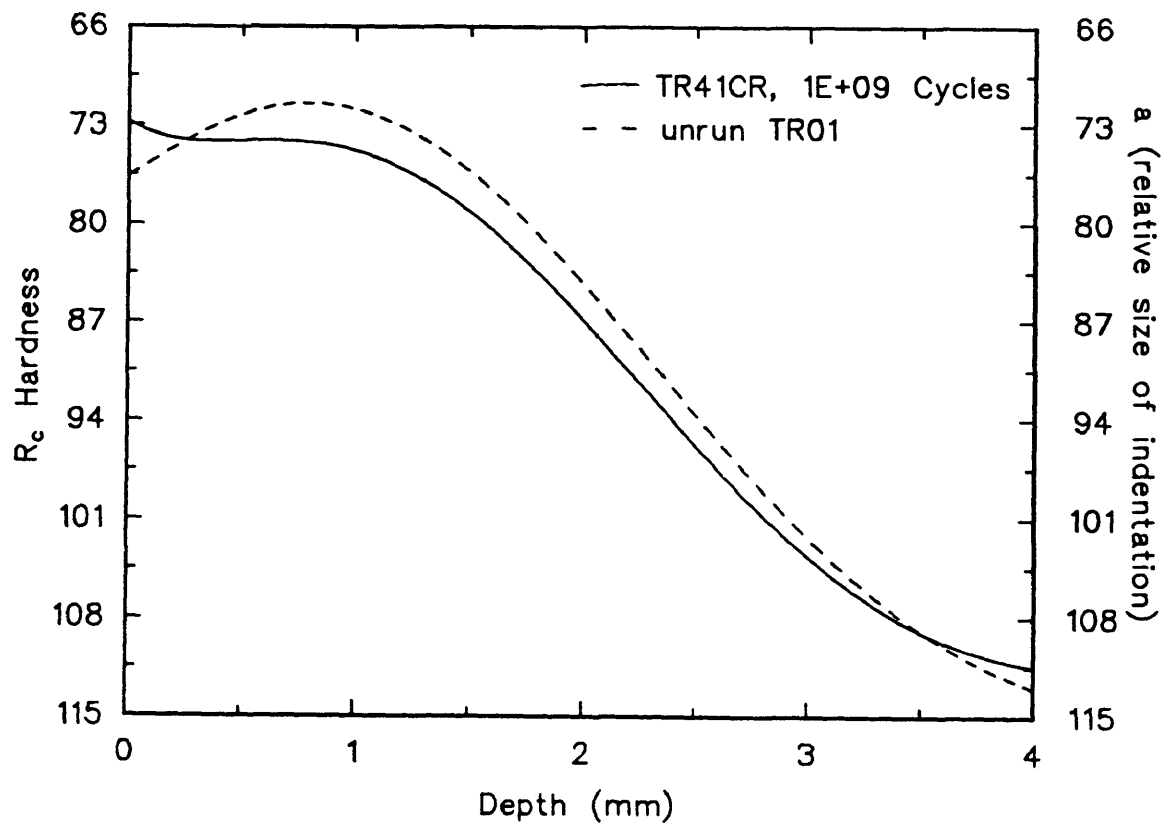


Figure 62: Hardness profiles for C section of Timken specimens TR01 and TR41 showing that in Stage IV (Figure 43) the hardness profile is below the untested level. A Vickers diamond shaped hardness indenter at 300 g load applied 15 seconds.

5.0 DISCUSSION

As observed in the literature, these microstructural changes occur in carburized as well as through-hardened bearing steels. Therefore, the initial differences in the residual stress profiles of these two very different types of steels must be overcome by the imposed residual stress. As discussed below, the relative consistency of the angles at which white etching bands occur may be due to a consistent type of imposed residual stress profile that is common to both types of steel after large numbers of rolling fatigue cycles at high loads. The following sections discuss the formation of the observed microstructural changes within the framework of the Swahn et. al. diagram, Figure 43.

5.1 Discussion of Stages I and II

The results presented above for the Caterpillar specimens confirm that there is an incubation stage in RCF, even at relatively high contact loads, during which there are no detectable changes in microstructure profiles, hardness profiles, or residual stress profiles. This stage of RCF is identified as Stage I in Figure 43. Following

this period, there are dramatic changes in retained austenite content, hardness, and residual stresses. The retained austenite transforms to martensite with increasing cycles of rolling contact. The fact that the surface retained austenite only begins to change after 10^6 cycles provides evidence for strain induced martensite formation. Typically, an incubation period, during which strain accumulates, is a characteristic feature required to initiate strain-induced austenite to martensite transformation (17). The transformation of retained austenite to martensite correlates well with the hardness changes and residual stress changes observed in the transition region between stages I and II, Figure 43. Clearly hardness increases were directly related to increases in the volume fraction of martensite formed by the strain-induced transformation of austenite. Strain hardening of martensite might also increase hardness, but the magnitude of the point in the RCF cycles at which this becomes significant cannot be established from the data obtained in this study. The contact stress of 3380 MPa, based on compression tests of martensite and austenite in 0.8 pct C steels, is well above the stress associated with significant strain hardening of martensite. Possibly strain hardening of martensite becomes a factor only after

significant amounts of austenite have transformed. At any rate, there is an excellent correlation of decreases in retained austenite with hardness increases in Stage II.

The dramatic increase in compressive residual stress profiles are explained by the transformation of retained austenite. As austenite transforms there is a volume expansion, but this volume expansion is restrained by the hard subsurface microstructure of the carburized case. As a result, instead of the volume expansion produced by martensite formation which occurs in an unconstrained microstructure, compressive stresses are created. Figure 52 shows that the compressive stresses reach very high values, on the order of the compressive yield stresses of martensite/austenite microstructures in 0.8 pct C steels, and just as with the hardness changes, the residual stress changes correlate directly with the transformation of the retained austenite.

Significant wear begins at the surface, sometime between 10^8 and 5×10^8 cycles in the Caterpillar specimens, Figure 56. The location of the DER is due to the region of highest τ_{45} shear stress (12,23,59). Wear is probably the result of strain hardening at the surface leading to microcracks and microspalls. Significant etching differences besides the DER and white etching bands are

observed in CR01 as compared to CR33. Differences in micrographs at 50X (Mac) of CR01 versus CR33 are significant.

Whether microstructural change occurs first at the surface or at depth is not known. Light microscopy performed on the Caterpillar specimens indicates a significant reduction in retained austenite below the surface (DER) after 10^6 cycles as measured with an image analyzer. Mössbauer results indicate that no detectable microstructural change at the surface (Sur) has occurred at 10^6 cycles. Therefore, it would seem that change occurs first at depth. However, hardness measurements beneath the surface (DER) of tested Caterpillar specimens, Figure 50, show an elbow at 10^6 cycles which corresponds to the elbow observed in the transformation of surface (Sur) retained austenite. Therefore, it is not known whether microstructural change occurs first below the surface or at the surface and also whether the rate of change varies as a function of depth.

5.2 Discussion of Stages III and IV

As discussed below, the 30 and 80 degree white etching bands form because of increasing dislocation density due to τ_{45} shear stress; first, in the 30 degree direction and

then, in the 80 degree direction. Zwirlein and Schlicht took a profile of σ_e and showed that by adding a Stage IV residual stress profile to it and recalculating the principal stresses, the resulting τ_{45} shear stress is reoriented so that it acts in the 80 degree direction. Their explanation for the 30 degree bands is more difficult to understand. They compare the new principal stresses and by subtracting the mean stress from all of the principal stresses show that a "crack opening" relative tensile stress acts perpendicular to the 30 degree direction, Figure 19. However, Zwirlein and Schlicht's 30 degree band explanation is based on the residual stress profile in Stage IV. The residual stress profile during Stage III may be different and not result in the "relative tensile stress" in the required direction for 30 degree bands. Therefore, other researchers have associated the 30 degree bands with τ_{45} (11,21,26) and it seems plausible that the residual stress profile in Stage III may be such that it orients τ_{45} in the 30 degree direction.

The initiation of the 30 degree bands probably starts when the DER gets soft enough due to DER ferrite formation for increased shear in the 30 degree direction and the initiation of 80 degree bands is when the residual stress and density of 30 degree bands is such that slip occurs in

the 80 degree direction. The initial residual stress condition, through hardened or carburized, is overridden by the imposed residual stresses, Figures 13 and 14.

Surface wear occurred in the Caterpillar specimens during Stage II when the DER is forming beneath the surface. The shape of regions of highest τ_{xz} were shown to roughly correlate with the areas of white etching bands. The mechanisms behind these two observations are not understood.

5.3 Discussion of τ_{45} Versus τ_{xz}

The controversy as to whether τ_{45} or τ_{xz} is the stress responsible for rolling contact fatigue has historically centered around three issues:

1. How can microstructural changes during RCF be caused by τ_{45} when the white etching bands look more like they were made by a fully reversing stress cycle?
2. The depth of crack initiation usually matches up better with the depth of highest τ_{xz} than the depth of highest τ_{45} .
3. Many cracks propagate parallel to the contact surface. How can a τ_{45} mechanism explain the propagation of these cracks?

Each of these issues is discussed below.

5.3.1 τ_{45} Versus τ_{xz} , Fully Reversing Stress Cycle

Bhargava et. al. (60) have shown that as one RCF

element rolls over the other that the orientation of the principal stresses acting on a point in the material rotate, Figure 63. Bhargava et. al. also found the directions in which the hydrostatic stresses were favorable for plastic flow. Two of these favorable directions match well with the inclinations of the white etching bands. Thus a fully reversing τ_{45} effect may be possible.

5.3.2 τ_{45} Versus τ_{xz} , Depth to Crack Initiation

According to Zwirlein and Schlicht's theory, the residual stress profile in Stage IV is always similar to the one shown in Figure 19a, resulting in the stress distribution shown. Since the white etching bands are seen in both carburized and through hardened bearing steels it is reasonable to assume that the imposed residual stresses can overcome the initial residual stresses due to processing. Usually the depth of crack initiation matches better with τ_{xz} , $0.50b$, than with τ_{45} , $0.78b$; b is half of the width of the wear track. However, as shown in Figure 19a, the residual stress profile can cause the peak σ_e stress, essentially τ_{45} as discussed earlier, to occur at $0.50b$. This would lead into Stage V, cracking, with the depth of maximum shear at $0.50b$. If the imposed stresses are such that the etching effects do not occur, then cracking should initiate at $0.78b$, the original depth to

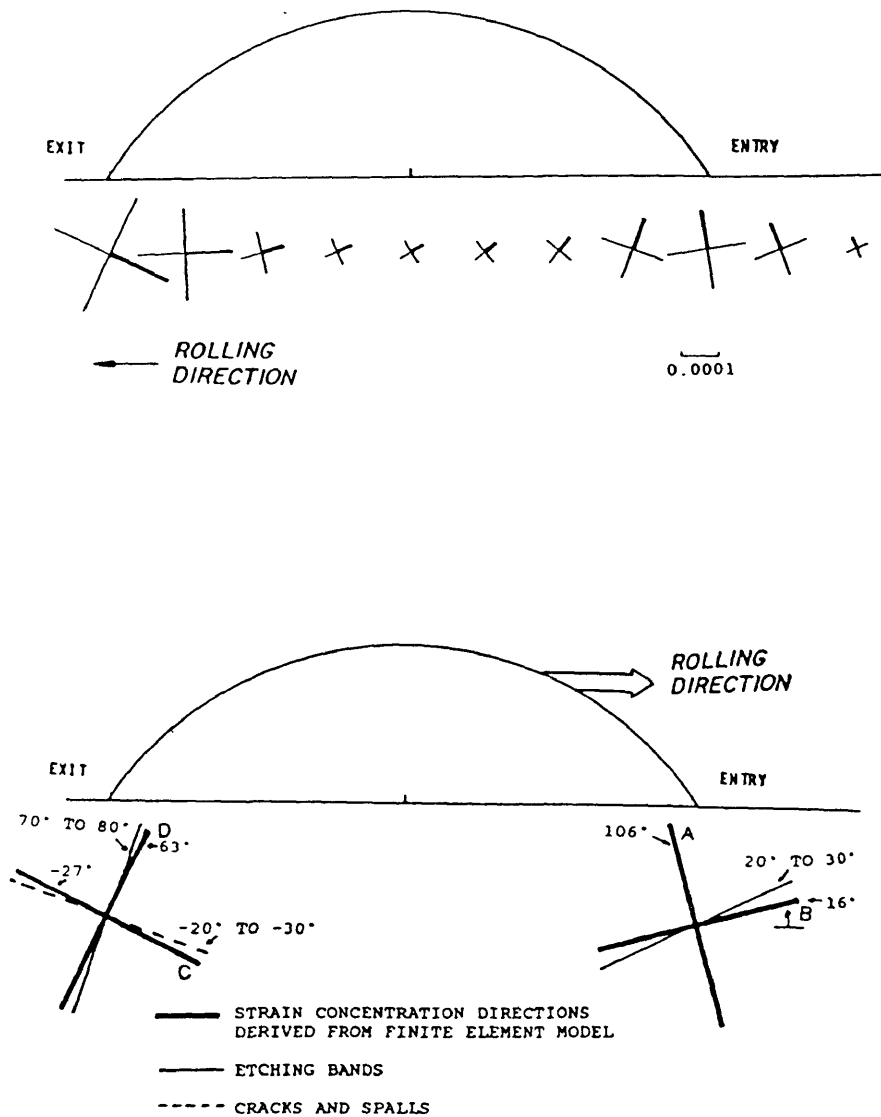


Figure 63: Rotation of applied principal stresses as one rolling contact fatigue element rolls over the other (60).

maximum τ_{45} .

5.3.3 τ_{45} Versus τ_{xz} , Cracks Parallel to the Surface

At first this seems to be an issue in favor of τ_{xz} , because even with the changes in orientation of the principal stresses, the τ_{45} shear stress probably does not act parallel to the surface. However, Zwirlein and Schlicht's "relative tensile stress" conceivably could. In this case, the principal stresses and not a shear stress would be responsible for this type of crack propagation. Additionally, as stated by Voskamp (21),

"The orthogonal shear stress amplitude reaches a maximum simultaneously in two planes, one parallel and one perpendicular to the raceway. While the probability for cracks to develop is in principle the same for both planes, crack propagation is normally observed only in that plane parallel to the surface," (A.P. Voskamp, "Material Response to Rolling Contact Loading," Journal of Tribology, vol. 107, July, 1985, pp. 359-366.

Figure 64 is a schematic of the orthogonal shear stresses acting on a stress cube. Theoretically, there is equal probability of the vertical orthogonal stress, which has the same magnitude as the horizontal component, to cause shear as there is for the horizontal component to cause cracking parallel to the surface (23) and thus, the orthogonal shear stress does not fully explain cracking parallel to the surface since cracks perpendicular to the surface are not seen until later.

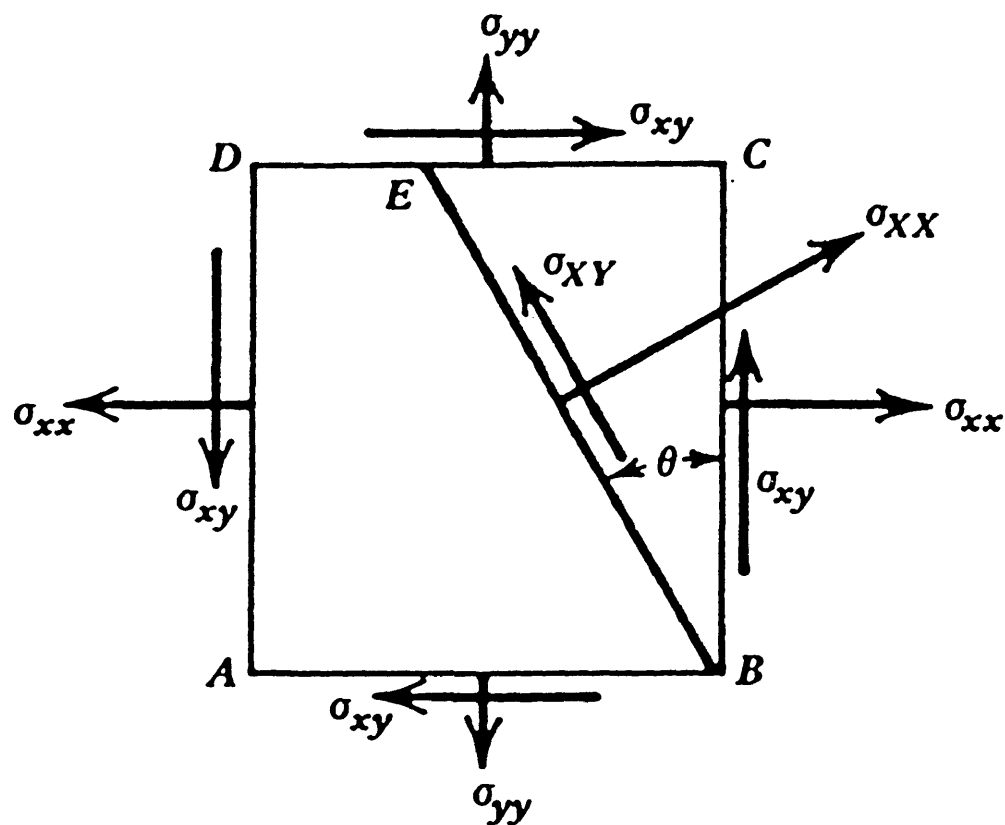


Figure 64: Schematic of the orthogonal shear stresses acting on a stress cube, σ_{xz} is the same as τ_{xz} (9).

6.0 CONCLUSIONS

1. High contact loads lead to four stages of fatigue life in carburized steels. The first stage serves as an incubation period during which strain accumulates for subsequent changes. No detectable microstructural changes are observed in Stage I. Changes in retained austenite profiles and residual compressive stress profiles begin after Stage I. In Stage II, retained austenite decreases and residual stresses become more compressive. A dark etching region begins to form due to decomposition of the martensite in the matrix. Stage III and Stage IV are continuations of these microstructural changes in which bands of ferrite are nucleated within the dark etching region. Hardness decreases due to the formation of these bands, and in Stage IV eventually drops below the hardness for untested specimens.
2. The same types of microstructural changes, which occur during RCF, are observed in both carburized and through-hardened steels.
3. It is concluded that the τ_{45} stress is the stress responsible for the RCF-induced microstructural changes observed (DER, 30 degree bands, and 80 degree bands).

7.0 SUMMARY

The following list is a summary of the accomplishments achieved during this project:

1. Setup of Rolling Contact Fatigue Laboratory.
2. Redesign of Lubrication System.
3. MathCAD Stress Analysis Program to Calculate σ_1 , σ_2 , σ_3 , τ_{45} , τ_{oct} , and σ_e .
4. Correlation of Wear to Stage II in which the DER is forming beneath the surface Caterpillar Specimens.
5. Correlation of Shape of τ_{xz} Regions to White Etching Areas.
6. Theoretical Work on Explanation of τ_{45} Versus τ_{xz} controversy.

8.0 REFERENCES

- 1 R.E. Denning and S.L. Rice, "Surface Fatigue Research with the Geared Roller Test Machine," manuscript of a paper for the SAE Automotive Engineering Congress and Exhibition, Detroit, MI, January 14-18, 1963.
- 2 Rolling Contact Fatigue Testing of Bearing Steels, A Symposium Presented at May Committee Week, J.J.C. Hoo Editor, ASTM STP 771 04-771000-02, Phoenix, AR, May 12-14, 1981, p. 86.
- 3 Rolling Contact Fatigue Testing of Bearing Steels, A Symposium Presented at May Committee Week, J.J.C. Hoo Editor, ASTM STP 771 04-771000-02, Phoenix, AR, May 12-14, 1981, p. 85.
- 4 Rolling Contact Fatigue Testing of Bearing Steels, A Symposium Presented at May Committee Week, J.J.C. Hoo Editor, ASTM STP 771 04-771000-02, Phoenix, AR, May 12-14, 1981, p. 85.
- 5 D.K. Lawrentz, "Operation and Maintenance Manual for the Timken Company Rolling Contact Fatigue Machines," Timken Research, Canton, Ohio, January, 1991.
- 6 Rolling Contact Fatigue Testing of Bearing Steels, A Symposium Presented at May Committee Week, J.J.C. Hoo Editor, ASTM STP 771 04-771000-02, Phoenix, AR, May 12-14, 1981, p. 107.
- 7 R.E. Miller, D.L. Williamson, and G. Krauss, "Rolling Contact Fatigue of Case-carburized Steels," ASPPRC Research Report MT-SRC-090-014, Colorado School of Mines, Golden, CO, September 1, 1990, pp. 102-122.
- 8 A.E.H. Love, The Mathematical Theory of Elasticity, 4th Edition, Dover Publication, New York, NY, 1944, p. 198.
- 9 A.P. Boresi and O.M. Sidebottom, Advanced Mechanics of Materials, 4th Edition, John Wiley and Sons, New York, NY, 1985, pp. 599-621.

- 10 H.R. Thomas and V.A. Hoersch, "Stresses Due to the Pressure of One Elastic Solid on Another," Bulletin of Engineering Experiment Station No. 212, University of Illinois, 1930.
- 11 J.A. Martin, S.F. Borgese, A.D. Eberhardt, "Microstructural Alterations of Rolling-Bearing Steel Undergoing Cyclic Stressing," Journal of Basic Engineering, September, 1966, pp. 555-567.
- 12 Rolling Contact Fatigue Testing of Bearing Steels, A Symposium Presented at May Committee Week, J.J.C. Hoo Editor, ASTM STP 771 04-771000-02, Phoenix, AR, May 12-14, 1981, p. 92.
- 13 R.E. Miller, D.L. Williamson, and G. Krauss, "Rolling Contact Fatigue of Case-carburized Steels," ASPPRC Research Report MT-SRC-091-016, Colorado School of Mines, Golden, CO, September 1, 1991, pp. 71-88.
- 14 F.M. Kustas, "High Current Ion Implantation of 440C Steel for Increased Rolling Contact Fatigue Resistance," ASPPRC Research Report MT-SRC-090-005, Colorado School of Mines, Golden, CO, March 1, 1990, pp. 58,61.
- 15 W.J. Greenert, "The Toroid Contact Roller Test as Applied to the Study of Bearing Materials," Journal of Basic Engineering, 1962, pp. 181-191.
- 16 A. Yoshida, "Some Problems in the Design of Surface-Hardened Gears for Tooth Surface Durability," ASME International Journal, Series III, vol. 32, Number 3, 1989, pp. 356-364.
- 17 G.B. Olson and M. Cohen, "Kinetics of Strain-Induced Martensite Nucleation," Metall. Trans. A., Vol. 6A, 1975, pp. 791-795.
- 18 Y. Murakami, Y. Matsumoto, and K. Uemura, United States Patent #4930909, June 5, 1990.
- 19 H. Muro and N. Tsushima, "Microstructural, Microhardness and Residual Stress Changes Due to Rolling Contact," Wear of Materials, 1970, pp. 313,327.

- 20 D. Zhu, F. Wang, Q. Cai, M. Zheng, and Y. Cheng, "Effect of Retained Austenite on Rolling Element Fatigue and its Mechanisms," in The International Conference on Wear of Materials, ed. by K.C. Ludema, Vancouver, B.C. Canada, 1985, p. 577.
- 21 A.P. Voskamp, "Material Response to Rolling Contact Loading," *Journal of Tribology*, vol. 107, July, 1985, pp. 359-366.
- 22 K. Fujita and A Yoshida, "Macroscopic and Microscopic Changes in the Surface Layers of Annealed and Case-Hardened Steel Rollers Due to Rolling Contact," *Wear of Materials*, 1977, pp. 301-313.
- 23 K. Bohm, H. Schlicht, O. Zwirlein, and R. Eberhard, "Nonmetallic Inclusions and Rolling Contact Fatigue," *Bearings Steels: The Rating of Nonmetallic Inclusion*, ASTM STP 575, ASTM, 1975, pp. 96-113.
- 24 Bearing Steels: The Rating of Nonmetallic Inclusions, A Symposium Presented at May Committee Week, J.J.C. Hoo Editor, ASTM STP 575 04-575000-02, Boston, MA, May 22-24, 1974, p. 55.
- 25 J. Murza, private communication, March, 1992.
- 26 H. Swahn, P.C. Becker, and O. Vingsbo, "Martensite Decay During Rolling Contact Fatigue in Ball Bearings," *Metall. Trans. A.*, vol. 7A, 1976, pp. 1099-1110.
- 27 Rolling Contact Fatigue Testing of Bearing Steels, A Symposium Presented at May Committee Week, J.J.C. Hoo Editor, ASTM STP 771 04-771000-02, Phoenix, AR, May 12-14, 1981, p. 361.
- 28 Zwirlein and Schlicht, "Rolling Contact Fatigue Mechanisms - Accelerated Testing Versus Field Performance," in Rolling Contact Fatigue Testing of Bearing Steels, A Symposium Presented at May Committee Week, J.J.C. Hoo Editor, ASTM STP 771 04-771000-02, Phoenix, AR, May 12-14, 1981.

- 29 G.T. Hahn, V. Bhargava, C.A. Rubin, Q. Chen, and K. Kim, "Analysis of the Rolling Contact Residual Stresses and Cyclic Plastic Deformation of SAE 52100 Steel Ball Bearings," Trans. of the ASME, vol. 109, October, 1987, pp. 618-626.
- 30 A.B. Jones: Steel, vol. 119, September 30, 1946, pp. 68-70; 97-100.
- 31 W.E. Littman and R.L. Widner, "Propagation of Contact Fatigue from Surface and Subsurface Origins," Trans. of the ASME, September, 1966, pp. 624-636.
- 32 Rolling Contact Fatigue Testing of Bearing Steels, A Symposium Presented at May Committee Week, J.J.C. Hoo Editor, ASTM STP 771 04-771000-02, Phoenix, AR, May 12-14, 1981, p. 386.
- 33 Bearing Steels: The Rating of Nonmetallic Inclusions, A Symposium Presented at May Committee Week, J.J.C. Hoo Editor, ASTM STP 575 04-575000-02, Boston, MA, May 22-24, 1974, p. 56.
- 34 Rolling Contact Fatigue Testing of Bearing Steels, A Symposium Presented at May Committee Week, J.J.C. Hoo Editor, ASTM STP 771 04-771000-02, Phoenix, AR, May 12-14, 1981, p. 79.
- 35 E.V. Zaretsky, "Selection of Rolling-Element Bearing Steels for Long-Life Application," NASA TM 88881, NASA Lewis Research Center, Cleveland, OH, 1986.
- 36 Rolling Contact Fatigue Testing of Bearing Steels, A Symposium Presented at May Committee Week, J.J.C. Hoo Editor, ASTM STP 771 04-771000-02, Phoenix, AR, May 12-14, 1981, p. 389.
- 37 T. Balliett and G. Krauss, "The Effect of the First and Second Stages of Tempering on Microcracking in Martensite of an Fe-1.22C Alloy," Metall. Trans. A., Vol. 7A, January, 1976, pp. 81-86.
- 38 V. Bhargava, G.T. Hahn, and C.A. Rubin, "Rolling Contact Deformation, Etching Effects, and Failure of High Strength Bearing Steel," Metall. Trans. A., vol. 21A, July, 1990, pp. 1921-1931.

- 39 Bearing Steels: The Rating of Nonmetallic Inclusions, A Symposium Presented at May Committee Week, J.J.C. Hoo Editor, ASTM STP 575 04-575000-02, Boston, MA, May 22-24, 1974, p. 84.
- 40 Bearing Steels: The Rating of Nonmetallic Inclusions, A Symposium Presented at May Committee Week, J.J.C. Hoo Editor, ASTM STP 575 04-575000-02, Boston, MA, May 22-24, 1974, p. 85.
- 41 M. Kuroda: Trans. Jap. Soc. Mech. Engr., vol. 26, 1960, pp. 1258-1270.
- 42 J.J. Bush, W.L. Grube, and G.H. Robinson: Trans. of the ASM, vol. 54, 1964, pp. 390-412.
- 43 K.L. Johnson and J.E. Merwin, Proc. Inst. Mech. Engrs., 177, 1963, p. 676.
- 44 J.O. Almen, Rolling Contact Phenomena, J.B. Bidwell Editor, Elsevier, Amsterdam, 1962.
- 45 Rolling Contact Fatigue Testing of Bearing Steels, A Symposium Presented at May Committee Week, J.J.C. Hoo Editor, ASTM STP 771 04-771000-02, Phoenix, AR, May 12-14, 1981, p. 293.
- 46 Rolling Contact Fatigue Testing of Bearing Steels, A Symposium Presented at May Committee Week, J.J.C. Hoo Editor, ASTM STP 771 04-771000-02, Phoenix, AR, May 12-14, 1981, p. 393.
- 47 "Operational Procedures for the Polymet Rolling Contact Fatigue Machine," Polymet Corp., Cincinnati, Ohio, 1975.
- 48 Rolling Contact Fatigue Testing of Bearing Steels, A Symposium Presented at May Committee Week, J.J.C. Hoo Editor, ASTM STP 771 04-771000-02, Phoenix, AR, May 12-14, 1981, p. 11.
- 49 Rolling Contact Fatigue Testing of Bearing Steels, A Symposium Presented at May Committee Week, J.J.C. Hoo Editor, ASTM STP 771 04-771000-02, Phoenix, AR, May 12-14, 1981, pp. 280,288.

- 50 D.L. Williamson, R.G. Schupmann, J.P. Materkowski, and G. Krauss, "Determination of Small Amounts of Austenite and Carbide in Hardened Medium Carbon Steels by Mossbauer Spectroscopy," Metall. Trans. A., vol. 10A, March, 1979, pp. 379-382.
- 51 D.L. Williamson, K. Nakazawa, and G. Krauss, "A Study of the Early Stages of Tempering in an Fe-1.2%C Alloy," Metall. Trans., vol. 10A, 1979, p. 1351.
- 52 C.B. Ma, T. Ando, D.L. Williamson, and G. Krauss, "Chi-Carbide Formation in a Tempered High Carbon Martensite," Metall. Trans., vol. 14A, 1983, p. 1033.
- 53 D.L. Williamson, F.M. Kustas, D.F. Fobare, and M.S. Misra, "Mossbauer Study of Ti-implanted 52100 Steel," J. Appl. Phys., vol. 60, 1986, p. 3466.
- 54 G. Petzow, Metallographic Etching, Metallographic and Ceramographic Methods for Revealing Microstructure, ASM, Metals Park, OH, 1978, pp. 103,104.
- 55 C.A. Johnson, Metallography Principles and Procedures, Leco Corporation, 1989, pp. 23-28.
- 56 G.F. VanderVoort, Metallography - Principles and Practice, McGraw-Hill, New York, 1984.
- 57 R.E. Miller, D.L. Williamson, and G. Krauss, "Life Prediction for Contact Fatigue of Carburized Tribological Materials," ASPPRC Research Report MT-SRC-090-004, Colorado School of Mines, Golden, CO, March 1, 1990, pp. 131-138.
- 58 K.A. Erven, "The Effects of Sulfur and Titanium on Bending Fatigue Performance of Carburized Steels," M.S. Thesis, MT-SRC-090-011, July, 1990.
- 59 V.K. Sharma, G.H. Walter, D.H. Breen, "Journal of Heat Treating - An Analytical Approach for Establishing Case Depth Requirements in Carburized Gears," Journal of Heat Treating, vol. 1, no. 1, 1979, pp. 48-57.
- 60 V. Bhargava, G.T. Hahn, and C.A. Rubin, "Rolling Contact Deformation, Etching Effects, and Failure of High Strength Bearing Steel," Metall. Trans. A., Vol. 21A, July, 1990, pp. 1921-1931.

61 Ochi (Nippon Steel), private communication, 1991.

APPENDIX

Start-up of Fatigue Machines

There are several steps to start-up of the TRFM fatigue machines. First, coat one end of a specimen with molydisulfide and put it into the chuck of the motor spindle. Bring the "nut cracker" arms up and fasten the tension bolt at top. The button on the main control panel is depressed to activate the lubrication system. Once oil is flowing, the flow valves are set such that there is continuous flow to the contact regions of both machines. Continuous flow, no matter how thin the flow, provides ample lubrication for testing. Orient the lubrication nozzles such that the oil enters the contact region in the direction of rolling, Figure 29.

There are two buttons on opposite ends of a rectangular block inside the machines, Figure A-1 (5), buttons number 10 and 11. The button on the right applies pressure to the system and the one on the left removes it. The black knob on the Nullmatic controller, number 1, determines how much pressure is applied. Set the Nullmatic controller such that approximately 850 lb of load is applied to the load cell. The load applied at the load

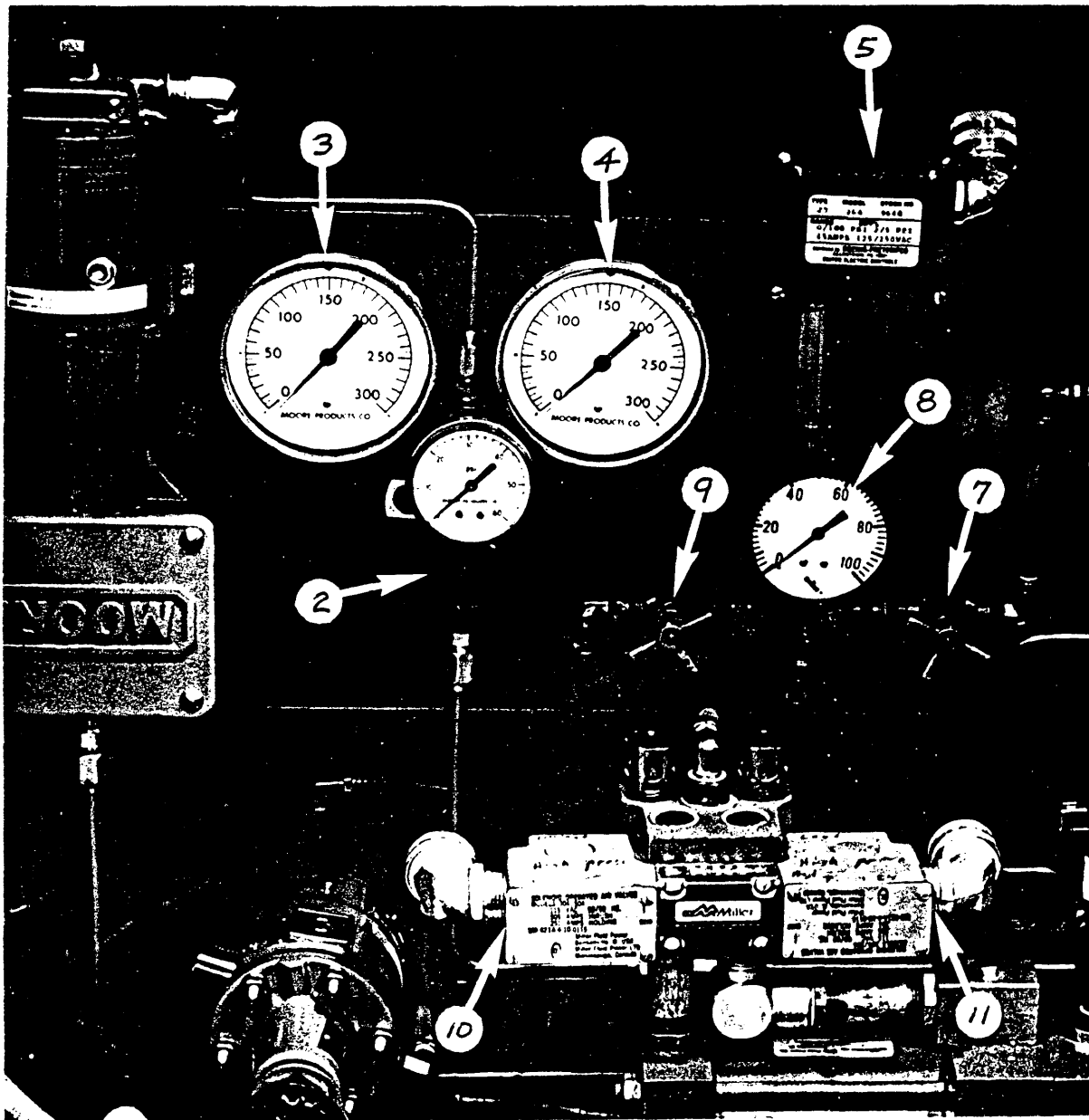


Figure A-1: Inside view of the controls of the Timken Rolling Fatigue Machines, various controls are numbered (5).

cell is multiplied by the moment arm such that 1700 lb is applied to the specimen. Manually turn the motor spindle for 50 turns while observing the maximum and minimum loads. For the testing done here, the difference between the maximum and minimum readings did not exceed 154 lb. The amount of difference is a function of the eccentricity of the motor spindle and how the specimen is set in the chuck. The eccentricity was usually 0.008 to 0.010 mm (0.0003 to 0.0004 in). The maximum eccentricity was 0.110 mm (0.0043 in).

The system is now prepared for start-up. Depress the left button. Allow the pressure to return to zero. Then depress the right hand button and at the same time depress the drive start and vibration bypass switches. Hold the drive start and vibration bypass switches down until the motor reaches operating speed. For more information refer to the manual written by Dave Lawrentz of Timken (5).

The goal specimen loading was 7562 N (1700 lb) for the Caterpillar specimens. However, due to machine error, the actual loading was $7562 \text{ N} \pm 445 \text{ N}$ ($1700 \text{ lb} \pm 100 \text{ lb}$). Figure 28 shows a spike in the load at start-up. The spike occurs due to lag in the system. With experience, spikes can be controlled by adjusting the Nullmatic controller during operation.

As soon as the machine is operating, check the reading on the load cell. Write this number down. Then adjust the Nullmatic controller up or down 5 psi and let the machine equilibriate. Once the machine seems stable and is within 50 lbs of the goal, 850 lb, leave it for 30 minutes to 1 hour. Return and check the load. Adjust the controller as needed and allow to equilibriate. Check the machine as time allows; once a day works well.

Table A-1: Raw Mossbauer Data

	Sample	RCF cycles	Etch	File
1	UNCARB.	0.0	NO	N4098
2	TRH	0.0	NO	N4094
3	--	0.0	NO	N4095
4	--	0.0	5 MILS	W102
5	--	0.0	5 MILS	W103
6	--	0.0	10 MILS	W125
7	TR1	300000000.0	NO	N4096
8	--	300000000.0	NO	N4099
9	--	300000000.0	5 MILS	W91
10	--	300000000.0	5 MILS	W107
11	--	300000000.0	10 MILS	W147
12	TR2	1000000000.0	NO	N4200
13	--	1000000000.0	NO	N4201
14	--	1000000000.0	NO	N4202
15	--	1000000000.0	5 MILS	W93
16	--	1000000000.0	5 MILS	W108
17	--	1000000000.0	10 MILS	W146
18	11-CRH2	0.0	NO	W127
19	--	0.0	NO	W126
20	--	0.0	10 MILS	N4367
21	50-CRH1	0.0	20 MILS	W195
22	30-CR11	10.0	NO	W128
23	--	10.0	NO	W133
24	--	10.0	NO	W139
25	--	10.0	NO	W141
26	30-CR12A	100.0	NO	W129
27	--	100.0	NO	W132
28	--	100.0	NO	W142
29	--	100.0	NO	W143
30	40-CR12B	100.0	NO	W130
31	--	100.0	NO	W131
32	00-CR13	1000.0	NO	W144
33	--	1000.0	NO	W145
34	--	1000.0	NO	W149
35	41-CR21	10000.0	NO	W191
36	--	10000.0	NO	W197
37	43-CR22	100000.0	NO	W192
38	--	100000.0	NO	W196
39	52-CR23	1000000.0	NO	W171
40	--	1000000.0	NO	W198
41	22-CR31	10000000.0	NO	W169
42	--	10000000.0	NO	W170
43	51-CR32	100000000.0	NO	W167
44	--	100000000.0	NO	W168
45	53-CR33	500000000.0	NO	W153
46	--	500000000.0	NO	W154
47	--	500000000.0	10 MILS	W223
48	54-CR33	500000000.0	20 MILS	N4281
49	90-CR41	1400000000.0	NO	W193
50	--	1400000000.0	NO	W194
51	70-CD	0.0	NO	W156
52	--	0.0	NO	W161
53	--	0.0	10 MILS	N4366
54	73-CD22	100000.0	NO	W177S
55	83-CD33	500000000.0	NO	W155
56	--	500000000.0	10 MILS	W222
57	84-CD33	500000000.0	20 MILS	N4280

continued

Table A-1 (continued)

	E. X. A	Fa(%)	Fc(%)	Quality
1	E	0.0	0.0	GOOD
2	X	26.6	3.6	GOOD
3	E	21.8	4.1	GOOD
4	E	3.3	4.9	GOOD
5	X	19.8	6.1	FAIR
6	X	21.7	2.1	GOOD
7	E	6.4	5.6	FAIR
8	X	18.5	5.5	POOR
9	E	5.0	2.1	FAIR
10	X	17.6	2.5	FAIR
11	X	13.6	8.1	POOR
12	E	4.0	9.3	FAIR
13	X	13.0	9.9	POOR
14	E-A	15.0	6.5	FAIR
15	E	4.6	6.0	FAIR
16	X	12.9	5.2	POOR
17	X	7.8	0.0	POOR
18	E	26.6	0.0	GOOD
19	X	24.6	1.5	GOOD
20	X	22.2	0.0	FAIR
21	X	20.2	0.0	FAIR
22	E	22.1	0.0	FAIR
23	E-A	26.8	0.0	GOOD
24	X-A	25.0	0.0	FAIR
25	X	20.1	1.0	POOR
26	E	22.1	0.0	GOOD
27	E-A	26.9	0.0	GOOD
28	X-A	25.5	0.0	FAIR
29	X	23.5	1.0	POOR
30	E	30.9	0.0	GOOD
31	E-A	36.8	0.0	GOOD
32	X	21.4	0.0	POOR
33	X-A	28.7	0.0	FAIR
34	E-A	40.0	0.0	GOOD
35	E	30.7	0.0	FAIR
36	X	22.7	0.0	POOR
37	E	23.8	0.0	FAIR
38	X	23.4	0.5	FAIR
39	X	21.2	0.4	FAIR
40	E	16.2	0.0	POOR
41	E	5.7	2.7	FAIR
42	X	19.2	0.0	POOR
43	X	14.9	2.4	POOR
44	E	4.2	3.7	FAIR
45	E	1.6	2.6	GOOD
46	X	11.7	0.0	FAIR
47	X	20.9	0.0	FAIR
48	X	15.2	3.1	POOR
49	E	1.5	3.0	POOR
50	X	14.3	2.4	FAIR
51	X	27.8	0.0	GOOD
52	E	31.9	1.5	GOOD
53	X	21.1	0.0	FAIR
54	X	25.2	2.2	POOR
55	X	10.7	0.0	FAIR
56	X	21.1	0.1	FAIR
57	X	20.0	0.0	POOR

continued

Table A-2: Microhardness Conversion Chart For Leco M-400A

M-400A - Load 300gf - Obj. Lens 55X

VICKERS HARDNESS NUMBER											
a	0.0	0.2	0.4	0.6	0.8	a	0.0	0.2	0.4	0.6	0.8
34	3560	3518	3477	3437	3398	89	520	517	515	513	510
35	3359	3321	3284	3247	3211	90	508	506	504	501	499
36	3175	3140	3106	3072	3039	91	497	495	493	490	488
37	3006	2974	2942	2911	2880	92	486	484	482	480	478
38	2850	2820	2791	2762	2733	93	476	474	472	470	468
39	2705	2678	2651	2624	2598	94	466	464	462	460	458
40	2572	2546	2521	2496	2472	95	456	454	452	450	448
41	2448	2424	2401	2378	2355	96	447	445	443	441	439
42	2333	2311	2289	2268	2246	97	437	436	434	432	430
43	2226	2205	2185	2165	2145	98	428	427	425	423	422
44	2126	2106	2087	2069	2050	99	420	418	416	415	413
45	2032	2014	1996	1979	1962	100	411	410	408	407	405
46	1945	1928	1911	1895	1879	101	403	402	400	399	397
47	1863	1847	1832	1816	1801	102	396	394	392	391	389
48	1786	1771	1757	1742	1728	103	388	386	385	383	382
49	1714	1700	1686	1673	1659	104	380	379	378	376	375
50	1646	1633	1620	1607	1595	105	373	372	370	369	368
51	1582	1570	1558	1546	1534	106	366	365	363	362	361
52	1522	1510	1499	1487	1476	107	359	358	357	355	354
53	1465	1454	1443	1432	1422	108	353	351	350	349	348
54	1411	1401	1391	1380	1370	109	346	345	344	343	341
55	1360	1350	1341	1331	1322	110	340	339	338	336	335
56	1312	1303	1294	1285	1275	111	334	333	332	330	329
57	1267	1258	1249	1240	1232	112	328	327	326	325	323
58	1223	1215	1207	1198	1190	113	322	321	320	319	318
59	1182	1174	1166	1158	1151	114	317	316	314	313	312
60	1143	1135	1128	1121	1113	115	311	310	309	308	307
61	1106	1099	1092	1084	1077	116	306	305	304	303	302
62	1070	1064	1057	1050	1043	117	301	300	299	298	297
63	1037	1030	1024	1017	1011	118	296	295	294	293	292
64	1005	998	992	986	980	119	291	290	289	288	287
65	974	968	962	956	950	120	286	285	284	283	282
66	945	939	933	928	922	121	281	280	279	278	277
67	917	911	906	900	895	122	276	276	275	274	273
68	890	885	880	874	869	123	272	271	270	269	268
69	864	859	854	849	845	124	268	267	266	265	264
70	840	835	830	826	821	125	263	263	262	261	260
71	816	812	807	803	798	126	259	258	258	257	256
72	794	789	785	781	776	127	255	254	254	253	252
73	772	768	764	760	756	128	251	250	250	249	248
74	751	747	743	739	735	129	247	247	246	245	244
75	732	728	724	720	716	130	243	243	242	241	241
76	712	709	705	701	698	131	240	239	238	238	237
77	694	690	687	683	680	132	236	235	235	234	233
78	676	673	669	666	663	133	233	232	231	231	230
79	659	656	653	649	646	134	229	228	228	227	226
80	643	640	637	633	630	135	226	225	224	224	223
81	627	624	621	618	615	136	222	222	221	221	220
82	612	609	606	603	600	137	219	219	218	217	217
83	597	594	592	589	586	138	216	215	215	214	214
84	583	580	578	575	572	139	213	212	212	211	211
85	570	567	564	562	559	140	210	209	209	208	208
86	556	554	551	549	546	141	207	206	206	205	205
87	544	541	539	536	534	142	204	204	203	202	202
88	531	529	527	524	522	143	201	201	200	200	199

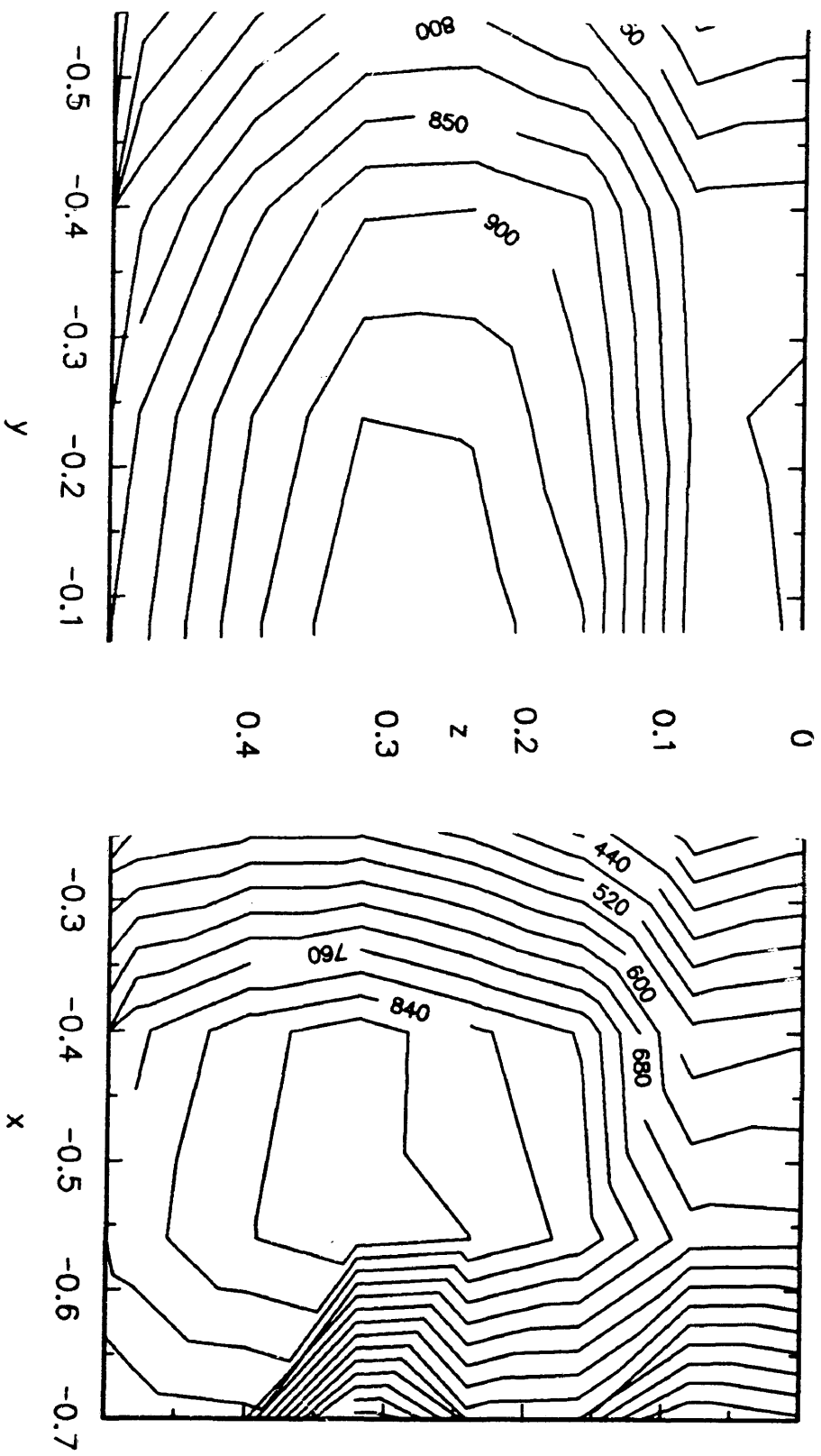


Figure 59: Imposed τ_{xz} stresses on the xz and yz planes of TR41. A rough correlation is evident between the regions of highest τ_{xz} stress and the white etching bands in TR41, 2% nital etch for 15 seconds, 200X.